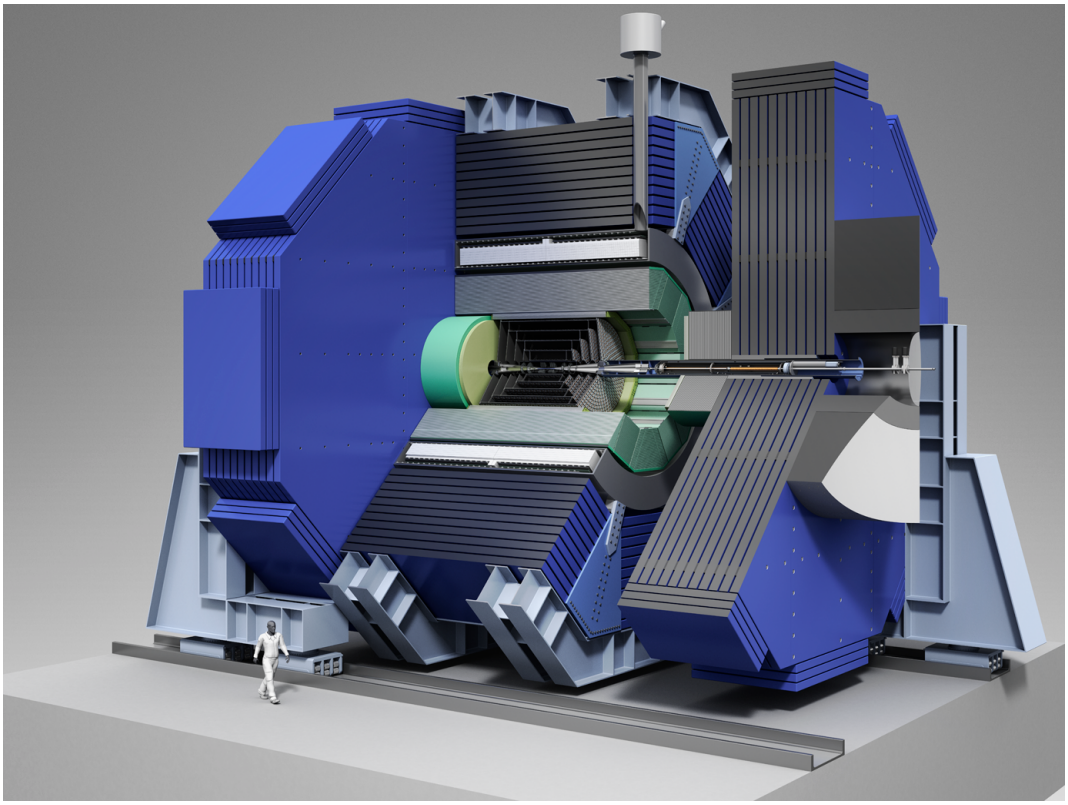

SiD

Detailed Baseline Design

Draft submitted to the PAC (revised)

10 December 2012

MAIN EDITORS

P.N. Burrows[1], L. Linssen[2], M. Oreglia[3], M. Stanitzki[4], A. White[5]

CHAPTER EDITORS

Vertex Detector
W. Cooper[6], R Lipton[6]

Silicon Tracking
W. Cooper[6], M. Demarteau[7], T. Nelson[8]

Calorimetry
R. Frey[9], A. White[5], L. Xia[7]

Muon System
H. Band[10], G. Fisk[6]

Superconducting Magnet System
W. Craddock[8], M. Oriunno[8]

Engineering, Integration and the Machine Detector Interface
P. Burrows[1], T. Markiewicz[8]

Forward Systems
T. Maruyama[8], B. Schumm[11]

Electronics and DAQ
M. Breidenbach[8], G. Haller[8], M. Stanitzki[4]

Simulation and Reconstruction
N. Graf[8], J. Strube[2]

Benchmarking
D. Asner[12], T. Barklow[8], P. Roloff[2]

Costs
M. Breidenbach[8]

[1]*John Adams Institute, University of Oxford, Oxford, United Kingdom*
[2]*CERN, Geneva, Switzerland*
[3]*University of Chicago, Chicago, USA*
[4]*DESY, Hamburg, Germany*
[5]*University of Texas at Arlington, Arlington, USA*
[6]*Fermi National Accelerator Laboratory, Batavia, USA*
[7]*Argonne National Laboratory, Argonne, USA*
[8]*SLAC National Accelerator Laboratory, Menlo Park, USA*
[9]*University of Oregon, Eugene, USA*
[10]*University of Wisconsin, Madison, USA*
[11]*University of California, Santa Cruz, USA*
[12]*Pacific Northwest National Laboratory, Richland, USA*

Contents

Table of Contents **5**

Introduction **11**

1 Concept Overview **13**
1.1 SiD Philosophy . . . 13
1.2 Silicon-based Tracking . . . 14
1.2.1 Vertex detector . . . 14
1.2.2 Tracking . . . 17
1.3 Calorimetry . . . 17
1.4 Forward calorimeters . . . 18
1.5 Magnet Coil . . . 19
1.6 Muon System . . . 20
1.7 The Machine-Detector Interface . . . 20

2 Vertex Detector **21**
2.1 Introduction . . . 21
2.1.1 Vertex detector requirements . . . 21
2.2 Baseline Design . . . 22
2.2.1 Sensor Technology . . . 23
2.3 3D-Based Module Design . . . 24
2.3.1 Active Edge Devices . . . 25
2.3.2 Barrel Sensor Interconnect to Readout . . . 25
2.3.3 Sensor tiling for disks . . . 26
2.4 Support structures and Integration . . . 27
2.4.1 Power delivery . . . 29
2.4.2 Cooling . . . 31
2.4.3 Cabling . . . 32

2.5 R&D Status . . . 32
2.5.1 Chronopixel . . . 32
2.5.2 VIP 3D Chip . . . 33
2.5.3 Thinned hybrid detector with high-density interconnect . . . 33
2.5.4 Active Edge Tiles . . . 34
2.5.5 Critical R&D . . . 34
2.6 Summary . . . 34

3 Silicon Tracking **35**
3.1 Introduction . . . 35
3.2 Baseline Design . . . 37
3.2.1 Barrels . . . 38
3.2.2 Disks . . . 39
3.2.3 Barrel/Disk Integration . . . 40
3.3 Critical R&D . . . 41
3.4 Performance . . . 44
3.4.1 Tracking Efficiency . . . 44
3.4.2 Fake Rates . . . 46
3.4.3 Tracking Resolution . . . 47
3.5 Alignment . . . 48
3.5.1 Alignment Methods . . . 51
3.5.2 Push-Pull Considerations . . . 53

4 Calorimetry **55**
4.1 Introduction . . . 55
4.2 Electromagnetic Calorimeter . . . 56
4.2.1 Introduction . . . 56
4.2.2 Global ECAL Design . . . 57
4.2.3 Baseline Technology . . . 60
4.2.4 MAPS option . . . 64
4.2.5 Calibration and alignment . . . 66
4.3 Hadronic Calorimeter . . . 66
4.3.1 HCAL requirements . . . 66
4.3.2 Description of the DHCAL concept . . . 66
4.3.3 Global HCAL mechanical design . . . 67
4.3.4 Baseline technology . . . 67
4.3.5 DHCAL prototype performance . . . 74
4.3.6 R&D towards technical feasibility and optimisation . . . 78

4.3.7 Calibration of a Digital Hadron Calorimeter . . . 79
4.3.8 Alternative technologies . . . 81
4.4 Summary . . . 88

5 Muon System **89**
5.1 Backgrounds . . . 90
5.2 Detector design . . . 91
5.2.1 Scintillating strips . . . 92
5.2.2 Resistive Plate Chambers . . . 94

6 Superconducting Magnet System **99**
6.1 Introduction . . . 99
6.1.1 List of subsystems . . . 99
6.1.2 Design Philosophy . . . 100
6.2 Magnetic Field and Forces . . . 100
6.2.1 Requirements and Design . . . 100
6.2.2 Calculations . . . 101
6.3 Mechanical Engineering . . . 102
6.3.1 Solenoid Coil Production . . . 102
6.3.2 Integration of DID to solenoid . . . 103
6.3.3 Thermal shield, cooling tubes, current leads and standpipe . . . 104
6.3.4 Stress Analysis . . . 105
6.3.5 Vacuum Shell Design . . . 105
6.3.6 Assembly procedure . . . 106
6.4 Cryogenics . . . 107
6.5 Conductor . . . 108
6.5.1 Solenoid baseline conductor (CMS) . . . 108
6.5.2 Modified CMS Conductor Choices . . . 108
6.5.3 DID conductor . . . 109
6.6 Electrical . . . 109
6.6.1 Magnet Safety . . . 109
6.6.2 Power Supply, Dump Resistor and Dump Switch . . . 110

7 Engineering, Integration and the Machine Detector Interface **111**
7.1 Introduction . . . 111
7.2 IR Hall Layout Requirements and SiD Assembly . . . 112
7.2.1 Vertical Access (Europe and Americas sites) . . . 113
7.2.2 Horizontal Access (Japan sites) . . . 115

7.2.3 Detector Access for Repairs . . . 115
7.3 Detector Exchange Via a Sliding Platform . . . 116
7.3.1 Introduction . . . 116
7.3.2 Platform . . . 116
7.3.3 Vibration analysis and Luminosity Preservation . . . 117
7.3.4 Push Pull Detector Exchange Process and Time Estimate . . . 118
7.4 Beampipe and Forward Region Design . . . 119
7.4.1 Introduction to the Near Beamline Design . . . 119
7.4.2 Beampipe . . . 119
7.4.3 LumiCal, BeamCal, Mask and QD0 Support and Alignment . . . 120
7.4.4 Vacuum System and Performance . . . 120
7.4.5 Feedback and BPMs . . . 120
7.4.6 Frequency Scanning Interferometric (FSI) Alignment of QD0 and QF1 . . . 122

8 Forward Systems 123
8.1 Forward Detector . . . 123
8.1.1 Design criteria . . . 124
8.1.2 Baseline Design . . . 125
8.1.3 Forward Systems Development Work . . . 127

9 Electronics and DAQ 133
9.1 ASIC developments . . . 133
9.1.1 KPiX . . . 134
9.2 On-Detector Electronics . . . 135
9.3 Off-Detector Electronics . . . 136
9.4 Overview of Electronics Channels and Expected Data Rates . . . 137

10 Simulation and Reconstruction 139
10.1 Overview of the Simulation and Reconstruction Software . . . 139
10.2 The SiD DBD Production . . . 140
10.3 Simulating the SiD Detector Geometry . . . 141
10.3.1 The SIDLOI3 Model . . . 141
10.4 Simulation of the full Detector Response . . . 142
10.4.1 Silicon Pixel and Strip Hit Digitisation . . . 143
10.4.2 Calorimeter Hit Digitisation . . . 143
10.4.3 Clustering . . . 144
10.5 Detector Performance . . . 144

10.5.1 Particle Identification: Photon, Electron and Muon ID 144
10.5.2 Jet Flavour Tagging: Efficiency and Purity 145
10.5.3 Di-Jet Energy Resolution 147

11 Benchmarking **151**
11.1 Event Generation 151
11.1.1 Signal and Background samples used for full simulation and reconstruction 151
11.2 Analysis Tools 153
11.2.1 Jet finding 153
11.2.2 Multivariate analysis tools 153
11.3 Summary of the LOI Results 153
11.4 DBD Benchmark Reactions 157
11.4.1 Measurement of the top Yukawa coupling 157
11.4.2 Higgs branching fractions 162
11.4.3 Measurement of beam polarisation using WW pairs 164
11.4.4 Top quark cross-section, mass, and forward-backward asymmetry . 170
11.5 Additional Benchmarks 173
11.5.1 The Analysis and the Importance of the BeamCal 173
11.6 Benchmarking Summary 175

12 Costs **179**
12.1 Introduction 179
12.2 Parametric cost model 180
12.3 Results 181
12.4 Parameter Dependencies 183

13 Summary **187**
13.1 The Status of the SiD Detector Concept 187
13.2 Further Development of the SiD Detector Concept 187
13.3 SiD and the New Global Linear Collider Organisation 188

Bibliography **189**

Introduction

The next generation of collider detectors, to study electroweak symmetry breaking and potential discoveries beyond the Standard Model, will demand a high level of precision in the measurement of physics properties. The SiD detector was conceived as a fully integrated, unified design with the basic features of compactness, silicon-based tracking, fine-grained calorimetry and a high central magnetic field.

Building on extensive experience with previous detectors, and exploiting major advances in sensors, materials, and electronics, this design has been developed for experiments at a future linear collider. The Silicon Detector, SiD, is the result of many years of creative design by physicists and engineers, backed by a substantial body of past and ongoing detector research and development. While each component of SiD has received the benefits of continuous development projects, the SiD design closely integrates these components into a whole system for excellent measurements of jet energies, based on the Particle Flow Algorithm approach, as well as charged leptons, photons and missing energy. The use of robust silicon vertexing and tracking makes SiD applicable to a wide range of lepton colliders from a Higgs factory to multi-TeV machines. SiD has been designed in a cost-conscious manner, with the compact design limiting the areas of high performing, high value, components. The restriction on dimensions is offset by the relatively high central magnet field from a superconducting solenoid. This Detailed Baseline Design builds on the results presented in our earlier Letter of Intent. While detector and physics studies continue, we regard this document as a substantive starting point for the development of a full Technical Design Report.

This design report presents an overview of the SiD Concept, its design philosophy, and the approach to each component. It presents detailed discussions of each of SiD's various subsystems, an overview of the full GEANT4 description of SiD, the status of the tracking and calorimeter reconstruction algorithms, studies of subsystem performance based on these tools, results of physics benchmark analyses, an estimate of the cost of the detector, and an assessment of the detector research and development needed to provide the technical basis for an optimised SiD.

Chapter 1

Concept Overview

1.1 SiD Philosophy

The SiD detector [1] is a general-purpose experiment designed to perform precision measurements at ILC. It satisfies the challenging detector requirements that are described in the Common Section. SiD is based on the paradigm of particle flow, an algorithm by which the reconstruction of both charged and neutral particles is accomplished by an optimised combination of tracking and calorimetry. The net result is a significantly more precise jet energy measurement which results in a di-jet mass resolution good enough to distinguish between W's and Z's.

The SiD detector (Figures 1.1.1, 1.1.2) is a compact detector based on a powerful silicon pixel vertex detector, silicon tracking, silicon-tungsten electromagnetic calorimetry and highly segmented hadronic calorimetry. SiD also incorporates a high-field solenoid, iron flux return, and a muon identification system. The use of silicon sensors in the vertex, tracking and calorimetry enables a unique integrated tracking system ideally suited to particle flow.

The choice of silicon detectors for tracking and vertexing ensures that SiD is robust with respect to beam backgrounds or beam loss, provides superior charged particle momentum resolution, and eliminates out-of-time tracks and backgrounds. The main tracking detector and calorimeters are "live" only during a single bunch crossing, so beam-related backgrounds and low-p_T backgrounds from $\gamma\gamma$ processes will be reduced to the minimum possible levels. The SiD calorimetry is optimised for excellent jet energy measurement using the particle flow technique. The complete tracking and calorimeter systems are contained within a superconducting solenoid, which has a 5 T field strength, enabling the overall compact design. The coil is located within a layered iron structure that returns the magnetic

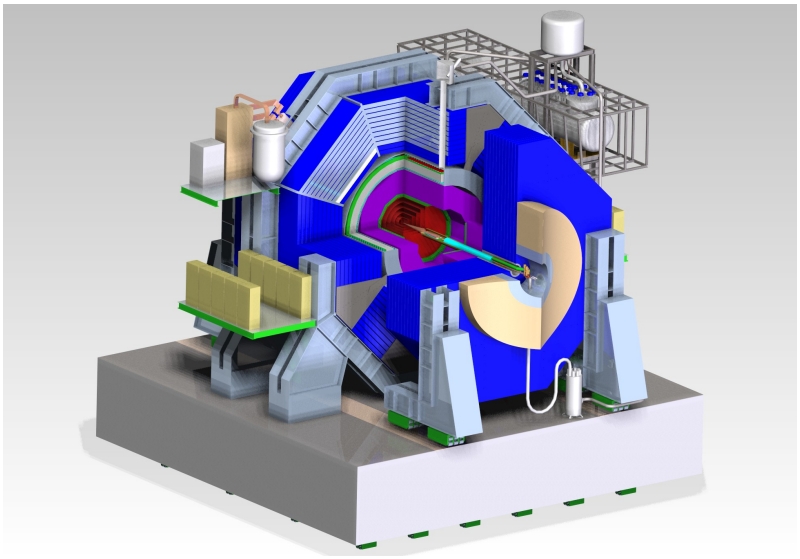

Figure 1.1.1: The SiD detector on its platform, showing tracking (red), ECAL (green), HCAL (violet) and flux return (blue).

flux and is instrumented to allow the identification of muons. All aspects of the SiD detector are the result of intensive and leading-edge research conducted to raise its performance to unprecedented levels. At the same time, the design represents an of imised balance between cost and physics performance. The key parameters of the SiD design are listed in Table 1.1.1.

1.2 Silicon-based Tracking

1.2.1 Vertex detector

To unravel the underlying physics mechanisms of new observed processes, the identification of heavy flavours will play a critical role. One of the main tools for heavy flavour identification is the vertex detector. The physics goals dictate an unprecedented spatial three-dimensional point resolution and a very low material budget to minimise multiple Coulomb scattering. The running conditions at the ILC impose the readout speed and radiation tolerance. These requirements are normally in tension. High granularity and fast readout compete with each other and tend to increase the power dissipation. Increased power dissipation in turn leads to an increased material budget. The challenges on the vertex detector

Table 1.1.1: Key parameters of the baseline SiD design. (All dimension are given in cm.)

SiD BARREL	Technology	Inner radius	Outer radius	z max
Vertex detector	Silicon pixels	1.4	6.0	$\pm$ 6.25
Tracker	Silicon strips	21.7	122.1	$\pm$ 152.2
ECAL	Silicon pixels-W	126.5	140.9	$\pm$ 176.5
HCAL	RPC-steel	141.7	249.3	$\pm$ 301.8
Solenoid	5 Tesla	259.1	339.2	$\pm$ 298.3
Flux return	Scintillator/steel	340.2	604.2	$\pm$ 303.3
SiD ENDCAP	**Technology**	**Inner z**	**Outer z**	**Outer radius**
Vertex detector	Silicon pixels	7.3	83.4	16.6
Tracker	Silicon strips	77.0	164.3	125.5
ECAL	Silicon pixel-W	165.7	180.0	125.0
HCAL	RPC-steel	180.5	302.8	140.2
Flux return	Scintillator/steel	303.3	567.3	604.2
LumiCal	Silicon-W	155.7	170.0	20.0
BeamCal	Semiconductor-W	277.5	300.7	13.5

are considerable and significant R&D is being carried out on both the development of the sensors and the mechanical support.

The vertex detector for SiD uses a barrel-disk layout. The barrel section consists of five silicon pixel layers with a pixel size of 20 $\times$ 20 μm^2. The forward and backward regions each have four silicon pixel disks. In addition, there are three silicon pixel disks at a larger distance from the interaction point to provide uniform coverage for the transition region between the vertex detector and the outer tracker. This configuration provides for very good hermeticity with uniform coverage and guarantees good pattern recognition capability for charged tracking and excellent impact parameter resolution over the full solid angle. The layout of the vertex detector provides excellent tracking pattern recognition capability. This enhances the tracking capability of the integrated tracking system, and in conjunction with the high magnetic field, makes for a very compact tracking system, thereby minimising the

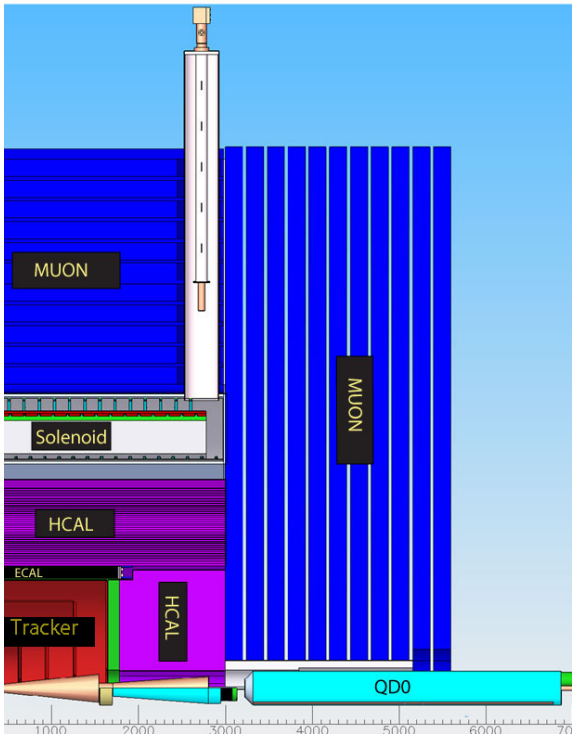

Figure 1.1.2: Quadrant of the SiD detector.

size and costs of the calorimetry.

To provide for a very robust track-finding performance, the SiD detector has as its baseline choice for the vertex detector a sensor technology that provides putting a time stamp on each hit with sufficient precision to assign each hit to a particular bunch crossing. This significantly reduces the effective backgrounds. Several technologies are being developed. One of them is a CMOS-based monolithic pixel sensor called Chronopixel. The main goal for the design is a pixel size of about 10×10 μm^2 with 99% charged-particle efficiency. Prototype devices have demonstrated that the concept works; what should be a fully functional chip is presently under test. Another, more challenging technology, is the 3D vertical integrated silicon technology. A full demonstration is close with this technology too.

Minimising the support material is critical to the development of a high-performance vertex detector. Different groups are studying an array of low-mass materials such as various reticulated foams and silicon-carbide materials. An alternative approach that is being pursued very actively is the embedding of thinned, active sensors in ultra low-mass media.

This line of R&D explores thinning active silicon devices to such a thickness that the silicon becomes flexible. The devices can then be embedded in, for example, Kapton structures, providing extreme versatility in designing and constructing a vertex detector. Power delivery must be accomplished without exceeding the material budget and overly heating the detector. The vertex detector design relies on power pulsing during bunch trains to minimise heating and uses forced air for cooling.

1.2.2 Tracking

The tracking system is a key element of the detector concepts at the ILC. The particle flow algorithm requires excellent tracking with superb efficiency and two-particle separation. The requirements from precision measurements, in particular in the Higgs sector, place high demands on the momentum resolution at the level of $\delta(1/p_{\mathrm{T}}) \sim 2-5\times10^{-5}/\mathrm{GeV}$.

Highly efficient charged particle tracking is achieved using the pixel detector and main tracker to recognise and measure prompt tracks, and the ECAL, which can identify short track stubs in its first few layers, in conjunction with the main tracker, to catch tracks arising from secondary decays of long-lived particles. With the choice of a 5 T solenoidal magnetic field, in part chosen to control the e^+e^- pair background, the design allows for a compact tracker design. The technology of choice is silicon strip sensors arrayed in five nested cylinders in the central region and four disks following a conical surface with an angle of 5 degrees with respect to the normal to the beamline in each of the end regions for precision tracking and momentum measurement. The geometry of the endcaps minimises the material budget to enhance forward tracking. The detectors are single sided silicon sensors, approximately 10×10 cm^2 with a readout pitch of 50 μm. The endcaps utilise two sensors bonded back-to-back for small angle stereo measurements. With an outer cylinder radius of 1.25 m and a 5 T field, the charged track momentum resolution will be better than $\delta(1/p_{\mathrm{T}}) = 5\times10^{-5}/(\mathrm{GeV})$ for high momentum tracks and down to polar angles of 10 degrees.

The all-silicon tracking approach has been extensively tested using full Monte-Carlo simulations including full beam backgrounds. Besides having an excellent momentum resolution it provides robust pattern recognition even in the presence of backgrounds and has a real safety margin, if the machine backgrounds will be worse than expected.

1.3 Calorimetry

The baseline design for the SiD detector incorporates the elements needed to successfully implement the particle flow approach. This imposes a number of basic requirements on the calorimeter systems. The entire central calorimeter system must be contained within the

solenoid in order to reliably associate tracks to energy deposits. The electromagnetic and hadronic sections of the calorimeter must have imaging capabilities that allow both efficient track-following and correct assignment of energy clusters to tracks. These requirements imply that the calorimeters must be finely segmented both longitudinally and transversely. In order to ensure that no significant amount of energy can escape detection, the calorimeter system must extend down to small angles with respect to the beampipe and must be sufficiently deep to prevent significant energy leakage. Since the average penetration depth of a hadronic shower grows with its energy, the calorimeter system must be designed for the highest-energy collisions envisaged.

The mechanical design of the calorimeter consists of a series of modules of manageable size and weight to ease detector construction. The boundaries between modules are kept as small as possible to prevent significant non-instrumented regions. The detectors are designed to have excellent long-term stability and reliability, since access during the data-taking period will be extremely limited, if not impossible.

The combined SiD electromagnetic and hadronic calorimeter systems consist of a central barrel part and two endcaps, nested inside the barrel. The entire barrel system is contained within the volume of the cylindrical superconducting solenoid. The electromagnetic calorimeter has silicon active layers between tungsten absorber layers. The active layers use 5×5 mm silicon pixels providing excellent spatial resolution. The structure has 30 layers in total, the first 20 layers having a thinner absorber than the last ten layers. This configuration is a compromise between cost, electromagnetic shower radius, sampling frequency, and shower containment. The total depth of the electromagnetic calorimeter is 26 radiation lengths (X_0) and one nuclear interaction length. The hadronic calorimeter has a depth of 4.5 nuclear interaction lengths, consisting of alternating steel plates and active layers. The baseline choice for the active layers are glass resistive plate chambers, which have been extensively evaluated in testbeam campaigns at Fermilab and CERN. Two other technologies (GEM, and Micromegas) are currently being prototyped and evaluated as potential options for SiD.

1.4 Forward calorimeters

Two special calorimeters are foreseen in the very forward region of the ILC detectors - LumiCal for the precise measurement, and BeamCal for the fast estimation, of the luminosity. LumiCal and BeamCal are compact cylindrical electromagnetic calorimeters centred on the outgoing beam. They are based on semiconductor-tungsten technology with 30 layers in depth. BeamCal is placed just in front of the final focus quadrupole and LumiCal is aligned with the electromagnetic calorimeter endcap. LumiCal uses silicon sensor readout. It is

a precision device with challenging requirements on the mechanics and position control. BeamCal is exposed to a large amount of low-energy electron-positron pairs originating from beamstrahlung. These depositions, useful for a bunch-by-bunch luminosity estimate and the determination of beam parameters, require radiation hard sensors. The detectors in the very forward region have to tackle relatively high occupancies, requiring dedicated front-end electronics.

The challenge of BeamCal is to find sensors tolerating about one MGy of dose per year. So far polycrystalline chemical vapour deposition (CVD) diamond sensors of 1 cm^2 and larger sectors of GaAs pad sensors have been studied. Since large-area CVD diamond sensors are extremely expensive, they may be used only at the innermost part of BeamCal. At larger radii GaAs sensors appear to be a promising option. Sensor samples produced using the liquid encapsulated Czochralski method have been studied in a high-intensity electron beam. For SiD, the main activities are the study of these radiation-hard sensors, development of the first version of the so-called Bean readout chip, and the simulation of BeamCal tagging for physics studies. SiD coordinates these activities with the FCAL R&D Collaboration.

1.5 Magnet Coil

The SiD superconducting solenoid is based on the CMS solenoid design philosophy and construction techniques, using a slightly modified CMS conductor as its baseline design. Superconducting strand count in the coextruded Rutherford cable was increased from 32 to 40 to accommodate the higher 5 T central field. Many iron flux return configurations have been tested in two dimensions to reduce the fringe field. An Opera 3D calculation with the Detector Integrated Dipole (DID) coil has been completed. Calculations of magnetic field with a 3D ANSYS program are in progress. These will have the capability to calculate forces and stress on the DID as well as run transient cases to check the viability of using the DID as a quench propagator for the solenoid. Field and force calculations with an iron endcap HCAL were studied. The field homogeneity improvement was found to be insufficient to pursue this option. Conceptual DID construction and assembly methods have been studied. The solenoid electrical power system, including a water-cooled dump resistor and grounding, was established. Significant work has been expended on examining different conductor stabiliser options and conductor fabrication methods. This work is pursued as a cost- and time-saving effort for solenoid construction.

1.6 Muon System

The return yoke for SiD is instrumented with position sensitive detectors to serve as both a muon filter and a tail catcher. The total area to be instrumented is very significant - several thousand square meters. Technologies that lend themselves to low-cost large-area detectors are therefore under investigation. Particles arriving at the muon system have seen large amounts of material in the calorimeters and encounter significant multiple scattering inside the iron. Spatial resolutions of a few centimetres are therefore sufficient. Occupancies are low, so strip detectors are possible. In SiD, the baseline design uses scintillator technology, with RPCs as an alternative. The scintillator technology uses extruded scintillator readout with wavelength shifting fibre and SiPMs, and has been successfully demonstrated. Simulation studies have shown that nine or more layers of sensitive detectors yield adequate energy measurements and good muon-detection efficiency and purity.

1.7 The Machine-Detector Interface

The push-pull system for the two detectors was only conceptual at the time of LoI publication, but since then the engineering design has progressed significantly. A time-efficient implementation of the push-pull model of operation sets specific requirements and challenges for many detector and machine systems, in particular the interaction region (IR) magnets, the cryogenics, the alignment system, the beamline shielding, the detector design and the overall integration. The minimal functional requirements and interface specifications for the push-pull IR have been successfully developed and published [2, 3], to which all further IR design work on both the detectors and machine sides are constrained.

Chapter 2

Vertex Detector

2.1 Introduction

The SiD vertex detector consists of a central barrel section with five silicon pixel layers and forward and backward disk regions, each with four silicon pixel disks. Three silicon pixel disks at large z provide uniform coverage for the transition region between the vertex detector and the silicon micro-strip based outer tracker. The barrel layers and disks are arranged to provide good hermeticity to $\cos(\theta) \approx 0.984$ and to guarantee good pattern recognition capability for charged tracking and excellent impact parameter resolution over the whole solid angle.

2.1.1 Vertex detector requirements

The physics goals of the ILC, particularly the need to separate bottom and charm vertices, drive the need for a very precise, light vertex detector. The time structure and low radiation background in the ILC provides an environment which allows us to consider very light, low power detector structures. The bunch structure, with a 1 ms long bunch train at 5 Hz, enables power pulsing of the electronics, providing a power saving of a factor of 50-100 for front-end analog power. Low power allows gas-based cooling, saving mass in cooling channels and associated structures. The vertex detector for SiD is designed to meet the following goals:

- Hit resolution better then 5 μm in the barrel
- Less than 0.3% radiation length per layer
- Average power less than 130 $\mu W/mm^2$ in the barrel

- Single bunch time resolution.

These requirements then drive the design of the vertex system. The 5 µm resolution implies a pixel size of 17 µm, larger if charge sharing is used to improve the resolution. Some CMOS MAPS devices, which collect charge by diffusion rather than drift, can utilise larger pixels because diffusion naturally spreads the charge.

The small radiation length per layer is driven by the need for precise three dimensional vertex resolution for heavy quark decays. This resolution has a direct effect on the efficiency for b and c hadron identification. For a device with less than 0.3% radiation length per layer air cooling appears to be the only viable low-mass sensor cooling technique. Gas cooling places a limit on the average power based on the heat which can be removed by laminar flow of the cooling gas. We combine this with an effective duty factor of 50-100 to calculate the maximum average power in the barrel.

Timing resolution affects the number of overlapping events that occur when the detector is read out. Here there is a tradeoff between speed and front-end signal-to-noise and power. Fortunately, the low capacitance and high signal-to-noise ratio of a finely pixelated sensor allows for acceptable power dissipation for single-crossing ($\approx$ 300-700 ns) time resolution. Therefore our baseline design assumes single-crossing time-resolution.

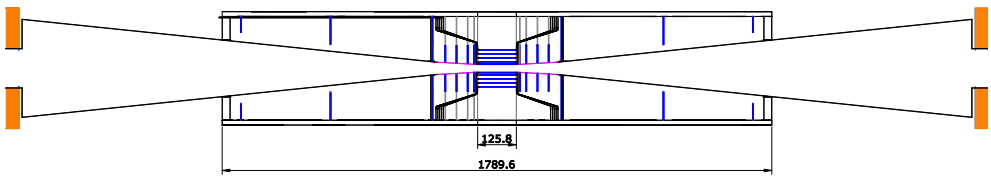

Figure 2.1.1: Layout of the vertex and forward tracking region, including carbon-fibre support and forward cone. Dimensions are in mm

2.2 Baseline Design

Given the significantly extended physics reach that can be achieved with superb vertex reconstruction – primary, secondary and tertiary – the vertex detector for SiD is proposed to be an all-silicon structure in a barrel-disk geometry. Side views of the vertex detector are shown in Figures 2.1.1 and 2.2.1.

The geometry parameters of the vertex detectors are summarised in Table 2.2.1. The five barrel sensor layers are arranged at radii ranging from 14 to 60 mm. The vertex detector

also has four disk layers supported by carbon-fibre support disks at z positions ranging from about 72 to 172 mm. The innermost disk covers radii from 14 mm out to 71 mm. Forward tracking continues beyond the vertex detector proper with three additional small pixel disks, extending in z from about 207 to 832 mm. The vertex barrel and inner endcaps have $\approx 20 \times 20$ µm pixels. The pixel size increases to $\approx 50 \times 50$ µm for the forward tracker disks. The total area of the vertex barrels is 1.63×10^5 mm^2 and is 0.59×10^5 mm^2 for each set of 4 inner pixel disks and 1.96×10^5 mm^2 for each set of 3 forward pixel disks. The simulation described in the following chapters assumes 0.1% radiation length per layer excluding cables and 20×20 µm pixels for the forward tracker disks.

Table 2.2.1: Parameters of the vertex detector. Units are mm.

Barrel	R	z_{max}	
Layer 1	14	63	
Layer 2	22	63	
Layer 3	35	63	
Layer 4	48	63	
Layer 5	60	63	
Disk	R_{inner}	R_{outer}	z_{center}
Disk 1	14	71	72
Disk 2	16	71	92
Disk 3	18	71	123
Disk 4	20	71	172
Forward Disk	R_{inner}	R_{outer}	z_{center}
Disk 1	28	166	207
Disk 2	76	166	541
Disk 3	117	166	832

2.2.1 Sensor Technology

There are a number of possible choices of sensor technology for the vertex detector, including 3D integrated sensors and readout chips [4], Silicon-on-insulator (SOI) [5], Monolithic Active Pixels (MAPS) [6, 7], hybrid pixels [8, 9], and DEPFETs [10]. All of these technologies have the capability of delivering sensors less than 75 µm thick with 5 µm hit resolution

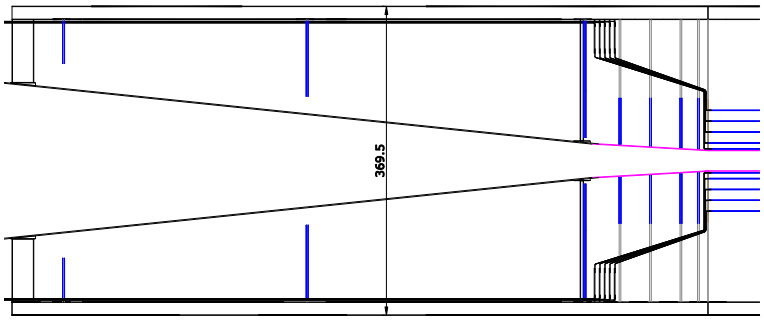

Figure 2.2.1: R-z view of the vertex detector and its support structure. Cable routes are also shown with DC-DC converters located on the support structure near the end of the first set of pixel disks. Dimensions are in mm.

and low power consumption. They are also changing rapidly with advances in microelectronics. The vertex detector is physically small and SiD is designed to make insertion and removal of the vertex detector straightforward. These factors motivate postponing a decision on the details of sensor technology for the SiD vertex detector to a date as late as possible in the final design process. In this document we have chosen 3D technology to provide a definite reference for the detector design. Other choices would differ in details of the mechanical and electronic design of the vertex detector but would not affect the overall design philosophy. To achieve minimum mass in the barrel ladders we are exploring an all-silicon assembly as the baseline. Alternatives include foam-based ladders as explored in the PLUME collaboration [11], and carbon-fibre supports as prototyped at Fermilab.

2.3 3D-Based Module Design

In microelectronics, 3D technology refers to the stacking of multiple layers of circuitry with vertical interconnections between them. This area is developing rapidly as a way of increasing circuit density without the major re-tooling and investment needed for smaller feature sizes. The enabling technologies for 3D are wafer thinning, wafer bonding, and the formation of Through-Silicon Vias (TSVs). Although the increased circuit density provided by multi-layer circuits is in itself an important application for High Energy Physics, it is the increased range of processing and interconnection options provided by technology that offers the largest potential [12]. Using these technologies arrays of chips can be bonded to sensors and electronics to form essentially monolithic arrays of sensors with no dead space between chips and with interconnections taken from the back rather than the edge of the IC.

Chip-to wafer technologies such as Direct Oxide Bonding (DBI) from Ziptronix [13] also promise lower cost and much finer pitch (4 μm has been utilised for the Fermilab wafers) than conventional bump bonding. Heterogeneous layers of different technologies can be combined in a 3D stack to optimise overall sensor performance.

Combining 3D with active edge processing can result in fully active tiles which can be used to populate detector arrays in a variety of geometries with small dead regions. This is especially important for the forward disks where tiling will allow full coverage with minimal dead area.

2.3.1 Active Edge Devices

Active edge sensors are an outgrowth of work done to develop 3D silicon sensors, which provide good charge collection combined with radiation hardness. The technique utilises a deep reactive ion etch of silicon to create a nearly vertical trench with smooth edges. The high quality of the trench wall avoids charge generation normally associated with saw-cut edges [14]. The trenches are filled with doped polycrystalline silicon. Combination of active edge technology with 3D integration can provide a technique for tiling sensor arrays with low mass and high yield. Readout wafers are oxide bonded to sensor wafers with active edge processing. The resulting stack is thinned to expose the Through-Silicon-Vias and the handle wafer is removed by grinding and etching. This results in active tiles with coarse pitch bump-bond connections for readout. Using such tiles, large-area pixelated modules with complex shapes can be assembled with known good integrated sensor/readout dies and with large-pitch backside bump-bond interconnects. All fine-pitch bonds to the sensor are made using wafer-to-wafer oxide bonding. This is particularly useful for the pixel disks, where we want to populate an $\approx$18 cm radius disk with IC reticule ($\approx 2.5 \times 2.5$ cm) sized objects.

2.3.2 Barrel Sensor Interconnect to Readout

Any complex, pixelated device will require integration of sensors with readout chips whose size is limited by the reticle area of the CMOS process. There are several choices if we wish to fabricate a 12 cm long ladder. A ”stitching” process modifies the reticules to allow reticule to reticule connections on the wafer, by double exposing an overlap region to form connections. The yield of the stitched array is the product of the individual yields. Active tiles can be bonded to a thin substrate which provides power and signal routing. There is a mass penalty associated with the backing structure. A third process, which we have chosen as the baseline, uses sensor wafers bonded to matched 3D wafers. The resulting stack is thinned and the readout and power connections are fabricated on the top aluminium layer

of the readout IC layer. This results in minimum mass ladders with no additional material needed for support.

Our design includes a number of features which have been or are being demonstrated, but full ladders have not yet been assembled. The design is based on active-edge SOI sensors bonded to readout chips with Through-Silicon-Vias [15]. Similar results can be obtained with SOI sensors utilising the handle wafer as a sensor, or MAPS-type designs. A possible process would include:

1. Fabricate sensor wafer as an SOI stack with a 50 µm thick sensor bonded to a thick handle which will be removed after processing. Trenches are etched in the perimeter of sensors to provide the active edge.

2. Fabricate ReadOut Integrated Circuit (ROIC) Through-Silicon-Vias wafers with reticule pitch matched to the sensors.

3. Oxide bond ROICs to sensors with seed metal routing to match a smaller ROIC pixel pitch at the edges. This allows for the regions near the edges of reticules to be used for test structures and alignment.

4. Thin the stack to expose the Through-Silicon-Vias. Pattern the top layer to provide bussing to all power and readout connections. Form bump bond pads near the edges.

5. Etch the regions at the sensor periphery to singular the individual sensors.

6. Backgrind and etch the wafer to remove the handle.

Figure 2.3.1 shows the wafer stack structure before and after thinning and singulation. This process is very similar to work currently being done at VTT and Ziptronix to demonstrate active-edge tile fabrication. The only significant difference for SiD would be the thickness of the sensor (50 vs. 200 µm) and bonding of multiple reticules to a single sensor. Alternatives, such as carbon-fibre or foam supports would simplify the process at some expense in mass.

2.3.3 Sensor tiling for disks

The ROIC/sensor bonding process for the four forward pixel disks is similar to that used for the barrel ladders except that single reticules are bonded and singulated. Each tile has a set of bump bonds distributed on the back side for power and readout interconnect. The tiles are bump bonded to a carbon-fibre backing plate co-cured with a Kapton circuit which provides routing to external connections. The four different inner radii of the disks would require four different reticule layouts. A optimised final design might utilise identical disks to minimise the varieties of layouts.

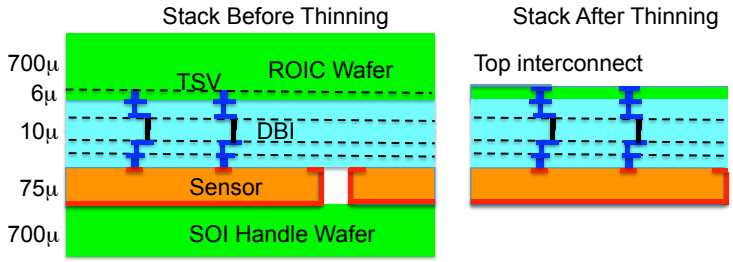

Figure 2.3.1: Wafer stack structure before and after thinning and singulation.

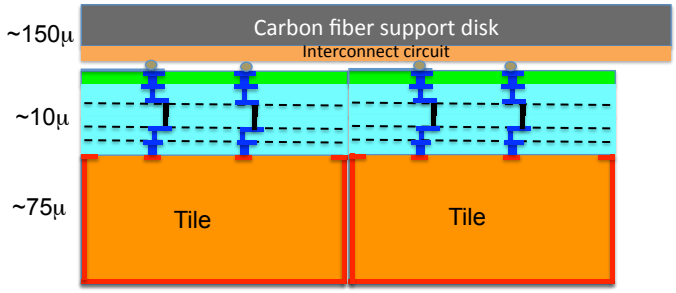

Figure 2.3.2: Tiled structure used for the disk layers utilising a carbon-fibre backing disk.

A similar layout can be used for the forward pixel disks at large z. Figure 2.3.3 shows a possible tiling which utilises only two reticule types. In this design the outer disk would use two rows of tiles, the middle would use four and the inner would use six. The active edge technique has the additional advantage that edges are formed by etching rather then saw cutting, so the trapezoid shapes can be fabricated easily.

2.4 Support structures and Integration

The vertex subsystem is supported by a double-walled carbon-fibre cylinder (Figure 2.4.1) which serves multiple functions. In addition to supporting the vertex detector barrels and disks the cylinder stiffens the beampipe in the vertex region, serves as a cooling gas transport and manifold, and provides locations to mount cables and power converters.

To allow assembly about the beampipe and later servicing, the vertex detector is split at the level of the horizontal plane into top and bottom sub-assemblies. To accommodate the sensor geometry, the split line is offset between the right and left hemisphere. Once

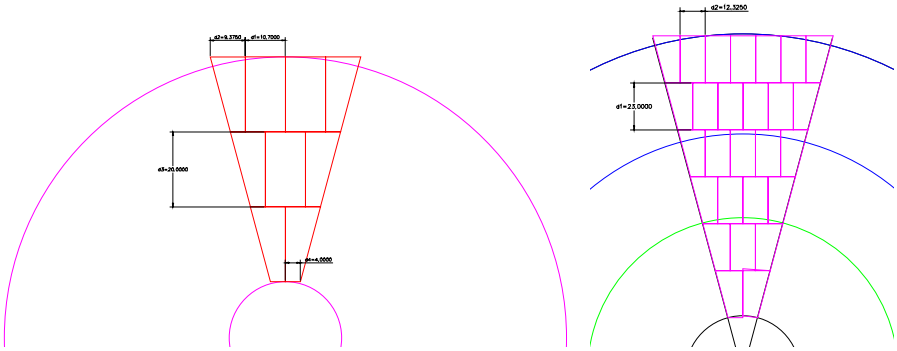

Figure 2.3.3: Design of the reticule-based tiling for the innermost pixel disk (left) and for the disks at large z (right) with inner radii of 28 (black), 76 (green) and 117 (blue) mm and an outer radius of 166 mm.

mated, the two sub-assemblies are supported from the beam pipe and stiffen the portion of the beampipe passing through them.

To prevent bending of the small-radius portion of the beampipe and ensure good stability of the vertex detector position, the outer vertex detector support cylinder is coupled to the beampipe at four longitudinal locations: $\pm$ 21.4 and $\pm$ 88.2 cm. The support cylinder is separated into top and bottom halves, as are all vertex detector structures. Inner and outer support cylinder walls are 0.26 mm thick. They are made from four plies of high-modulus carbon-fibre resin pre-preg. Wall separation is 15 mm.

During silicon tracker servicing the vertex detector and beampipe remain fixed while the outer silicon tracker rolls longitudinally. To allow for that motion and to permit the outer silicon tracker elements to be at the lowest possible radius, the outer radius of the vertex detector, including its support structures, has been limited to 18.5 cm. Additional space for any additional thermal insulation which might be needed, has been foreseen. To maximise the physics potential, the inner radius of vertex detector elements has been chosen to be as small as possible, while still being consistent with beam-related backgrounds and the beampipe profile. In the barrel region, the minimum radius to a sensor surface is 1.4 cm, governed by the beam backgrounds.

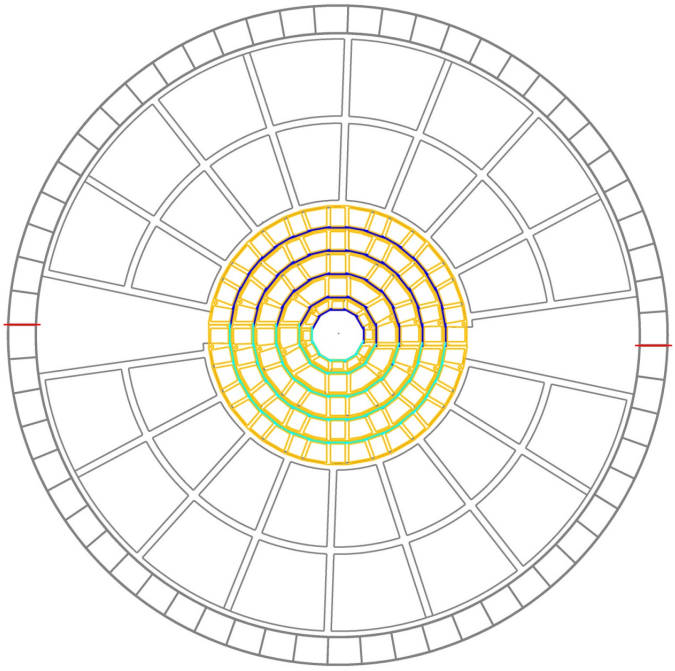

Figure 2.4.1: End view of the vertex support cylinder showing ribs and cooling gas passages, internal stiffening web structures, and the barrel vertex detector. Top and bottom sections of the barrel are shown in blue and green.

2.4.1 Power delivery

Readout Considerations

The vertex detector readout is illustrated using the scheme with in-pixel storage of analog information and digital time stamps used both in the 3D-VIP or the Chronopixel chip [16]. In this scheme analog and digital information is stored within a pixel during the bunch train and read out between bunch trains. The pixel complexity is minimised by storing the address information on the periphery of the chip. Table 2.4.1 summarises the power consumption of this readout scheme. Electrical connections of about one meter from the ladders to optical links installed on the support tube have been assumed. Assuming 32 bits are used per hit and 100 pF interconnect capacitance at 1.5 V, the local readout consumes 0.24 W of average power. If each of the 108 ladders is independently driven using a 200 MHz clock, the inner layers would dominate the readout time at 75 ms/ladder. The bit rate from the entire vertex detector is about 2 Gbit/s.

Table 2.4.1: Readout rates for the vertex detector.

Layer	Ladders	hits/crossing	bits/train	Readout time (s)	Readout Power (W)	Analog Power (W)
1	12	2000	1.8×10^8	7.5×10^{-2}	0.10	1.7
2	12	1200	1.1×10^8	4.5×10^{-2}	0.06	2.5
3	20	800	7.2×10^7	1.8×10^{-2}	0.04	3.7
4	28	450	4.1×10^7	7.2×10^{-3}	0.02	5.0
5	36	400	3.6×10^7	5.0×10^{-3}	0.02	6.2

We base our estimates on the VIP chip, which utilises 6 µA per 24×24 µm pixel in steady-state operation. An effective duty factor of 80 for power pulsing leads to an average power of $\approx$120 µW/mm^2. The average power in the vertex barrel is then 19.1 W. A similar calculation yields an average power of 1.37 W/disk.

Pulsed Power and DC-DC conversion

The stringent power dissipation requirements for the vertex detector can be met by delivering power to the front-end electronics only when it is actually needed. The time structure of the ILC beam, with $\approx$1 ms bunch trains followed by $\approx$199 ms gaps, allows for power pulsing. Analog and digital circuits can be turned on and off selectively, taking into account capacitive rise and fall times of individual sub-circuits as well as the time to handle the actual data load. Bias levels, however, need to be maintained at all times.

Although the average power in the vertex detector is low, the instantaneous current during the bunch train can be quite high, especially in view of the low supply voltages in modern CMOS technologies. This results in either unacceptable voltage drops in the cables or the use of high cable masses to reduce resistance. To solve this problem, which is also a significant issue for the ATLAS and CMS detector upgrades, we plan to place DC-DC converters in the vicinity of the vertex detector. Moreover, adequate voltage regulation will be implemented in the power supply chain to avoid voltage spikes due to power pulsing. The design includes low-mass flex cables which are routed from the vertex barrel and disk modules to a location at the inner wall of the support cylinder

The powering of the SiD readout chips was studied with a one-step DC-DC buck converter providing the required voltage and current. Input to the converter is 12 V for an output of 1.2 V using an air core inductor. Test boards were constructed operating at 1 MHz with several different commercial DC-DC converter chips. Tests with ATLAS tracker sili-

con strip detectors [17, 18] indicated that the electrical noise is primarily electrostatic and can be shielded by a 20 µm Al foil. To further reduce the mass, higher frequency operation of the inductor and the buck converter is required. The portable platform industry (smartphones, tablets, etc) currently uses DC-DC converters operating up to 6 MHz, while 20 MHz converters are in the R&D stage.

2.4.2 Cooling

Cooling in the SiD vertex detector is based on forced convection with dry air. The flow for barrel cooling is assumed to be from one barrel end to the other. For a study of the heat dissipation and cooling, the average power dissipated in a sensor was taken to be131 $\mu W/mm^2$. That corresponds to a total power of 20 W for the five barrel layers. These numbers presume power pulsing. Power is assumed to be distributed uniformly over the sensor active surface and both sensor surfaces participate in heat removal. The supply air temperature was taken to be -15 ^{0}C. For a given sensor, heat transferred inward through the carbon-fibre support was taken to be proportional to the surface contact between the sensor and carbon fibre. Thermal impedance through silicon, epoxy, and carbon-fibre laminate has been included, but turns out not to be very significant. The remaining heat was assumed to be transferred outward into the layer to layer gap. For flow and heat transfer calculations, the gap between barrel layers was taken to be 1 mm less than the nominal layer spacing and laminar flow was assumed.

In the gap between the innermost layer and the beam tube, flow is likely to be lower and temperature higher, once supply and return distribution patterns of air flow have been taken into account. Higher flow rate clearly improves the uniformity of sensor temperatures and reduces the difference between the sensor temperature and the cooling air. All flow rates which have been considered lead to temperature variations which should be acceptable for dimensional stability, which is crucial for high-precision vertexing. The time-dependent effects of power cycling remain to be investigated. Those depend on the thermal mass in the barrel and the details of the power cycling.

The outer support cylinder of the vertex detector offers a natural thermal enclosure. Details of end openings in barrel membranes remain to be included. Those openings provide a mechanism for adjusting relative flow between barrel layers. A membrane between the outermost barrel layer and the vertex support cylinder will ensure that flow does not excessively bypass the barrel-to-barrel gaps. Similar calculations have been made to understand disk cooling. Those calculations are based on barrel results with a Reynold's number of 1800 (barrel flow = 20 g/s). Heat removal calculations for the first four disks at each end of the barrel assume the same power per unit area as the pixel sensors of the barrel. The result is a total power of 16.9 W for all eight disks and an air flow of 16.4 g/s.

We propose to deliver air via the outer support cylinder. To allow that, the two walls of the cylinder are separated by radially-oriented ribs running along the full cylinder length. The calculations assume ribs at 60 azimuths. Openings, each approximately 12.2 mm $\times$ 15 mm, at 18 z-locations in the inner cylinder wall distribute the flow to the various disk locations and to the barrel. At each azimuth, the cell through which flow passes was approximated by a rectangle of height 15 mm and width 18.2 mm. The wall thickness was assumed to be 0.26 mm for both cylinders and for all ribs. The results gave a Reynold's number of 3105 in the portion of the cell which sees full flow, indicating turbulent flow. Since a portion of the flow exits the cell at each opening, the Reynold's number drops to 1725 at approximately z = 51.9 cm (a short distance inboard of the two outermost disks). While entrance effects may remain, the flow should gradually become laminar after that point. Supply and return connections to the outside world remain to be fully evaluated. With eight connections per end, each represented by a 20 mm $\times$ 40 mm rectangular passage, the Reynold's number is 12900 and flow is turbulent.

2.4.3 Cabling

We plan to utilise low-mass strip line cables based on aluminium conductor for signal communication and power distribution from the sensors to the DC-DC converter region. The inner ends of the cables will be wire bonded directly to the sensor ladders.

In the DC-DC converter region signals will be converted to optical fibres. Power will be brought into the vertex region at $\approx$ 12 V by aluminium cables which make the transition to copper outside the tracker volume.

Varying Lorentz forces due to pulsing of the power are a particular concern. This is minimised by utilising balanced supply and return lines and twisted wires where appropriate. We will utilise a three-layer strip-line design with centre supply and outer return traces to minimise forces on the cables [19]. Tests of mechanical forces and vibration are planned utilising KPiX chips and a 7 T magnet available at Yale. The pulsed power frequency, 5 Hz, is significantly below the resonance frequency expected for major support structures.

2.5 R&D Status

2.5.1 Chronopixel

We have developed a design, in collaboration with SARNOFF Research Labs, for the Chronopixel devices that satisfy the ILC requirements [16]. The design of the ultimate device requires high resistivity silicon (5 kΩ-cm) with a 15 µm thick epilayer and pixels

of 10 × 10 to 15 × 15 µm which will require to use 45 nm technology. The 45 nm technology is currently too expensive for prototyping, so we foresee a series of prototypes that approach the ultimate design. The first prototype has been designed, fabricated and extensively tested. The second prototype has recently been fabricated and the testing of these devices is just getting started.

2.5.2 VIP 3D Chip

The Vertically Integrated Pixel (VIP) ASIC was conceived of as a demonstration readout chip for the ILC vertex detector [20]. The Lincoln Laboratory process has the advantage of very well-established wafer bonding and thinning, but the fully depleted SOI process is not well suited for analog applications and has larger feature size than advanced commercial processes. The final Fermilab designed ASIC (VIP2a) using this process was received and tested late in 2009. The analog front end of VIP2a, which was laid out using design rules modified at Fermilab based on failings of the earlier prototypes, worked well, as did all of the interconnections between circuit layers.

A second iteration, the VIP2b was fabricated in the 3D process developed by Tezzaron/Global Foundries. This process uses a bulk 0.13 µm CMOS IC process with modifications to allow the top copper metal layer to be used for face-to-face wafer bonding, and to include vias that extend 6 µm into the bulk material. After wafer bonding, one of a pair of wafers was back thinned to expose the deep vias, and metal pads deposited that are suitable for wire bonding or for further wafer bonding. We now have chips with successful 3D bonds between tiers. Initial testing of the 2D parts show excellent analog performance. Tests of the full functionality of the 3D chips are underway.

2.5.3 Thinned hybrid detector with high-density interconnect

An alternative option for a low-mass vertex detector combines thinned high-functionality readout ASICs with thin high-resistivity sensors, assembled using advanced low-mass interconnect technologies. For the ASIC the 65 nm deep sub-micron technology was successfully assessed, through the design and production of relevant pixel readout sub-circuits [21]. Subsequently a fully functional test chip has been designed in 65 nm technology. It comprises 64 × 64 pixels of 25 × 25 µm size providing time-of-arrival and time-over-threshold functionality [22]. The ASIC foresees individual power pulsing of its analog and digital circuits. It has been submitted for production at the end of 2012. Development has been initiated towards low-mass fine-pitch flip-chip interconnect based on copper pillars. Module assembly is foreseen to make use of Through Silicon Vias (TSV) to carry interface signals to the backside of the pixel chip. This will offer 4-side buttable pixel chips, enabling the

assembly of large-area pixel detectors with minimal dead space between individual pixel tiles. The TSV technology has meanwhile been applied successfully on Medipix3 chips manufactured using a 130 nm process [23].

2.5.4 Active Edge Tiles

Active tiles are central to the conceptual design of the forward disks. A program to demonstrate these devices is underway in collaboration with Fermilab, SLAC, and Cornell University. Sensors of 200 µm thickness are being fabricated on SOI wafers by VTT and planar dummy top wafers with tungsten contacts are being fabricated by Cornell. The two will be wafer-bonded by Ziptronix and this stack will be singulated and thinned by SLAC. We expect the VTT wafer to be complete by the end of 2012.

2.5.5 Critical R&D

By the conclusion of the current round of R&D, we expect to have demonstrated the basic sensor and IC technologies needed for SiD. The next logical step would be to develop a full sized ladder for the barrels and a wedge segment for the disks. We need to build prototype support structures, including the double walled outer cylinder and barrel and disk supports. We also would need to demonstrate the integration of ladders and wedges into barrels and disks, initially with one live and several dummy sensors. Finally, a full-sized prototype with heating elements would allow us to study air cooling and confirm flow and temperature calculations.

Studies of power delivery and cabling are critical. We would like to demonstrate a low-mass cabling system, including aluminium conductors, DC-DC conversion, and optical interconnects in the context of a full sized mechanical prototype. Again, many of the individual technologies have been demonstrated by the LHC experiments, the RHIC projects, or in ILC detector R&D, but a complete system has yet to be demonstrated.

2.6 Summary

The basic concepts in the SiD Vertex detector, low-mass mechanical designs, the split cylinder support structures, and the barrel/disk geometry are essentially unchanged from the SiD LOI. However, more detailed designs for cabling, power conversion, sensor technology, and mechanical supports and cooling are included in this report. Most of these components are, or will soon be, ready for the module prototype phase. At that point decisions would need to be made on tradeoffs such as the lower mass, but more challenging, all-silicon design vs a design which has carbon-fibre or foam supports and, ultimately, sensor technology.

Chapter 3

Silicon Tracking

3.1 Introduction

The outer tracker of the SiD detector is a large all-silicon tracking detector filling the space between the vertex detector and the electromagnetic calorimeter. The tracker comprises five cylindrical barrel layers, with the four outer layers closed at the ends by conical, annular disks, as shown in Figure 3.1.1. In the baseline design, the barrels are tiled with modules

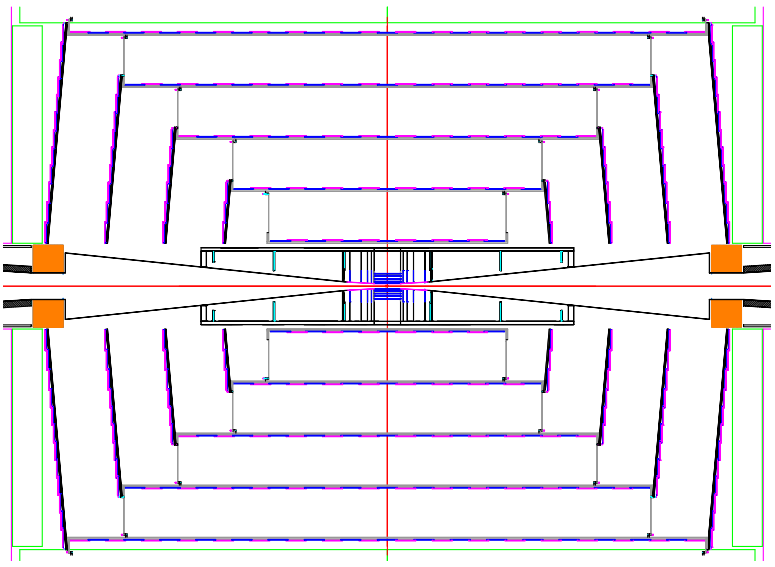

Figure 3.1.1: $r-z$ view of the vertex detector and outer tracker.

hosting a single micro-strip sensor for axial-only measurement, while the disks are tiled with modules having a stereo pair. These cylinders are nested, connected by annular rings at the ends of each, to create a single unit supported from the ends of the ECAL. The design of the outer tracker is summarised in Table 3.1.1 and more details of the design may be found here [1]. The coverage of the SiD tracking system is shown in Figure 3.1.2 as a function of

Table 3.1.1: The layout of the outer tracker.

Barrel Region	R (cm)	Length of sensor coverage (cm)	Number of modules in ϕ	Number of modules in z
Barrel 1	21.95	111.6	20	13
Barrel 2	46.95	147.3	38	17
Barrel 3	71.95	200.1	58	23
Barrel 4	96.95	251.8	80	29
Barrel 5	121.95	304.5	102	35
Disk Region	**z_{inner} (cm)**	**R_{inner} (cm)**	**R_{outer} (cm)**	**Number of modules per end**
Disk 1	78.89	20.89	49.80	96
Disk 2	107.50	20.89	75.14	238
Disk 3	135.55	20.89	100.31	438
Disk 4	164.09	20.89	125.36	662

the polar angle. At least six hits are measured for all tracks with a polar angle down to about 8°. For polar angles above 13° ten layers or more are traversed.

The goals of the ILC physics program impose performance requirements on the tracking that exceed those met by any previous system and are summarised in Table 3.1.2. In particular, the need for excellent momentum resolution over a broad p_T spectrum creates significant design challenges. For high p_T tracks superior position resolution and mechanical stability are required. For low p_T tracks, an aggressive material budget is critical. Meanwhile, the need for high efficiency over a wide range of momenta and large solid angle motivates an integrated approach to tracking: the vertex detector, outer tracker and calorimeter are designed to work in concert to achieve these goals robustly but with a narrow margin of extra layers that result in unnecessary material.

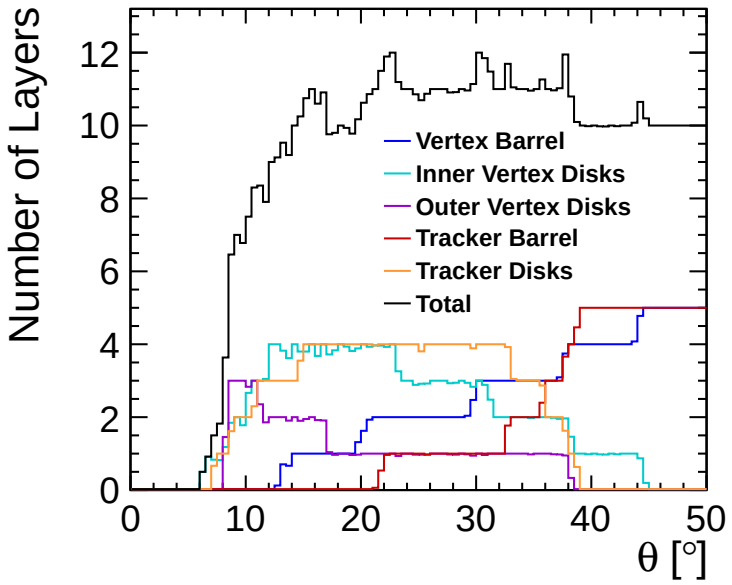

Figure 3.1.2: The coverage of the SiD tracking system as a function of the polar angle θ.

3.2 Baseline Design

The baseline design uses relatively conventional technologies to achieve the performance goals with low risk and minimal cost. The sensors are single-sided micro-strips. The barrel and disk supports, as well as the module supports are composites of carbon fibre and low-density Rohacell 31 foam. Low mass hardware is fabricated in poly ether ether ketone (PEEK).

There are, however, some key elements where novel solutions are required. The sensors, like those for the ECAL, employ a double-metal layer to route signals to bump-bonding arrays for readout by the KPiX ASIC [24, 25, 26]. As with the ECAL, traces on the second metal layer of the sensor connect power and signal lines on the KPiX chip to a readout cable that is also bump bonded to the face of the sensor. This arrangement eliminates the material and assembly complexity of hybrid circuit boards to host the readout electronics. The low power dissipation of KPiX makes gas cooling feasible, reducing further the required material. However, since KPiX achieves low power consumption through power pulsing with a duty cycle of approximately 1%, the instantaneous currents required to power the

Table 3.1.2: Performance goals for the outer tracker.

Parameter	Design Goal
coverage	hermetic above $\theta \sim 10^{\circ}$
momentum resolution $\delta(1/p_{\mathrm{T}})$	$\sim 2-5\times 10^{-5}/GeV/c$
material budget	$\sim 0.10-0.15\mathrm{X}_0$ in central region
	$\sim 0.20-0.25\mathrm{X}_0$ in endcap region
hit efficiency	$> 99\%$
background tolerance	Full efficiency at $10\times$ expected occupancy

tracker are still large and require significant mass of conductor. Concentrator boards located on the support rings at the ends of each barrel host DC-DC converters to transform high voltage, low current input power into low voltage, high current power for the modules, thus minimising the conductor and cross-sectional area required to deliver power into the these boards from outside the tracking volume.

3.2.1 Barrels

A set of five cylindrical layers provides tracking coverage in the central portion of the detector. Each cylinder is formed from a sandwich of carbon fibre and Rohacell cured as a single unit, similar to those used in the DØ CFT and the ATLAS SCT [27]. The inherent rigidity of the cylinders allows for holes to be cut where allowed by module mounting locations to further reduce the average material experienced by passing particles without significantly compromising rigidity. However, it should be noted that such measures to reduce the material in the barrel and disk supports are not included in the current simulation or material estimates shown here. The outer surface of each cylinder is populated with PEEK mounting clips for the modules that allow the insertion and extraction of individual modules without the use of tools, facilitating module replacement without complete disassembly of the tracker. The normal to each module is tilted with respect to the radial direction to allow for overlap between modules that are adjacent in ϕ and partially compensate for the Lorentz direction. Adjacent modules in z alternate between inner and outer mounting positions to provide longitudinal overlaps. Excluding overlaps, the material presented by a single barrel layer is approximately 0.9% X_0 for tracks at normal incidence.

The modules themselves comprise a single sensor, read out via two bump-bonded KPiX ASICs and a short polyimide cable supported by a composite support frame. A picture of a prototype sensor and cable is shown in Figure 3.3.1. The sensors are single-sided, poly-

biased, AC-coupled, micro-strip sensors fabricated on 300 μm thick, p+ on n bulk, high resistivity silicon. The nominal sense(readout) pitch is 25(50) μm, with the intermediate strips capacitively coupled to readout strips to improve single hit resolution. The KPiX chips bonded to the surface of the sensor, described more fully in Chapter 4, store time-stamped hits from the tracker exactly as for the ECAL sensors, for readout between bunch trains. Traces on the second metal layer of the sensor connect power and signal lines on the KPiX chip to a short readout cable, or pigtail, that is also bump-bonded to the face of the sensor. These copper-on-polyimide cables have tabs that provide bias voltage to the edges of the sensors and have micro-connectors that mate to the extension cables running along the surface of the cylinder to the concentrator boards located at each end. Great care has been taken to model the conductor required for each cable run and the stacks of cables required for each layer to arrive at realistic material estimates.

The back side of the sensor glues to the face of a module support frame that comprises a pair of carbon composite sheets sandwiched around a thin sheet of Rohacell 31. This frame is approximately 50% void to reduce material and is passivated to isolate the carbon fibre from the high voltage on the back side of the sensor. A set of three spheres around the periphery of each frame provide a three-point kinematic mount to the mounting clips on the outer surface of the barrel cylinder. A small handle on each module provides a strain relief for the pigtail as it leaves the module and a safe handle during assembly and installation.

3.2.2 Disks

The outer four barrel cylinders are partially closed at each end by slightly conical, annular disks that extend the coverage of the outer tracker to the forward regions. These disks are fabricated using a carbon fibre and Rohacell 31 sandwich similar to that of the barrel cylinders. As with the barrel cylinders, the outer surface of the endcap disks are covered by a set of PEEK mounting clips that hold the disk modules. Adjacent modules in ϕ alternate between inner and outer mounting positions to provide overlap. The modules, with normals along z, step along the 5 degree slope of the cone to provide radial overlap. Excluding overlaps, the material budget for a single disk layer is approximately 1.3% X_0 for tracks at normal incidence.

The endcap modules are similar to those for the barrels, but have sensors on both sides of the module frames to provide a stereo measurement. The sensors on each side are identical trapezoids with strips parallel to one edge, but are technologically identical to those used in the barrel. A smaller sensor is used for small-radius portions of the disk, while a larger sensor is used in the larger radius regions. As in the barrel, short pigtail cables bonded directly to the sensors connect to extension cables that transmit power and data to concentrator boards mounted at the outer radius of each disk. The layout of the outmost disk is shown in

Figure 3.2.1.

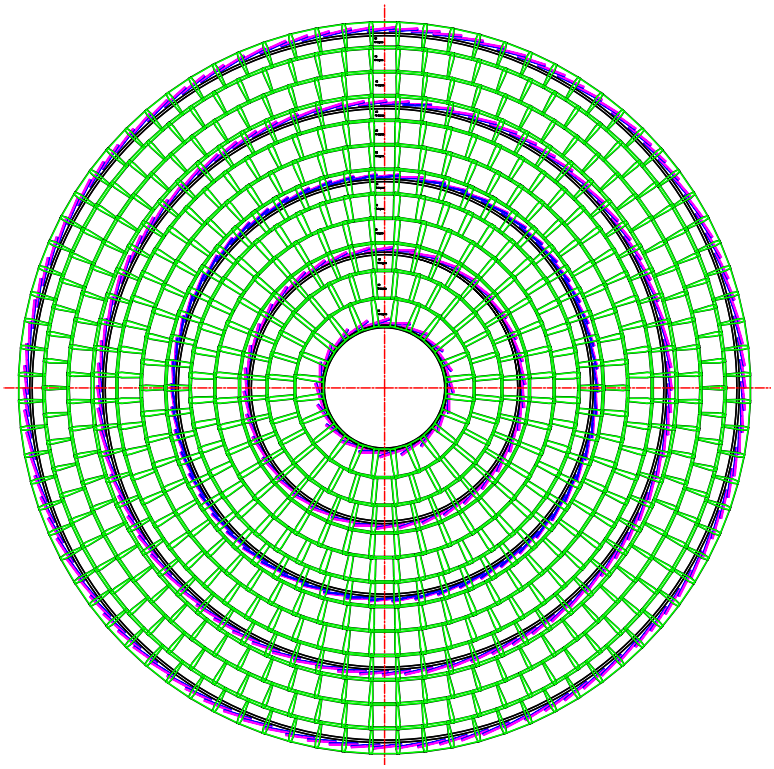

Figure 3.2.1: Rφ projection view of the tracker barrels and disks.

3.2.3 Barrel/Disk Integration

The barrel cylinders are nested, one inside the other, with spoked annular rings at the ends of each cylinder supporting it from the inside surface of the next cylinder outward. The outermost cylinder is mounted to the inside surface of the ECAL barrel. The disks that close the ends of the barrels mount to the inside circumference of these same rings, extending beyond the barrel radii to provide overlap between the barrels and disks. On the outer faces of these support rings are the concentrator boards that connect to all of the individual modules. Each board hosts charge storage and DC-DC conversion to provide pulsed power to at least ten sensors as well as distribution of clock and control signals and electrical to optical conversion of signals to concentrate data output. With high-voltage low-current power and optical transmission of data, the cable cross-section needed to service the concentrator boards for

the entire detector is minimised, improving the hermeticity of the detector at the barrel-disk transitions. In order to spread out the material in the concentrator boards and support rings, the barrel-disk transitions of the different layers are non-projective. The impact of the concentrator boards on the material budget can be seen in Section 10.3, which includes a graph showing the material inside of the ECAL as a function of polar angle.

3.3 Critical R&D

The outer tracker embraces conventional technologies where possible to minimise the risks and costs of the system and minimise the R&D necessary to bring it into production. However, there are a few key areas where exploring new technologies, targeted at addressing specific performance limitations, is critical to meeting the performance goals for the tracker. These technologies focus on minimising the material in the tracker necessary for low-momentum resolution while maintaining the mechanical stability required for high-momentum resolution. The key R&D projects then relate to silicon readout, data transmission, power, cooling and the mechanical stability of the tracking system.

The key to minimising the material in the tracker is the KPiX readout. As a result, development of KPiX and the critical elements of the readout chain is of great importance. In addition to development of KPiX itself, this encompasses a number of critical tasks: bump bonding KPiX to sensors, development of sensors and cables, and development of the complete DAQ chain. Because the tracker is technologically identical to the ECAL in all of these respects, R&D for the tracker is undertaken together with KPiX R&D for the ECAL and is largely described in Chapter 4. However, with a very different set of requirements, the implementation for the tracker still differs in some respects that motivate tracker-specific R&D. This R&D has focused first on producing prototypes of a barrel module, since that is the simplest module needed for the tracker and solutions developed there apply directly to the key issues for the disk modules.

With the requirement of full efficiency for minimum ionising particles and excellent single-hit precision, the signal-to-noise ratio must be maximised. Achieving the goals for the design requires a signal-to-noise ratio in excess of 20. This, in turn, sets the requirement for the noise performance of KPiX and necessitates sensors with the lowest possible readout capacitances and resistances. Prototype sensors, as shown in Figure 3.3.1, were fabricated by the Hamamatsu Photonics Corporation and meet expectations for the parameters that define the noise performance. Meanwhile, successive generations of KPiX have undergone improvements in noise performance and are now able to meet the goal, although testing of a fully assembled module will be required to verify the as-built noise performance of a module. Assembly of a full module has been awaiting recently developed interconnect

techniques for first ECAL prototypes, as described in Chapter 4.

The cable for the tracker differs somewhat from that required for the ECAL. It must have the lowest possible mass and the best possible noise performance, while servicing two KPiX chips simultaneously instead of one. A prototype cable for the tracker has been produced that meets all of the requirements, shown together with a prototype sensor in Figure 3.3.1. To speed development, this prototype cable is meant to be glued and then wire bonded to

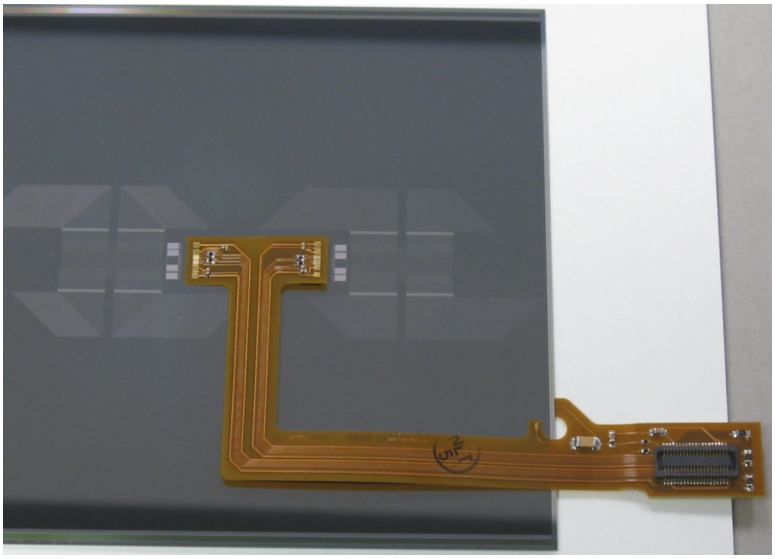

Figure 3.3.1: Prototypes of the barrel sensor and its pigtail cable shown together as they would be assembled. The bump bonding arrays for the KPiX chips and the double-metal fan outs can be seen on either side of the cable. The tab at the edge provides bias to the sensor.

the sensor, rather than bump-bonded as called for in the design. However, a processing deficiency in the prototype sensors makes them susceptible to damage during wire bonding of the readout cable. The design and fabrication of a cable for bump bonding attachment, as successfully demonstrated in the ECAL, is underway. It will enable assembly and test of full prototype modules with KPiX and sensors already in hand.

The other key to the tracker design is low mass support and cooling. While the module support frames are quite conventional, the techniques being considered for mounting these frames to the support cylinders and disks are somewhat novel. For this reason, it is important to verify the details of these designs with prototypes before considering large-scale production. In order to establish that the mounting concept is sound, testing the design with

rapid prototypes is being pursued that will allow the designs to evolve quickly. With a working prototype in hand and using standard design guidelines, it should be possible to ensure success with a high degree of confidence. However, the final step of ensuring that these parts can be mass-produced in conjunction with a third party will be expensive and likely must wait until more resources are available.

Meeting the requirements for gas cooling depends principally on meeting power consumption goals with KPiX, a milestone already achieved [1]. The requirements for other cooling loads, such as those from the concentrator boards, can already be met with commercially available components. With gas velocities of approximately 1 cm/s, the impact on mechanical stability is negligible compared with other low-mass, gas-cooled silicon detectors being assembled for other experiments. [28] However, the requirement for hermetic coverage severely restricts gas flow in some parts of the detector, and further study is required to properly engineer the cooling system.

The main issue for mechanical stability is Lorentz forces on the various elements of the tracker due to power-pulsing in the five Tesla magnetic field of SiD. In the barrel, conductors are largely parallel to the field, but the opposite is true in the disks. Development of cables with closely paired supply and return lines is a priority, and incorporation of this consideration into the next pigtail prototype is planned. Tests of modules inside a small-bore MRI magnet are being considered that would allow for the collection of critical data on these effects. The rigidity of support structures should place any resonances well above the 5 Hz excitation frequency, but the design of the detector must be mindful of any harmonics.

Charge storage and high-voltage, low-current supply to the concentrator boards greatly reduce Lorentz effects on power transmission to them from the outside, but present their own R&D challenges. Storing enough energy on the concentrator boards to provide power for a single pulse has become much more feasible as advances in high energy density capacitors have been pushed by the needs of industry. In fact, it appears likely that charge storage using a capacitor on each module may soon be feasible, which would all but eliminate Lorentz forces. Meanwhile, R&D into DC-DC conversion for the supply of future detectors has become an active field in recent years, with some work focused specifically on the needs of the ILC experiments [29, 30].

Beyond the needs of the baseline design, various efforts are continually investigating upgrades that would significantly improve the performance of the outer tracker. One such effort considers the use of resistive charge sharing to determine the position of hits along strips to the precision of a few mm [1]. While instrumentation of both ends of each strip doubles the readout and the material budgets; cost, powering, and cooling constraints do not obviously exclude this option. Another topic of active investigation is whether the entire tracker could be built using monolithic active pixel sensors (MAPS). While this would clearly result in improved tracking performance, none of the technologies being investigated

for the vertex detector can be convincingly scaled in power and cost to provide a solution for the outer tracker in the near future.

3.4 Performance

The tracking performance of the SIDLOI3 geometry has been studied using full event simulation and realistic event reconstruction of single muon as well as di-jet events. In the reconstruction of the di-jet events a realistic number of hits from incoherent pairs and hadronic beam backgrounds are overlaid [31], corresponding to one bunch crossing at 1 TeV. This assumes that the time resolution of the tracking detectors is sufficient to separate hits from different bunch crossings, a reasonable assumption for the ILC.

The digitisation of the simulated tracker hits in the silicon detectors is performed using the SiSim package [32]. Diffusion of the deposited charge in the silicon is taken into account. A nearest neighbour algorithm is used to identify the clusters which are input to the track finding. The seed tracker algorithm is used for the track finding and track fitting. This algorithm uses a strategy based approach, where several sets of combinations of three layers define the possible seed layers for the track finding. For the studies presented here "inside-out" tracking strategies are used. The two innermost vertex layers are excluded from seeding to mitigate the impact of the large number of hits from beam backgrounds on the track reconstruction time. Similarly, choosing as small a χ^2 cut-off as possible in rejecting track candidates without compromising the track finding efficiency is essential in the presence of high occupancy events.

In general a minimum of 7 hits are required to find a track. In the barrel region this requirement is reduced to 6 hits to increase the track finding efficiency for central low-momentum tracks. A secondary tracking algorithm using calorimeter stubs as seeds can be used to find those tracks from late decays with fewer hits [33]. This algorithm is not used in the performance studies presented here.

3.4.1 Tracking Efficiency

The track finding efficiency is defined as the fraction of the successfully reconstructed findable particles. The true match of the reconstructed track is determined by the majority of contributed hits. The findable particles are defined as those charged particles originating from within ± 5 cm of the IP and travelling at least 5 cm. Any additional cuts are noted in the corresponding figures. In case of multiple interactions, only particles from the signal event are considered for the track finding efficiency. Due to the small total number of hits, falsely assigned hits have a significant impact on the reconstructed track parameters.

Thus, an additional quality cut is introduced and only tracks with a maximum of one falsely assigned hit are counted as successfully reconstructed.

The dependence of the track finding efficiency for single muons on transverse momentum, p_T, and polar angle, θ, is shown in Figure 3.4.1. The track finding efficiency is nearly 100% for all tracks with a polar angle larger than 15° and a transverse momentum larger than 1 GeV. The efficiency for very forward tracks below 15° deteriorates towards the detector acceptance of about 10°, where it drops sharply. Requiring a minimum of 7 hits reduces the efficiency for 1 GeV tracks in the region between 35° and 40° by about 10%. More central tracks are found efficiently for momenta as low as 0.2 GeV. Forward low-momentum tracks for polar angles below 25° suffer from about 15% inefficiency due to the higher material budget.

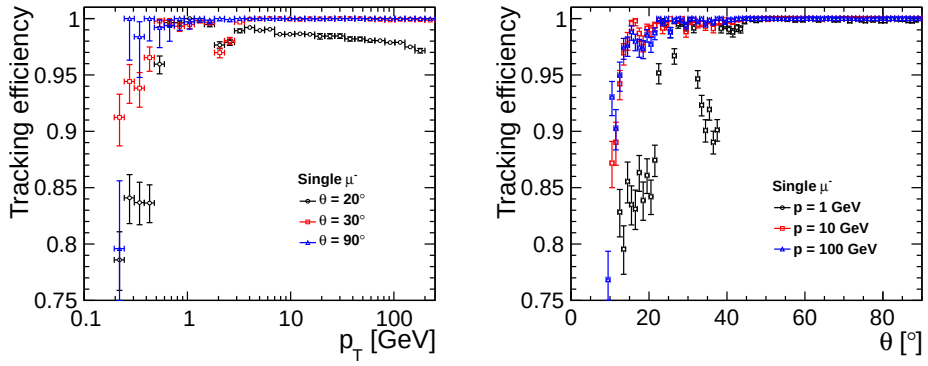

Figure 3.4.1: Tracking efficiency for single muon events in SIDLOI3 as function of the transverse momentum (left) and the polar angle (right).

The track finding efficiency has also been studied in di-jet decays of a Z' boson with mass of 1 TeV. The average tracking efficiency in these events, including beam induced backgrounds, is approximately 98%. As shown in Figure 3.4.2, the tracking efficiency is almost constant for most polar angles and transverse momenta. Similar to the performance in single muon events there is a slightly reduced track finding efficiency for low momentum tracks at a polar angle of around 40° and for very forward tracks of all momenta. In addition there is a drop in the track finding efficiency for high momentum forward tracks. These are typically in the centre of the jet and thus suffer most from confusion due to ghost hits in the stereo strip detectors.

In general the track finding efficiency is mostly limited by the total number of hits created by the corresponding particle and the local hit density, as illustrated in Figure 3.4.3. The tracking efficiency for particles within the acceptance which reach the calorimeters and thus

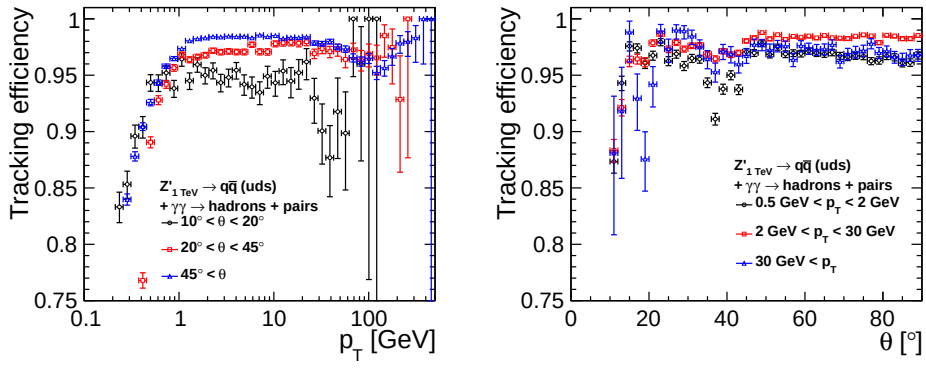

Figure 3.4.2: Tracking efficiency in di-jet decays of a Z-like particle with a mass of 1 TeV in SIDLOI3 as function of the transverse momentum (left) and the polar angle (right) of the corresponding particle. Incoherent pairs and $\gamma\gamma \rightarrow$ hadrons events corresponding to 1 bunch crossing are included.

necessarily pass through at least 10 layers is about 99%. The tracking efficiency in dense jets is limited by the strip sizes. Particles which have any other hit closer than 100 µm, which corresponds to twice the pitch of the readout in the strip detectors, have a reduced track finding efficiency. For more isolated particles the tracking efficiency is higher than 98%.

3.4.2 Fake Rates

As mentioned above, the low number of tracking layers requires a very high track purity. We thus use a strict definition of the fake rate, where all reconstructed tracks with more than one falsely assigned hit are counted as fake tracks. This fake rate is shown in Figure 3.4.4 for tracks in di-jet events including beam-induced backgrounds. Unlike the definition of tracking efficiency these rates include tracks reconstructed from background particles. The fake rate is between 1% and 3%, while high momentum tracks are more likely to have more than one false hit assigned, since they are necessarily in the centre of a jet and thus, in general, suffer from higher local hit densities. The fake rate in the forward region below 40° is lower by one order of magnitude compared to the central region. All tracker hits in the forward region have 3D information which is not the case for the barrel strip detectors.

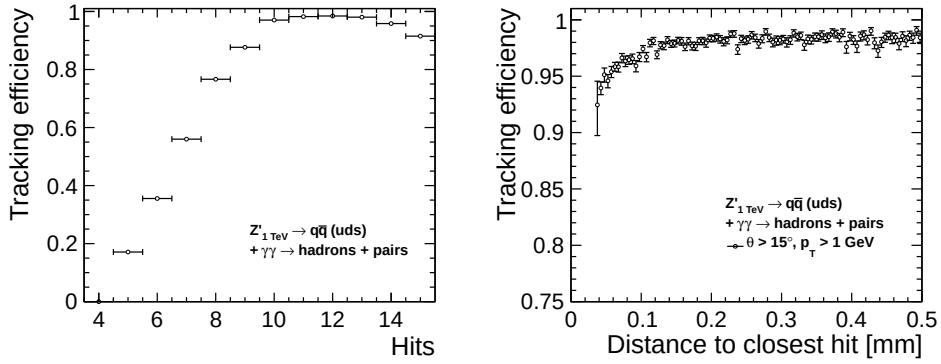

Figure 3.4.3: Tracking efficiency in di-jet decays of a Z-like particle with a mass of 1 TeV in SIDLOI3 as function of the number of hits produced by the charged particle (left) and the distance to the closest hit from a different particle (right). Incoherent pairs and $\gamma\gamma \rightarrow$ hadrons events corresponding to 1 bunch crossing are included.

3.4.3 Tracking Resolution

The normalised transverse momentum resolution achieved in the SIDLOI3 geometry is shown in Figure 3.4.5 for single muons. The data points show the width of a Gaussian fit to the $\delta(p_T)/p_T^2$ distribution of the corresponding reconstructed tracks. The dashed line represents a fit to the canonical parametrisation of the transverse momentum resolution:

$$\sigma(p_T)/p_T^2 = a \oplus \frac{b}{p \sin\theta}. \tag{3.4.1}$$

Despite the ambitious material budget, the multiple scattering term given by b dominates the momentum resolution for tracks up to 100-200 GeV. Whereas the momentum resolution for very forward tracks is limited by the short lever arm in the transverse projection, a momentum resolution of $\sigma(p_T)/p_T^2 < 10^{-4}\text{GeV}^{-1}$ is achieved for high momentum tracks at polar angles larger than 30°. Central tracks exceed a resolution of $\sigma(p_T)/p_T^2 < 2 \times 10^{-5}\text{GeV}^{-1}$.

The resolution on the transverse impact parameter, d_0, as well as the longitudinal impact parameter, z_0, is shown in Figure 3.4.6. The d_0 resolution is better than a few μm for central tracks with a momentum exceeding a few GeV. For 1 GeV muons the d_0 resolution drops to about 10 μm for central tracks. In the forward region the resolution degrades by up to one order of magnitude at the acceptance limit of $\theta \approx 10°$. The z_0 resolution has a stronger

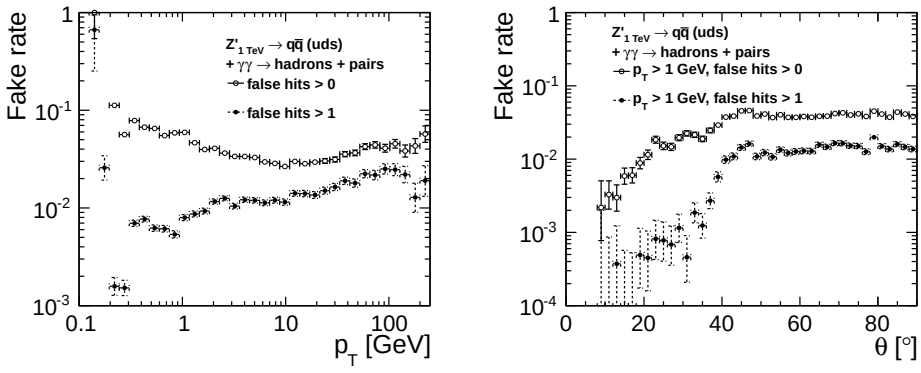

Figure 3.4.4: Fraction of reconstructed tracks with spurious hits in di-jet decays of a Z-like particle with a mass of 1 TeV in SIDLOI3 as function of the transverse momentum (left) and the polar angle (right) of the reconstructed track. Incoherent pairs and $\gamma\gamma \rightarrow$ hadrons events corresponding to 1 bunch crossing are included.

dependence on the polar angle and, while similar to the d_0 resolution in the central region, it is about one order of magnitude worse for very forward tracks. In addition, the z_0 resolution for central tracks is limited by the lever arm of the straight line fit. In the current algorithm the strip hits in the barrel region are excluded from the straight line fit which results in a very short lever arm for central tracks. More details about the tracking performance can be found in [34].

Overall the silicon tracker of the SiD concept detector, which incorporates a minimum number of layers, shows excellent performance. Tracking efficiencies in excess of 99% are demonstrated over most of the momentum and acceptance range. An asymptotic momentum resolution of $1.46 \cdot 10^{-5}$ and transverse impact parameter resolution better than 2 µm has been obtained. Even though the SiD tracker is very "thin" the studies show that the material budget still imposes limitations and a further reduction in mass is beneficial. It is expected that some of the performance features can be mitigated through a further optimisation of the overall detector design. It should be noted that the physics results presented later are based on the tracking performance as described here.

3.5 Alignment

The alignment strategy for the SiD outer tracker, vertex detector, and beam-pipe assemblies is based on:

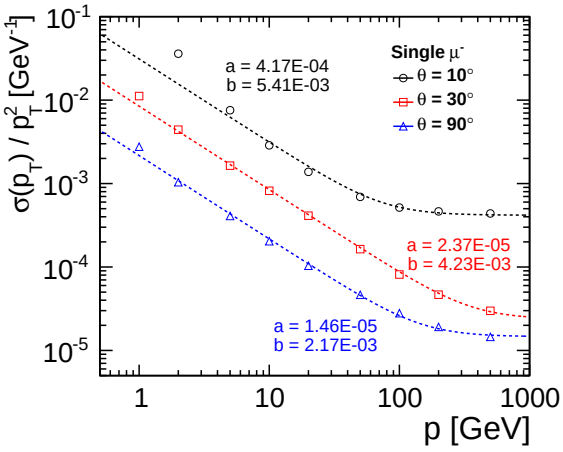

Figure 3.4.5: Normalised transverse momentum resolution for single muon events in SIDLOI3 as function of momentum. The dashed lines indicate a fit to the parametrisation given in Equation 3.4.1.

1. a small number of robust, rigid elements;
2. precise positioning of smaller components during fabrication and assembly;
3. real-time monitoring of alignment changes, including during push-pull moves; and
4. track-based alignment for final precision.

It is expected to achieve ≈20 µm relative precision among outer tracker sensor modules in different layers after fabrication and assembly in the full detector. The final precision of a few µm is attained for individual sensor modules from track-based alignment, with real-time Frequency Scanned Interferometry (FSI) and laser-track monitoring, providing both a bridge from the coarse to the fine alignment and a set of global corrections for time dependent structure motion and deformation.

The support structures for the vertex detector and tracker have been designed to minimise distortions and maintain alignment. In the outer tracker, the structure with double-walled support cylinders, concave disk support structures, and nested assembly with annular rings and kinematic mounts is intended to lead to a robust structure which can be treated as a single unit. Kinematic support from the central calorimetry is intended to minimise distortions of that structure under geometry changes of the calorimeters. In the vertex detector, double-walled support half cylinders are intended to preserve good internal alignment of

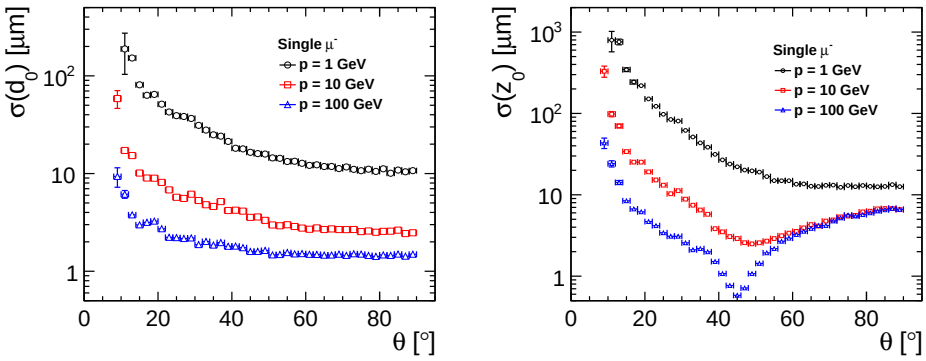

Figure 3.4.6: Impact parameter resolution $\sigma(d_0)$ (left) and $\sigma(z_0)$ (right) for single muon events in SIDLOI3 as function of the polar angle θ.

the entire vertex detector. Since the support structures deflect under beam pipe loads, substantial R&D including measurements of prototypes will be necessary to confirm that this design will work well.

Tracker alignment is expected to begin during tracker fabrication and assembly. Sensor alignment within each outer tracker module will be measured with respect to fiducials and mounting features of the module. Modules will be solidly anchored with stable relative position to stiff support cylinders and support disks, which are based upon carbon fibre laminate material. This material provides good thermal stability and should result in rigidity for the SiD tracker that is about 50 times higher than that of the CMS tracker. Predicted deflections of the support structures under gravity are small: $<$10 μm. Modules will be installed in groups with internal alignment of a group controlled to about 10 μm. Reference features on each barrel and disk will allow the positions of each group of modules to be known with respect to the reference features to about 10 μm. Hence position and orientation of a given sensor should be known to approximately $10 \times \sqrt{3} = 17$ μm. A large coordinate measuring machine (CMM) or equivalent laser-based equipment will be needed to achieve this accuracy. Frequency scanned laser interferometry during assembly offers the potential for still better knowledge of alignment than the values above. Moreover, tracker sensor modules slightly overlap within layers (and hence are tilted), which provides valuable linking of sensors within layers for track-based alignment.

We plan to use ball and cone mounts to mate barrels and disks with one another. This type of mount provides a reproducibility of 3 μm. Again, a large CMM or laser-based equipment will be used to measure reference features on each object. Precision should be about 10 μm, which implies the precision to which individual sensors are known to

≈20 μm, although individual groups of sensors will be known relative to one another with slightly better precision. Kinematic mounts will be used to support the outermost tracker barrel from the interior of ECAL. Support via kinematic mounts from some other portion of the detector has also been considered. All other outer tracker elements are supported either directly or indirectly from the outermost barrel. If the kinematic mounts are designed correctly, push-pull operations may affect absolute position of the tracker, but should not affect tracker internal alignment.

The vertex detector is supported independently of the outer tracker. Outer support half-cylinders locate all vertex detector elements relative to one another. Relative alignment of elements within either top or bottom support cylinder is likely to be better than half-cylinder to half-cylinder alignment. That suggests the two half-cylinders and detector elements they support may need to be treated as independent objects. The tracker would then be treated as three pieces: the outer tracker (including all barrel layers and disks), the upper half of the vertex detector, and the lower half of the vertex detector. Alignment of the three pieces relative to one another will be monitored via frequency scanned interferometry (FSI). A combination of frequency scanned interferometry and "laser-track" monitoring of relative sensor positions will monitor internal alignment of the outer tracker. After assembly, during data taking, and during push-pull operations, the FSI system will be run nearly continuously, providing "real time" measurement of global tracker distortions and of vibration amplitudes and frequencies (up to the Nyquist frequency of the FSI DAQ sampling). This type of monitoring may not be feasible for internal alignment of the two vertex detector halves due to constraints on the material budget.

A deformation monitoring system based on optical fibre sensing techniques is also under consideration. Strain Optical Fibre Sensors (OFS) would be embedded in the carbon fibre supporting structures or/and sensor modules. The OFS would provide real-time strain information during the production, assembly, operation and push-pull operation of the instrumented tracker structures. From a detector integration point of view, using this kind of distributed monitoring requires only the embedding of 120 μm diameter optical fibres in the carbon fibre composite; this means that it can be also considered as a suitable technology for the vertex detector.

3.5.1 Alignment Methods

The FSI system incorporates multiple interferometers fed by optical fibres from the same laser sources, where the laser frequency is scanned and fringes counted, to obtain a set of absolute lengths. This alignment method was pioneered by the Oxford group on the ATLAS Experiment. By defining $\mathcal{O}(100)$ "lines of sight" in the tracker system for absolute distance measurements, we will over-constrain the locations of fiducial points in space,

allowing global distortions of the carbon-fibre support structure layers (translation, rotation, twist, bending, stretching, etc.) to be determined to the required precision. The real-time FSI measurements should allow for relevant time-dependent corrections to be applied when carrying out the final step of track-based alignment of individual silicon modules.

With a test apparatus, the state of the art in precision DC distance measurements over distance scales of a meter under laboratory-controlled conditions has been reached and extended. Precisions better than 100 nm have been attained using a single tunable laser when environmental conditions are carefully controlled. Precisions under uncontrolled conditions (e.g., air currents, temperature fluctuations) were, however, an order of magnitude worse with the single laser measurements.

Hence a dual-laser FSI system is foreseen for the tracker, one that employs optical choppers to alternate the beams introduced to the interferometer by the optical fibres. By using lasers that scan over the same wavelength range but in opposite directions during the same short time interval, major systematic uncertainties can be eliminated. Bench tests have achieved a precision of 200 nm under highly unfavourable conditions using the dual-laser scanning technique.

A separate real-time alignment method with different systematic uncertainties will be provided by a "laser-track" system in which selected sensor modules are penetrated by laser beams to mimic infinite-momentum tracks. This method exploits the fact that silicon sensors have a weak absorption of infrared (IR) light. Consecutive layers of silicon sensors are traversed by IR laser beams. The same sophisticated alignment algorithms as employed for track alignment with real particles can then be applied with arbitrarily high statistics to achieve relative alignment between modules to better than a few microns. This method employs the tracking sensors themselves, with only a minor modification to make them highly transparent to infrared light. A window in the aluminium metallisation on the back of the sensor with a diameter of few millimetres allows the IR beam to pass through. Since IR light produces a measurable signal in the silicon bulk, there is no need for any extra readout electronics. This alignment method has been implemented by both the AMS and CMS Experiments.

The sensing element of the OFS monitor is a Fibre Bragg Gratting (FBG) sensor operated as an optical strain gauge. FBG sensors have many enhanced features with respect to traditional electrical strain gauges: no need for power or readout cabling, long term stability, immunity to electromagnetic fields, high voltage, extreme temperature and radiation resistance. Concerning its application in tracker systems, one of the most important properties is its light weight since the actual FBG is "written" in a short section, only a few mm in length, of an optical fibre with a 125 μm diameter. Multiplexing capabilities having many distributed FBG sensors on the same optical fibre are available; this technology also allows for long-range sensing, placing the readout unit well outside of the detector. The

FBG sensor would be embedded in the carbon fibre structures supporting the modules and the module mechanics itself. The system is expected to reach local deformation sensitivities better than 1 μm strain. The OFS monitor will provide a very fast feedback on full structure deformations during the push-pull operations.

The final alignment of individual sensor modules will be track-based, using accumulated statistics from many detected tracks and constrained fitting to determine local position and orientation corrections for that module. The time to accumulate sufficient statistics for alignment of each individual module is expected, however, to be long enough to require continuous monitoring of global structure motions and deformations via the FSI and laser-track systems and to warrant robust, stable mechanical structures, as discussed above. Although six parameters are needed, in principle, to describe a rigid module's position and orientation, the most critical parameter for microstrip planes is the offset of the module from nominal along the direction normal to the microstrips and in the module plane, since this is the coordinate measured most precisely by the strips. Expected translations in the orthogonal directions should have a negligible effect on tracking. Rotations of module planes about their normals and about an axis parallel to the strips can lead to small biases in coordinate reconstruction, while rotation about an axis in the module plane and perpendicular to the strips should have negligible effects. To determine systematic offsets in the measured coordinate to a precision that is an order of magnitude smaller than the hit resolution requires O(100) tracks per module, assuming systematic variations in hit reconstruction for different strips in the same module are negligible. The sensor modules receiving the least number of tracks, i.e. $\cos(\theta) = 0$, outer barrel layer, are expected to be penetrated by O(10^4) tracks per month, making track-based alignment feasible for each separate data-taking epoch between push-pull moves. The fact that a large number of tracks produced will be back-to-back in the x-y plane with approximately equal p_{T} values should enable more powerful constrained-fit determination of module offsets.

3.5.2 Push-Pull Considerations

Six rigid-body degrees of freedom are anticipated for outer tracker alignment after a move of the detector: two transverse positions per end, an azimuth, and a z-position. Measurement data will be collected to monitor additional degrees of freedom corresponding to shape distortions which are expected to be quite small (twist, bending and stretching). The data will also be used to monitor long- and short-term instabilities of the rigid-body degrees of freedom. Twelve degrees of freedom are anticipated for vertex detector alignment after a move: two transverse positions per barrel end, two transverse positions per support cylinder end, one azimuth per support cylinder end, and one z-position per support cylinder end. An additional four degrees of freedom (two transverse positions of the beam pipe near each

LumiCal) will be considered in estimates of support structure distortions.

During detector moves; alignment of the beam pipe, the ends of the outer tracker, and beam monitoring calorimetry will be monitored nearly continuously relative to the central calorimeter via frequency scanned interferometry. At the end of motion; alignment of the beam pipe, beam monitoring calorimetry, and final quads will be adjusted relative to the outer tracker and central calorimeter. The vertex detector is mounted from the beam pipe and follows its motion. No adjustments to the position of the outer tracker are anticipated. Tune-up of beam position will be performed at low intensity while monitoring vertex detector and outer tracker backgrounds. The time required depends upon accelerator procedures.

During each move the FSI system will be operational and taking data continuously. At least six types of measurements are anticipated. The transverse and longitudinal positions of the ends of each outer tracker barrel layer at approximately eight azimuths will be measured. Also the transverse positions of each barrel layer for at least eight azimuths and additional z-locations along the layer will be determined as will be the overall length of each barrel layer for at least eight azimuths. The transverse and longitudinal positions of each disk near its outer periphery for at at least eight azimuths will be evaluated as well as the beam pipe transverse positions just inboard of each LumiCal location. Furthermore, the transverse and longitudinal positions of each vertex detector support cylinder at each end at approximately four azimuths will be assessed. Alarms will be set for any motion measured outside of what is expected. Consequently, electrical power will need to be maintained continuously for the laser system, and the optical bench will need to move with the detector. In addition, we envision measuring the strain of the structure during the move through the OFS method. Again, alarms would be set for measured values outside the expected range. Laser-track monitoring is also planned for a subset of the sensor modules. The OFS deformation monitoring system can be also operated continuously.

In summary, with the methodology described above, we expect to achieve a precision of 3 μm or better on outer tracker transverse coordinate offsets (barrels and disks) for an assumed hit precision of 7 μm before and after a detector move. For the vertex detector, which is more demanding given an expected single hit resolution for two coordinates of better than 3 μm, a relative alignment precision of 1 μm for coordinates transverse to the track is the goal.

Chapter 4

Calorimetry

4.1 Introduction

The SiD baseline design uses a Particle Flow Algorithm (PFA) approach to Calorimetry. PFAs have been successfully applied to existing detectors, such as CDF, ZEUS, and CMS and have resulted in significant improvements of the jet energy resolution compared to methods based on calorimetric measurement alone. However, these detectors were not originally designed with the application of PFAs in mind. The SiD baseline design on the other hand considers a PFA approach necessary to reach the goal of obtaining a measurement uncertainty on the jet energy resolution of the order of 3% or better for jet energies above 100 GeV. SiD is therefore optimised assuming the PFA approach and the major challenge imposed on the calorimeter by the application of PFAs is the association of energy deposits with either charged or neutral particles impinging on the calorimeter. This results in several requirements on the calorimeter design:

- To minimise the lateral shower size of electromagnetic clusters the Molière radius of the ECAL must be minimised. This promotes efficient separation of electrons and charged hadron tracks.

- Both ECAL and HCAL must have imaging capabilities which allow assignment of energy cluster deposits to charged or neutral particles. This implies that the readout of both calorimeters needs to be finely segmented transversely and longitudinally.

- The calorimeters need to be inside the solenoid to be able to do track to cluster association; otherwise, energy deposited in the coil is lost and associating energy deposits in the calorimeter with incident tracks becomes problematic.

- The gap between the tracker and the ECAL should be minimised.
- The calorimeter needs to be extendable to small angles to ensure hermeticity, and be deep enough to contain hadronic showers.

Following is a description of the baseline designs and options for the ECAL and the HCAL. Also included are brief descriptions of alternative calorimeter technologies being considered by SiD.

4.2 Electromagnetic Calorimeter

4.2.1 Introduction

The major challenge imposed on the calorimeter by the application of PFAs is the association of individual particles with their energy depositions in the calorimeters. For the ECAL, this implies that electromagnetic showers be confined to small volumes in order to avoid overlaps. Effective shower pattern recognition is possible if the segmentation of readout elements is small compared to the showers. This level of transverse segmentation then also facilitates the separability of the electromagnetic showers from charged particle tracks due to un-interacted charged hadrons (and muons). The longitudinal segmentation is chosen not only to achieve the required electromagnetic energy resolution, but also to provide discrimination between electromagnetic showers and those hadrons which interact (typically deeper) in the ≈ 1 interaction length of the ECAL. Finally, there should be a sufficient number of longitudinal readout layers to provide charged particle tracking in the ECAL. This is important not only for the PFA algorithms, but also to aid the tracking detectors, especially for tracks which do not originate from the IP.

The ECAL described in this section according to the qualitative description above is expected to have capabilites including:

- Measurement of beam-energy electrons and positrons (and photons) from (radiative) Bhabha scattering. This is sensitive to contact terms and the angular distribution provides important information on electroweak couplings, for example in interference terms between Z, γ, and a new Z$'$. Precise Bhabha acollinearity distributions provides a key piece of the measurement of the luminosity spectrum [35], which is crucial for correct measurement of sharp threshold features in the annihilation cross section.
- electrons from $Q \to Q' e \nu$ (where Q = heavy quark).
- adequate electromagnetic energy resolution; the anticipated $\sim 0.17/\sqrt{E} \oplus 1\%$ is sufficient for this component in the PFA.

The imaging ECAL can also provide these more challenging measurements abilities compared to previous ECALs. These have already been demonstrated in simulation and in the PFA-based reconstruction:

- PFA reconstruction of photons in jets with high (95%) efficiency
- PFA tracking of charged particles in jets
- ECAL-assisted tracking (especially for decays of long-lived particles)
- π^0 reconstruction in τ decays. This is a crucial for identification of τ final states which are important for measuring τ polarisation, P_τ.

Some other possibilities have not yet been fully demonstrated in simulation, but are under study and will be further studied:

- π^0 reconstruction in jets - this allows improvement of the EM component of jet energy [36]
- photon vertexing - the impact parameter resolution for photons of ~ 1 cm would be important for identifying decays where photons are the only visible decay products, such as predicted from some gauge-mediated SUSY-breaking models

In the following, we provide a description of the baseline ECAL. We then discuss the R&D program, including recent progress.

4.2.2 Global ECAL Design

A sampling ECAL provides adequate energy resolution for the ILC physics, as discussed above. Because of its small radiation length and Molière radius, as well as its mechanical suitability, we have chosen tungsten absorber/radiator. Due to practical considerations for ease of production of large plates and machining, the tungsten will be a (non-magnetic) alloy. This currently chosen alloy includes 93% W with radiation length 3.9 mm and Molière radius 9.7 mm. An additional benefit of tungsten is that it has a relatively large interaction length, which helps to ameliorate confusion between electromagnetic and hadron showers in the ECAL.

The longitudinal structure we have chosen has 30 total layers. The first 20 layers each have 2.50 mm tungsten thickness and 1.25 mm readout gap. The last 10 layers each have 5.00 mm tungsten plus the same 1.25 mm readout gap. This configuration is a compromise between cost, shower radius, sampling frequency, and shower containment. The cost is roughly proportional to the silicon area, hence the total number of layers. We chose finer

sampling for the first half of the total depth, where it has the most influence on electromagnetic resolution for showers of typical energy. However, as discussed below, an increase in sampling with fixed readout gaps has a detrimental effect on the shower radius. The total depth is 26 X_0, providing reasonable containment for high energy showers. Simulations in EGS4 and GEANT4 have shown the energy resolution $\Delta E/E$ for electrons or photons to be well described by $0.17/\sqrt{\mathrm{E}} \oplus 1\%$.

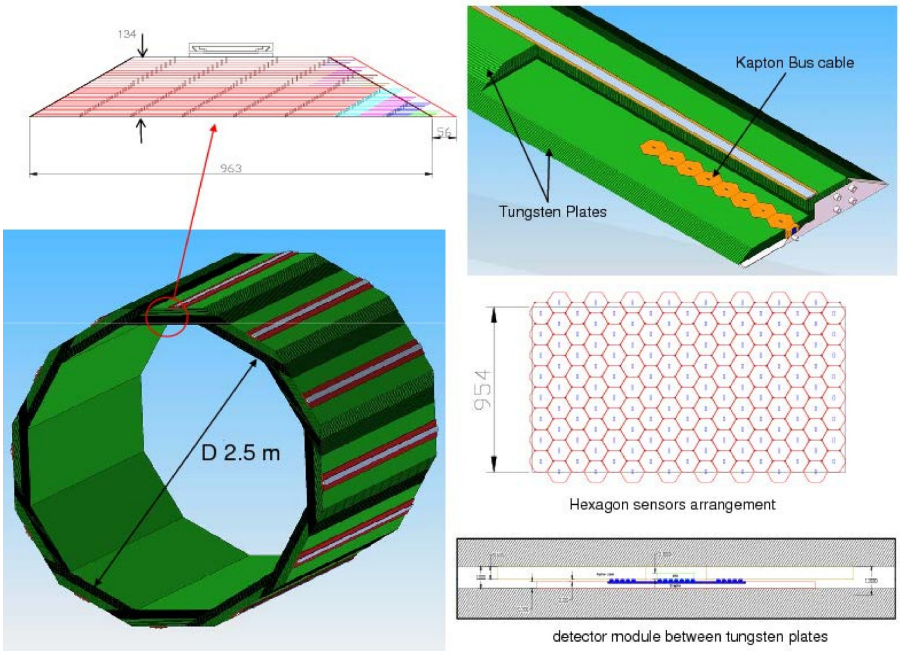

Figure 4.2.1: Overall mechanical layout of the ECAL.

Silicon detectors are readily segmented. In the baseline design we have chosen (see description below), there is little penalty for segmenting the silicon sensors much more finely than typical shower radii. (The MAPS option takes this to the extreme.) As discussed above, the scale for this is set by the shower size, which we wish to be as small as feasible. A useful figure of merit for this is the Molière radius, which is 9 mm for pure tungsten. Since showers will spread in the material between tungsten layers, it is crucial to keep the readout gaps as small as possible. We can scale the shower radii by a simple factor to provide a figure of merit. In our case, this factor is $(2.50 + 1.25)/2.50 = 1.50$ for the crucial first

20 layers. We can then define the effective Molière radius, $\mathscr{R}$, as the Molière radius of the radiator multiplied by this factor. In our case, this is about 14 mm. A crucial driving force in our design has been to provide as small a $\mathscr{R}$ as feasible, along with a transverse segmentation of the readout which is well below $\mathscr{R}$.

Table 4.2.1 summarises the basic ECAL parameters. Figure 4.2.1 shows the overall mechanical structure of the ECAL barrel, including detectors layout (for the baseline option) and readout gap.

Table 4.2.1: Nominal parameters of the silicon-tungsten ECAL for SiD.

inner radius of ECAL barrel	1.27 m
maximum z of barrel	1.76 m
longitudinal profile	20 layers $\times$ 0.64 X_0
	10 layers $\times$ 1.30 X_0
EM energy resolution	$0.17/\sqrt{E} \oplus 1\%$
readout gap	1.25 mm (or less)
effective Molière radius ($\mathscr{R}$)	14 mm

Referring to Figure 4.2.1, the construction of a barrel "wedge" module is carried out as follows. Because tungsten plates are only available with a maximum size of 1×1 m^2, the wedge assembly is done by interconnecting the plates with a screw-and-insert network, which transfers the load from the bottom of the stack to the rail. The design is self-supporting and it does not require additional material to provide the required stiffness. The assembly procedure for a single wedge is sequential with the sensors permanently captured in the gap between tungsten plates, which are specified to have high planarity, achieved at the vendor site by grinding. This specification has been verified on a batch of 15×15 cm^2 plates procured for the beam test module (see Section 4.2.3), which have planarity tolerances of ± 10 μm, and have been confirmed by interviewing several tungsten vendors/producers. Because of the trapezoidal cross-section of the wedge, the assembly sequence is bottom up, with the wider plate at the base. The first layer of tungsten will be laid down on a jig tool to set the basic tolerances of the stack. Spacing inserts are placed at the locations of the cutouts at the sensor edges (see Figure 4.2.2), followed by the sensors with flex cables.

The control of the gap tolerances relies on the flatness of the tungsten plate and on the spacers, which are individually quality-checked by metrology. The positioning tolerances of the sensor modules in the plane rely on the QC of spacer too, but also on the flex-cable, which will have mounting pads which mate with the inserts. The assembly of the sensors on the flex-cable will be done on a precision jig, which will guarantee the repeatability of

the assigned tolerances. The second layer of tungsten will be overlaid on the sensors, once mechanical and electrical connection are tested. This process is repeated 30 times along the stack, which is the number of the active layers of a single wedge module. The last plate on the top has rails, which will allow the insertion and the support from the HCAL. Prior to insertion, each individual wedge will be equipped with a cold plate for thermal management, running along z on one side of the wedge. The boxes on the two opposite sides at $\pm z$ contain the data concentrator electronics, which completes the assembly

4.2.3 Baseline Technology

In the baseline design, the ECAL readout layers are tiled by large, commercially feasible silicon sensors (presently from 15 cm wafers). The sensors are segmented into hexagonal pixels which are individually read out over the full range of charge depositions. The complete electronics for the pixels is contained in a single chip (the KPiX ASIC) which is bump bonded to the wafer. We take advantage of the low beam-crossing duty cycle (10^{-3}) to reduce the heat load using power pulsing, thus allowing passive thermal management within the ECAL modules. The realisation of this technology has been the subject of an intensive, ongoing R&D program.

The main parameters associated with the baseline technology choice are given in Table 4.2.2. Some details of the design and R&D results are given below. Further details can be found in the references [37, 38].

Table 4.2.2: Parameters of baseline silicon-tungsten ECAL and the MAPS option.

	Baseline	MAPS option
pixel size	13 mm^2	50$\times$ 50 µm
readout gap	1.25 mm	similar
	(incl. 0.32 mm thick Si sensors)	
effective Molière radius	14 mm	14 mm
pixels per silicon sensor	1024	$1 \cdot 10^6$
channels per KPiX chip	1024	-
dynamic range	$\sim$ 0.1 to 2500 MIPs	1 MIP
heat load	20 mW per sensor	20 mW per sensor

Figure 4.2.2 shows a sensor with 1024 pixels. Not shown in the drawing are the signal traces, part of the second layer metallisation of the sensors, which connect the pixels to a bump-bonding pad at the centre of the sensor for input to the KPiX readout chip. The

pixels are DC-coupled to the KPiX, thus only two metallisation layers are required for the sensors. The pixels near the bump-bonding array at the centre are split to reduce capacitance from the large number of signal traces near the sensor centre. The electronic noise due to the resistance and capacitance of the traces has been minimised within the allowed trace parameters. The cutouts at the corners of the sensor are to accommodate mechanical stand-offs which support the gaps between the tungsten layers.

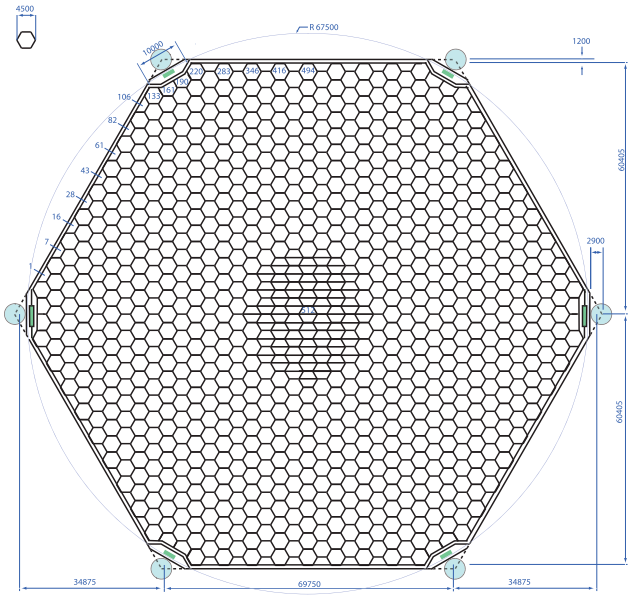

Figure 4.2.2: Drawing of a silicon sensor for the ECAL. The sensors are segmented into 1024 13 mm^2 pixels.

The lower-right image of Figure 4.2.1 depicts a cross-sectional view of the readout gap in the vicinity of the centre of the sensor. The silicon sensor is about 320 µm thick. The KPiX is bump-bonded to the silicon sensor at an array of bump pads which are part of the second metallisation layer from sensor fabrication. This is a 32 $\times$ 32 array of bump bond pads. Polyimide (Kapton) flex cables connect near the centre of the sensors. The cables bring power and control signals into the KPiX chip and bring out the single digital output line for the 1024 channels.

Thermal management is a crucial feature of this design. Our requirement is to hold the average power dissipation per wafer to less than 40 mW. This will allow the heat to be extracted purely passively, providing a highly compact and simple design, less subject

to destructive failures. The ILC bunch structure allows for power pulsing. A factor 80-100 reduction in power consumption is obtained by switching off the most power hungry elements of the KPiX chip, e.g. the analog front end, for most of the interval between the bunch trains. The design of the KPiX chip yields an average power below 20 mW when power pulsing is applied. While we do not foresee the need for cosmic ray data, the power pulsing eliminates this possibility.

After several interactions with the R&D, in early 2012 a full 1024-channel KPiX was successfully bump-bonded to a sensor by IZM Company. Following this, a Kapton cable was successfully bump-bonded to the sensor assembly at UC Davis. The cable bonding uses a lower temperature solder than that used for the KPiX bonding. Figure 4.2.3 shows the fully bonded assembly.

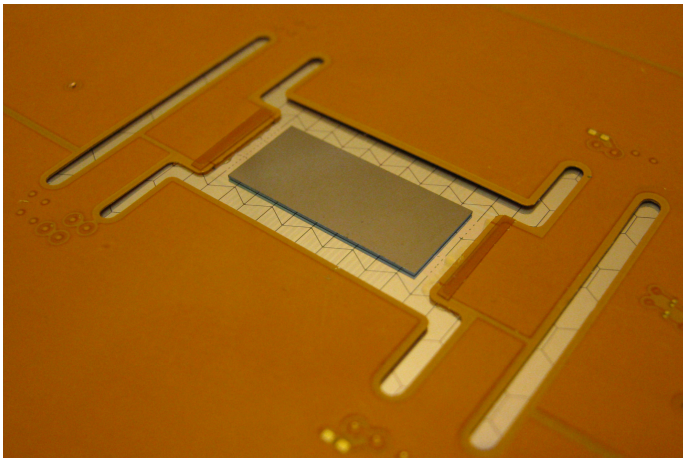

Figure 4.2.3: Photograph of the central region of a sensor. The KPiX chip is bump-bonded to the sensor and is visible through the central cutout of the Kapton cable. The slots in the Kapton allow for differential thermal expansion.

Bonded sensor results

Initial bench tests of the bonded sensor of Figure 4.2.3 have been carried out and the results are quite promising. A cosmic ray telescope was used to trigger KPiX and the charge of the pixel having the maximum charge was entered in the distributions shown in Figure 4.2.4. The red distribution resulted when the ECAL sensor was placed within the telescope acceptance, while the blue distribution resulted when the sensor was outside the telescope

acceptance. A Landau distribution (black) is fit to the red signal. The peak of the signal at about 4 fC is consistent with our expectation for MIPs passing through the fully-depleted 320 µm thick sensors.

With the highly integrated design we have chosen, a potential worry is crosstalk between channels. Figure 4.2.4 indicates no evidence for crosstalk in any other channel when a large 500 fC signal is injected. The noise distribution is nicely fit by a Gaussian with RMS 0.2 fC. This is to be compared with the 4 fC MIP signal. This noise level exceeds our requirements for the ECAL.

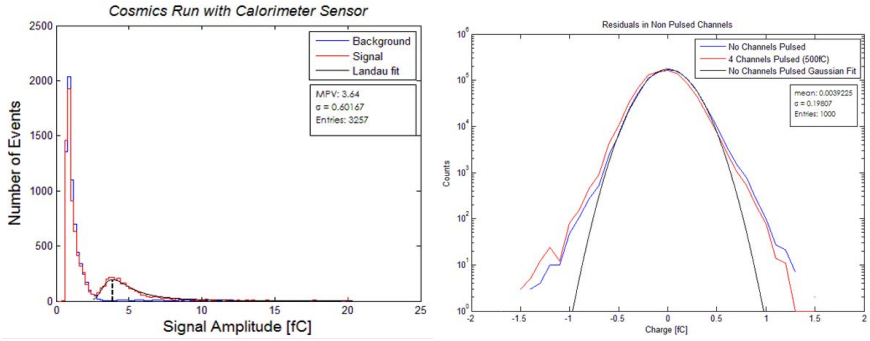

Figure 4.2.4: Distribution of charge depositions in bonded sensor for cosmic ray triggered events (left). The MIP peak is clearly visible above the noise peak. Crosstalk test of bonded sensor (right). The charge distributions for all non-pulsed pixels are compared for a large pulse injection (red) and no pulse injection (blue). Also shown is a Gaussian fit with RMS 0.2 fC.

Prototype Module and Test Beam

Given the positive initial results of the first bonded sensors, we are moving forward with our plans to build a full-depth test module. This is shown in Figure 4.2.5. The test stack is to have a width of one sensor, easily sufficient to contain electromagnetic showers. The longitudinal structure closely matches that of the SiD ECAL. The main difference is that we will have 1.5 mm readout gaps for the test stack, rather than the nominal 1.25 mm gaps of the SiD design, in order to allow clearance for sensor assemblies to be slid in or out of the stack.

Since the operation of KPiX has been optimised for the bunch timing structure of the ILC, the optimal test facility would be a linear collider having a similar timing structure.

Fortunately, SLAC is presently restoring a test beam capability at End Station A. We expect to have the sensors for the test module prepared and first data from this facility in 2013.

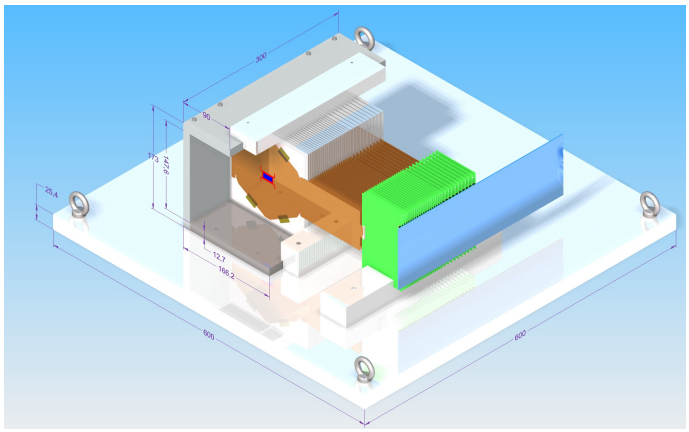

Figure 4.2.5: Schematic of test module to be tested in a beam. The module has a width of one sensor and a depth of 30 layers. The Kapton cables attached to each sensor feed concentrator boards, which in turn are connected to a mother board.

4.2.4 MAPS option

The Monolithic Active Pixel Sensor option [39] uses 50 ×50 µm silicon pixels as readout material. The main difference here is the usage of digital electromagnetic calorimetry where the ECAL is operated as a shower particle counter. The simulated performance [40] is illustrated in Figure 4.2.6 where the potentially advantages are clearly visible. These sensors could be manufactured in a commercial mixed-mode CMOS process using standard 300 mm wafers. This is an industrial and widely available process, so pricing for these wafers should be very competitive. We have also incorporated the usage of deep p-well implants and high resistivity epitaxial layers in this design, which was used to be rather non-standard for CMOS processes previously. This allows to include full CMOS functionality in a MAPS pixel, which has been possible before.

Three first-generation sensors for digital electromagnetic calorimetry, TPAC 1.0, 1.1 and 1.2 [40, 42] have been manufactured and tested. They consists of 168×168 pixels with the required size of 50×50 µm. The TPAC 1.2 will be described in more detail. It uses a the pre-Shaper architecture and consists of a charge preamplifier, a CR-RC shaper which generates a shaped signal pulse proportional to the amount of charge collected and

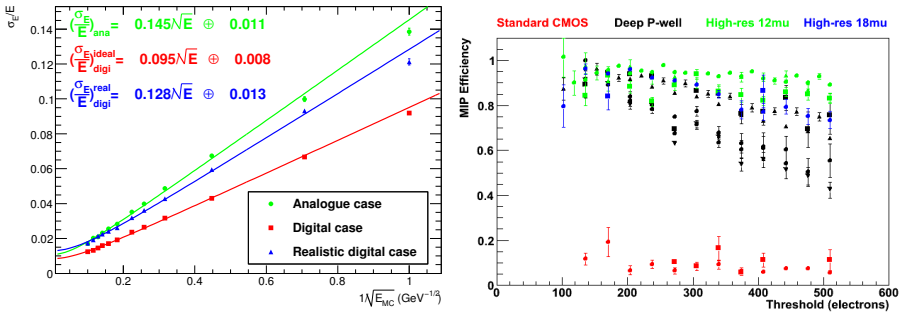

Figure 4.2.6: Left: The energy resolution as a function of the incident energy for single electrons for both analog and digital readout using a GEANT4 simulation. The realistic digital cases includes effects of saturation and charge sharing, leading to a degradation of 35% [40]. Right: The MIP detection efficiency as a function of the comparator threshold for different process variants of TPAC 1.2 [41, 42]; no deep p-well implant (standard CMOS), deep p-well implant and high-resistivity epitaxial layer (all 12 µm) and 18 µm high-resistivity layer

a two-stage comparator which triggers the hit-flag. The sensor supports single-bunch time stamping with up to 13 bits. Each pixel has a 6 bit trim to compensate for pedestal variations and each pixel can be masked off individually. A bank of forty-two pixels shares nineteen memory buffers to store the hits during the bunch train. The sensor also supports power-pulsing already and is able to power off its front-end in the quiet time between bunch trains.

All sensors have been tested using sources and lasers [39, 40, 41, 42]. The TPAC 1.2 sensor was tested in test beams at CERN and DESY using a stack of six TPAC sensors. The minimum ionising particle efficiency was found by using the outer four TPAC planes to perform the track finding and then deriving the MIP detection efficiency of the two inner planes [41, 42]. This was done for a range of threshold values (see Figure 4.2.6). The version without a deep p-well (using plain CMOS) shows a very low MIP efficiency. Including the deep p-well then increases the detection efficiency to around 80-85%. The addition of the high-resistivity epitaxial layer then makes TPAC close to a 100% efficient for minimum ionising particles.

The MAPS option is designed to fit in the same mechanical structure as the baseline option and we foresee a sensor size of 5 $\times$ 5 cm (baseline) for a final system. As the active sensor area is less than 20 µm thick, it does allow back-thinning of the wafers down to 100 µm or less. The main parameters for the MAPS option are summarised in Table 4.2.2.

4.2.5 Calibration and alignment

Silicon detectors are inherently insensitive to gain variations with time and should not have significant inter-pixel gain differences. Pixel to pixel gain differences in the electronic readout are calibrated by dedicated calibration circuitry within the KPiX chip. Perhaps the main calibration issue will be sensor to sensor gain differences. These are not expected to be large, but we are investigating different options for this calibration.

Alignment within ECAL modules and between modules should not be difficult to control with careful fabrication. Alignment to the inner detectors can be sufficiently established using charged particle tracks.

4.3 Hadronic Calorimeter

4.3.1 HCAL requirements

Within the PFA paradigm the role of the hadron calorimeter is to allow identification of the energy deposits from charged particles, and to measure the energy associated with neutral hadronic particles, such as neutrons and $K_L^0 s$. In this approach the challenge is to unambiguously identify energy deposits in the calorimeter as belonging to charged particles (and therefore to be ignored) or to neutral particles (and therefore to be measured). As a consequence, the optimal application of PFAs requires calorimeters with the finest possible segmentation of the readout. Further requirements imposed by the application of PFAs on the hadron calorimeter include:

- Operation in a (strong) magnetic field;
- Limitations on the thickness of the active element (to keep the coil radius as small as possible);
- Manageable accidental noise rate (to keep the confusion term manageable).

In general, the active elements need to satisfy standard performance criteria, such as reliability, stability, a certain rate capability and be affordable.

4.3.2 Description of the DHCAL concept

The PFA-based HCAL is a sandwich of absorber plates and instrumented gaps with active detector elements. The active detector element has very finely segmented readout pads, with 1×1 cm^2 size, for the entire HCAL volume. Each readout pad is read out individually, so the readout channel density is approximately $4\times10^5/\mathrm{m}^3$. For the entire SiD HCAL,

with $10^2 m^3$ total volume, the total number of channels will be 4×10^7 which is one of the biggest challenges for the HCAL system. On the other hand, simulation suggests that, for a calorimeter with cell sizes as small as 1×1 cm^2, a simple hit counting is already a good energy measurement for hadrons. As a result, the readout of each channel can be greatly simplified and just record 'hit' or 'no hit' according to a single threshold (equivalent to a '1-bit' ADC). A hadron calorimeter with such kind of simplified readout is called a Digital Hadron Calorimeter (DHCAL). In a DHCAL, each readout channel is used to register a 'hit', instead of measure energy deposition, as in traditional HCAL. In this context, gas detectors (such as RPC, GEM and Micromegas) become excellent candidates for the active element of a DHCAL.

The SiD baseline design uses a DHCAL with RPC as the active element.

4.3.3 Global HCAL mechanical design

The SiD HCAL is located inside the magnet and surrounds the electromagnetic calorimeter, the latter being fixed to it. The HCAL internal and external radii are respectively: R_{int}=1417 mm and R_{ext}=2493 mm. The overall length is 6036 mm, centred on the interaction point.

The HCAL is divided into twelve identical azimuthal modules, as illustrated in Figure 4.3.1. Each module has a trapezoidal shape and covers the whole longitudinal length. The chambers are inserted in the calorimeter along the Z-direction from both ends and can eventually be removed without taking out the absorber structure from the magnet. Special care of the detector layout has been taken into account to avoid a crack at θ=90°.

The absorber plates are supported by several stringers fixed radially on both sides of the modules. Stringers of two consecutive modules are staggered in order to maximise the active detector area. Although the space between two consecutive modules is not instrumented, it is however filled by the absorber material. The barrel will be fixed on the magnet at 3 and 9 o'clock or 5 and 7 o'clock.

Each endcap forms a plug that is inserted into an end of the barrel calorimeter. The layer structure of the end cap calorimeters is the same as for the barrel. Figure 4.3.1 shows a view of one endcap.

4.3.4 Baseline technology

In the baseline design, the active element of the SiD DHCAL uses Resistive Plate Chambers (RPCs).

RPC fulfils all the above mentioned requirements for a PFA DHCAL. For the standard two-glass plate design [43], a position resolution of a few hundred μm is typical and so a

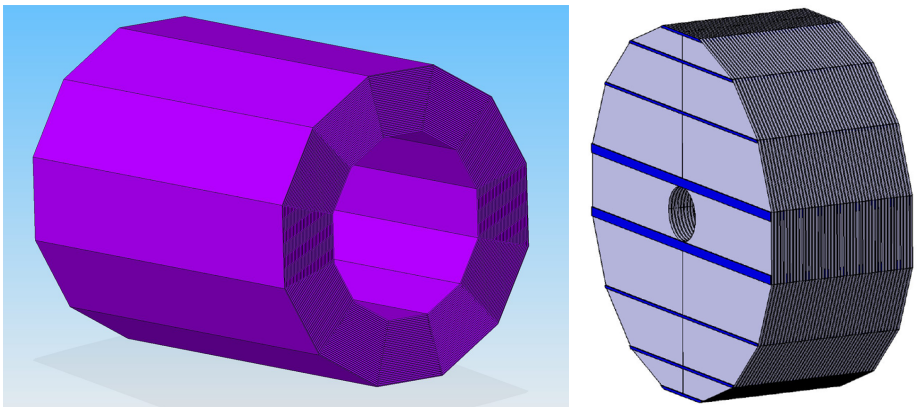

Figure 4.3.1: Cross-section of the HCAL barrel (left) and face and top views of the HCAL endcap (right).

segmentation of the readout into pads of 1×1 cm^2 or smaller is technically meaningful. The design can be tuned to minimise the thickness. With two glass plates a layer thickness smaller than 8 mm appears achievable. If using the 1-glass design [43] an overall thickness of 1 mm less is conceivable. The noise rate for RPCs is in general extremely low, with values below 1 Hz/cm^2 for MIP detection efficiencies exceeding 90% [44].

RPCs with glass plates as resistive plates are reliable and operate stably. Long term tests showed no changes in performance [44]. The rate capability of RPCs is well understood [45] and is adequate for most of the solid angle of a colliding beam detector. In the forward region, where the rates are in general higher, RPCs using resistive plates with lower bulk resistivity or other high rate gas detectors might be required.

RPC chamber designs

Resistive Plate Chambers (RPCs) are gaseous detectors primarily in use for the large muon systems of colliding beam detectors. The detectors feature a gas volume defined by two resistive plates, typically Bakelite or glass. The outer surface of the plates is coated with a layer of resistive paint to which a high voltage is applied. Depending on the high voltage setting of the chamber, charged particles crossing the gas gap initiate a streamer or an avalanche. These in turn induce signals on the readout strips or pads located on the outside of the plates.

Various chamber designs have been investigated [43] for the SiD DHCAL. Of these two are considered particularly promising: a two-glass and an one-glass plate design. Schemat-

ics of the two chamber designs are shown in Figure 4.3.2. The thickness of the glass plates is 1.1 mm and the gas gap is maintained with fishing lines with a diameter of 1.2 mm. The overall thickness of the chambers, including layers of Mylar for high voltage protection but excluding readout board, is approximately 3.7 mm and 2.6 mm, respectively. The two-glass design is the current baseline, however, due to its attractive features, the one-glass design is being actively developed.

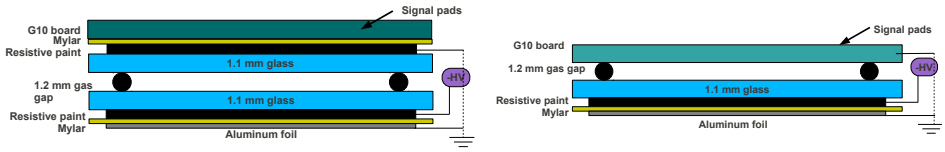

Figure 4.3.2: Schematic of the RPC design with two glass plates (left) and one glass plate (right). Not to scale.

Readout

The electronic readout system needs to be optimised for the readout of tens of millions of readout channels envisaged for the SiD hadron calorimeter operating at the future International Linear collider. Due to the high channel count, a front end ASIC and several layers of data concentration are considered necessary. In the R&D phase, a readout system was developed and constructed for the DHCAL prototype which handles nearly 500,000 readout channels. Even though the system was optimised for test beam operation and did not address all requirements for a realistic SiD DHCAL system, it achieved the very first embedded front-end readout for a calorimeter system and serves as a milestone towards the final engineering design.

A block diagram of the prototype DHCAL readout system is shown in Figure 4.3.3. The electronics is divided into two parts: The "on-detector" electronics processes charge signals from the detector, collects data for transmission out, and acts as the interface for slow controls. The "back-end" electronics receives and processes the streams of data from the front-end electronics, and in turn passes it to the Data Acquisition (DAQ) system. It also has an interface to the timing and trigger systems.

A custom integrated circuit (ASIC) has been developed for the front-end. The ASIC chip, called DCAL performs, in addition to ancillary control functions, all of the front-end processing, including signal amplification, discrimination/comparison against threshold, recording the time of the hit, temporary storage of data, and data read out. It services

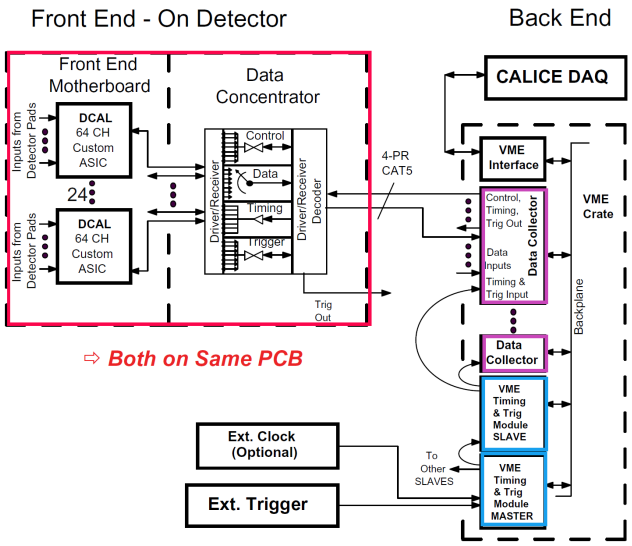

Figure 4.3.3: Block diagram of the readout system of the DHCAL prototype.

64 detector channels with a choice of two programmable gain ranges ($\sim$10 fC and $\sim$100 fC sensitivity.)

The chips reside on front-end printed circuit boards that are embedded in the DHCAL active layer. There are 24 chips on a front-end board, servicing 1,536 channels. An FPGA based data concentrator (DCON) resides on the edge of the front-end board which collects data from the 24 DCAL chips and serves as the first level of data concentration. The DCON's send their data to the data collectors (DCOL's) through serial links. The DCOL's are located in VME crates and serves as the second level of data concentration. Each DCOL receives data from 12 DCON's and store the data into a large buffer for DAQ program to read via VME bus.

The system runs in two modes: triggered mode and triggerless (or self-triggered) mode. The first was designed for test beam runs with an external trigger. The second mode was designed for noise measurement, but was also found to be extremely useful in monitoring the RPC condition, collecting cosmic ray data for calibration and capturing all particles in a spill at a test beam.

The readout system for the DHCAL prototype is proven to be very reliable and has extremely low error rate. The front-end has very low noise. For all practical purposes, the noise coming from the front-end electronics can be safely ignored. As previously mentioned, the readout system for the DHCAL prototype did not address all requirements for a

real DHCAL system in a colliding beam experiment. Further R&D is needed for the final readout design. There are two possibilities:

- Continue the development based on the success of the current DHCAL prototype readout system and focus on reducing power consumption, improving data transmission routing and optimising readout board thickness;
- Adopting KPiX readout for the DHCAL. The R&D needs to start from small scale chamber test and have several system level prototyping. This approach will be a longer development, however, it has the potential benefit of having a more uniform readout across the entire SiD detector;

Active layer design

In the baseline design, the barrel modules have a trapezoidal cross section. There are 40 layers in each module, each layer is 28 mm thick, consists of a 20 mm thick steel absorber and a 8 mm active layer for the RPC and its front-end readout. The innermost layer has a size of 740 mm $\times$ 6036 mm, and the outermost layer has a size of 1350 mm $\times$ 6036 mm.

Within each active layer, there are six RPCs that cover the entire area. Each RPC has a width 10 mm shorter than the full width of the layer. Along the beam direction, there are two different lengths for the RPCs: five at 966 mm and one at 1206 mm. With a 3 mm frame, the RPCs will have an active length of 960 mm or 1200 mm, which accommodates 96 or 120 readout pads of 1×1 cm^2 size. The six RPCs forms a row within a layer with the long RPC at the end. Neighbouring layers have the long RPC at alternating ends so that the dead areas between the RPCs are not lined up in all layers. The smallest RPC unit has a size of 730 mm $\times$ 966 mm, while the largest RPC has a size of 1340 mm $\times$ 1200 mm, which is still within comfortable range for RPC construction and handling.

The RPC sizes exceed the size of a reasonable PCB board, so each RPC will be read out by several boards that have 1×1 cm^2 pads on the RPC side and front-end components on the other side. The basic dimension of the readout board is 32×32 cm^2. The short RPC needs exactly three readout boards along its length, and the long RPC needs three standard boards and a 32×24 cm^2 board to fill the whole length. Several special boards, that are 32 cm or 24 cm long and have different widths, are needed to fill the entire width of the RPCs in different layers. Boards that are in the same row along beam direction are chained together using flex cables and are read out from both ends of the module.

The baseline design uses a two-glass RPC design, which has a thickness of 3.7 mm, including insulation material. The readout board has a total thickness of 3.8 mm, including the height of surface mount components. The total thickness of the active elements adds up

to 7.5 mm, which leaves 0.5 mm tolerance to slide the RPC and the readout boards in and out of the 8 mm gap between the absorbers.

The RPCs run with negative high voltage. The high voltage side of the RPC faces the inner absorber, and the readout is on the ground side of the RPC and is close to the outer absorber. The RPCs leave 5 mm space along both sides of the gap which allow two 1/8" gas tubes and one thin high voltage cable to run into the gap along each side. They supply gas and high voltage to the two inner RPCs on the same half of the module, and the end RPC is directly accessible from the end of the module.

The endcap modules have a similar active layer design, except that all RPC's have direct access form the end of the modules which make gas and high voltage connections significantly easier.

Results of prototype testing

The development of a hadron calorimeter based on the RPC technology progressed in several stages: a) Studies of various RPC designs, b) Construction and testing of a small scale calorimeter prototype, the Vertical Slice Test (VST), c) Construction of the DHCAL prototype, d) Testing of the DHCAL prototype in the Fermilab and CERN test beams. In the following we briefly report on the main results obtained in these stages.

RPC tests

We choose to operate the RPCs in a saturated avalanche mode with an typical high voltage setting around 6.3 kV. The working gas has three components: Freon R134A (94.5%), isobutane (5.0%) and sulfur-hexafluoride (0.5%).

The size of the signal charges, the MIP detection efficiency and the pad multiplicity (as function of operating conditions) were measured with both cosmic rays and beam muons. As an example, Figure 4.3.4 shows the pad multiplicity versus MIP detection efficiency [46]. Note the constant pad multiplicity at 1.1, independent of efficiency, for the one-glass design.

The RPCs in the Vertical Slice Test were also exposed to 120 GeV protons at various beam intensities to study their rate capability. The results show no loss of the MIP detection efficiency for rates below 100 Hz/cm^2. For higher rates, the efficiency drops exponentially in time (with a time constant depending on the beam intensity) until reaching a constant level.

The RPCs being tested have been operated continuously for over 18 months. Within the time period of these studies there was no evidence of long-term aging effects.

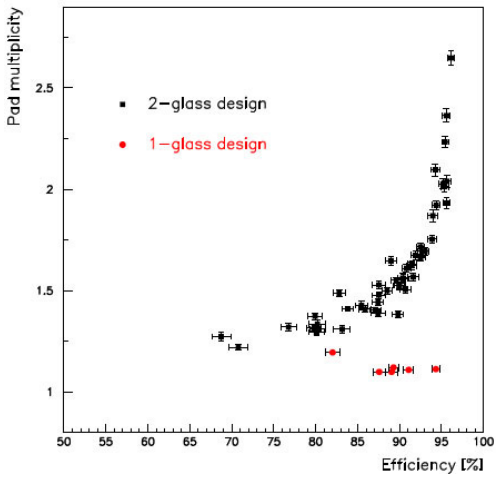

Figure 4.3.4: Pad multiplicity versus MIP detection efficiency for 2-glass RPC and 1-glass RPC, measured with muon beam.

DHCAL prototype and TCMT

The DHCAL prototype constitutes the first large scale hadron calorimeter with digital readout and embedded front-end electronics. It also utilised, for the first time, a pad-readout together with RPCs. The design of the DHCAL was based on preliminary work done with the Vertical Slice Test.

The DHCAL prototype consists of two parts: a 38-layer structure with 17.5 mm thick steel absorber plates and a 14-layer structure with eight 2.54 cm thick steel plates followed by six 10.0 cm thick steel plates. The former is commonly referred to as the DHCAL, or the Main Stack, and the latter is called the Tail Catcher and Muon Tracker (TCMT). These absorber structures were equipped with RPCs as active elements. Each layer measured approximately 1×1 m^2 and was inserted between neighbouring steel absorber plates. The Main Structure rested on a movable stage, which offered horizontal and vertical movements in addition to the possibility of rotating the entire stack. Figure 4.3.5 shows photographs of the Main Structure and the TCMT.

Each layer consists of three RPCs, each with an area of 32×96 cm^2 and stacked vertically on top of each other to create a 1×1 m^2 active area. Each RPC in turn is read out with two front-end boards, which covered the entire gas volume of the chambers. The three chambers and their boards are contained in a cassette structure providing the mechanical protection during transportation and installation.

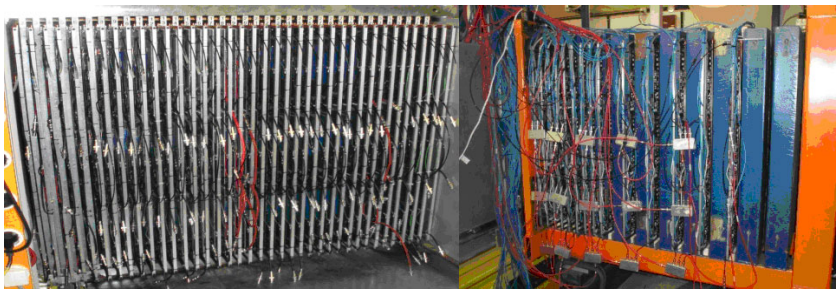

Figure 4.3.5: Left: the DHCAL main stack (before cabling), right: the TCMT.

The construction of the DHCAL prototype and TCMT started in fall 2008 and finished in early 2011.

DHCAL prototype test beam campaigns

The DHCAL was tested extensively in the Fermilab test beam in various configurations: with the Scintillator Tail Catcher, with the Tail catcher equipped with RPCs, with or without the CALICE Silicon-Tungsten ECAL in front, and also with minimal absorber material between layers. In total, 9.4M triggers were collected from muon beam and 14.4M triggers are collected from secondary beam. Figure 4.3.6 shows some events recorded by the DHCAL prototype and TCMT during the test beam campaigns.

In Spring 2012 the DHCAL layers were transported to CERN and were inserted into a Tungsten absorber structure with 39 layers and a Steel tail catcher with 15 layers. Tests at both the Proton-Synchrotron and the Super-Proton-Synchrotron have been carried out. So far, 5 million muon events and 22 million secondary beam events have been collected.

4.3.5 DHCAL prototype performance

The DHCAL is a novel type of calorimeter. To first order the energy E of an incident particle is reconstructed as being proportional to the number N of pads hits. However, a non-vanishing noise rate and variations in the chamber efficiencies and average pad multiplicities need to be corrected for, such that the energy of an incident particle is reconstructed as

$$E = \alpha_{sample} \times (\sum_{i=0}^{n} N_i \cdot \frac{\varepsilon_0}{\varepsilon_i} \cdot \frac{\mu_0}{\mu_i} - N_{noise}) \tag{4.3.1}$$

where the sum runs over all layers of the detector, α_{sample} is the sampling fraction which may depend on particle energy, ε_0 and μ_0 are the average MIP detection efficiency and the

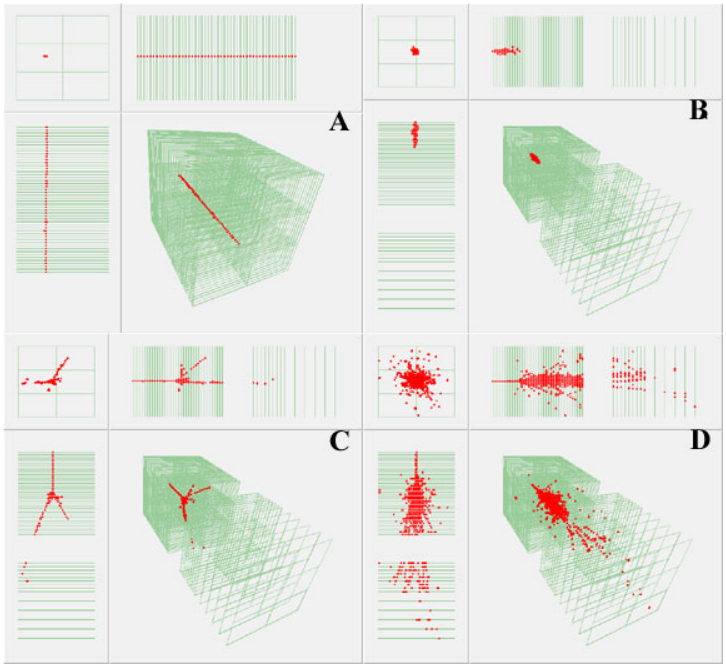

Figure 4.3.6: Events recorded by DHCAL prototype at the Fermilab test beam. A: a muon track; B: 8 GeV positron shower; C: 8 GeV pion shower; D: 120 GeV proton shower.

average pad multiplicity of the detector, ε_i and μ_i are the MIP detection efficiency and average pad multiplicity of layer i and N_{noise} is the average contribution from noise. All these calibration parameters are carefully measured and monitored over time during the test beam campaigns for the DHCAL prototype. The DHCAL response for positrons and pions are measured at different beam momenta, and data analysis is still on-going. We show preliminary results for the DHCAL noise measurement, muon calibration, positron response and pion response.

Noise measurement

The accidental noise rate was measured both with random triggers and with trigger-less acquisitions. Confirming our measurement with the Vertical Slice Test, the rate was found to be low, but to depend on the temperature of the stack and the ambient air pressure. For a given event, the accidental noise rate adds on average 0.01 to 0.1 hits in the entire DHCAL prototype, where 1 hit corresponds to about 60 MeV.

Muon calibration

At Fermilab, muons traversing the DHCAL were collected using the 32 GeV/c secondary beam, a 3 m long iron absorber and a trigger based on the coincidence of a pair of 1×1 m^2 Scintillator paddles located upstream and downstream of the detector. Muon events were used to measure the local response of RPCs (efficiency and average pad multiplicity) in the DHCAL and TCMT. As an example, Figure 4.3.7 (left) shows the MIP detection efficiency ε_i, the average pad multiplicity μ_i and the so-called calibration factors, $c_i=(\varepsilon_i\mu_i)/(\varepsilon_0\mu_0)$, as measured with two different techniques (tracks and track segments) versus layer number.

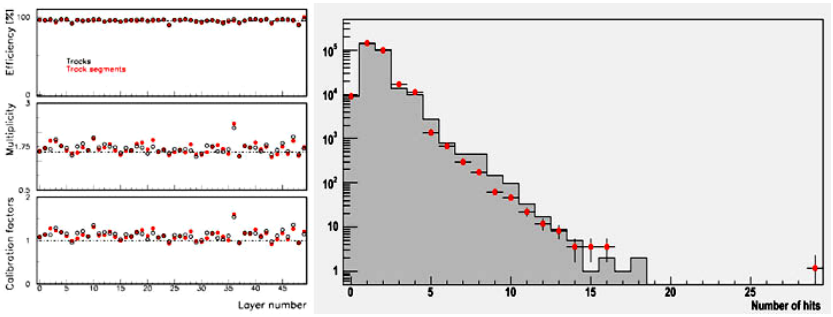

Figure 4.3.7: Left: MIP detection efficiency, average pad multiplicity and calibration factors as function of layer number, as measured with both tracks and track segments; Right: response of a detector layer to muons averaged over the entire DHCAL with the histogram (data points) showing data (simulation).

The average response in clean regions of the stack, i.e. away from borders and fishing lines, was measured and is being used to tune the Monte Carlo simulation of the RPC response. Figure 4.3.7 (right) shows a comparison of the measured and simulated RPC response.

Positron response

Secondary beam particles were collected at momentum points covering the range of 1 to 60 GeV/c at the Fermilab test beam. Data with the primary 120 GeV proton beam were also collected. The trigger (provided by the coincidence of two 19 $\times$ 19 cm^2 scintillator paddles positioned upstream of the DHCAL) accepted positrons and hadrons indiscriminately. The particles were later identified offline based on the information from the Cerenkov counters and shower shape.

The mean response of the DHCAL (before calibration) to identified positrons is shown in Figure 4.3.8 (left). The response is fit with the nonlinear function $N=a+bE^m$. The fit

describes the data well and is in accordance with the predictions in the VST results of positron showers [47]. In order to measure the electromagnetic energy resolution of the DHCAL the positron response need to be corrected for non-linearity. Figure 4.3.8 (right) shows the electromagnetic energy resolution for both uncorrected and corrected values.

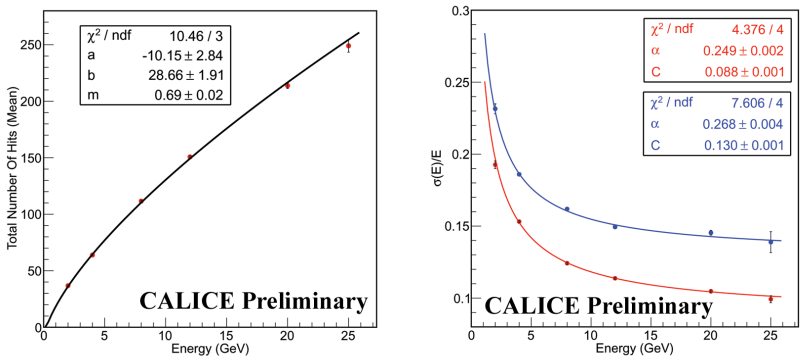

Figure 4.3.8: Left: Mean response of DHCAL to positrons; Right: Non-linearity corrected (blue) and uncorrected (red) electromagnetic energy resolution for DHCAL.

Pion response

The mean response of the DHCAL (before calibration) to pions is shown in Figure 4.3.9 (left). The response is linear up to 25 GeV, and at 32 GeV, the response deviates from linear behaviour due to RPC response fluctuation and possible saturation effect. Therefore, 32 GeV data point is not included in the linear fit (N=aE where N is the total number of hits and E is the beam energy). Figure 4.3.8 (right) shows the hadronic energy resolution of the DHCAL with the current particle identification algorithms. The fits represent the data well and for the longitudinally contained pions -that have no hits in the last two layers- a stochastic term of approximately 55% and a constant term of 7.5% is achieved. The measurements are within 1-2% of predictions based on the simulation of the large-size DHCAL prototype using the VST results [48].

With the data analysis still in a preliminary state, there are nevertheless a few conclusions to be drawn regarding an RPC-based digital hadron calorimeter:

- The RPC technology appears to satisfy the requirements of the active media of a highly segmented calorimeter.

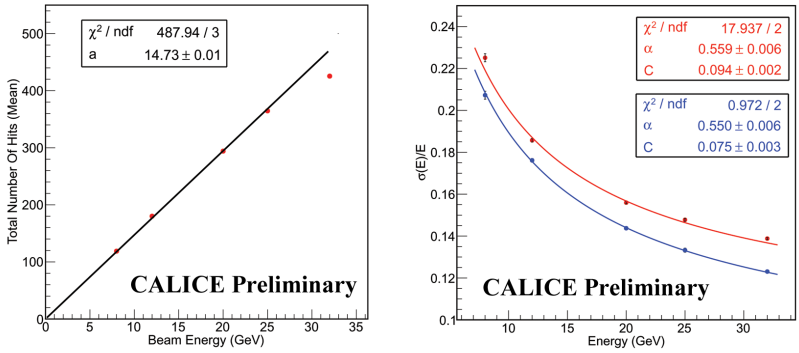

Figure 4.3.9: Left: Mean response of DHCAL to pions; Right: hadronic energy resolution of DHCAL for all identified pions (red) and the longitudinally contained pions (blue).

- The dark rate in the DHCAL is very low and corresponds to a negligible amount of energy added to a single event.
- The response to positrons is as expected and consistent with predictions based on the VST [47]. As expected the response to positrons is non-linear, due to saturation effects introduced by the finite size of the readout pads.
- The response to pions is as expected and consistent with predictions based on the VST [48]. The response appears to be linear up to about 30 GeV/c.
- Using Tungsten absorbers instead of Steel plates leads to a reduced number of hits, by about 30%. To extend the range of the linear response beyond 20 GeV, a finer segmentation of the readout is required. It is conceivable that the application of software compensation techniques, which utilise the density of hits, is able to restore the linearity and improve the resolution at these higher particle energies.

4.3.6 R&D towards technical feasibility and optimisation

The DHCAL prototype was designed for proof of principle, R&D in several areas are still critical to demonstrate the technical feasibility and achieve design optimisation:

- The front-end of the DHCAL readout need to have significantly reduced power consumption, in order to avoid active cooling. Low power ASIC design techniques and

power pulsing scheme are being considered to reduce the power dissipation by a factor of $\sim$100.

- The digital part of the readout system need to be optimised for better data concentration and reduced number of data connections without sacrificing reliability. Several ideas, including token ring passing and wireless data link, are being considered.
- A novel 1-glass RPC design is being developed, which features distinct advantages, such as an average pad multiplicity close to unity, a thinner chamber, a higher rate capability and a generous insensitivity to the surface resistivity of the resistive paint. The feasibility of larger chambers based on this design needs to be established.
- The high rate RPC could be a nice solution for the forward region of the DHCAL. The group is currently collaborating with several other institutes in developing low resistivity glass and Bakelite material for high rate RPC.
- The group is pursuing the development of a realistic design of a DHCAL module. Several configurations are being considered.
- A high voltage distribution system is being developed which is capable of turning onoff, adjust voltage value, and monitoring the current of individual chambers from a single high voltage input source.
- In order to operate a large DHCAL system at a future colliding beam experiment, a gas recirculation system is needed for both cost and environmental considerations. Initial development has started.

4.3.7 Calibration of a Digital Hadron Calorimeter

The event record for the DHCAL will contain a list of hits and their location. The energy of a hadron E_h will be reconstructed as described in formula 4.3.1. In a running experiment, one needs to determine α_{sample}, ε_0, μ_0, and constantly monitor ε_i, μ_i and N_{noise}.

Sampling fraction and energy scale

The sampling fraction α_{sample} for charged hadrons can be measured by placing detector modules into a pion test beam of varying energies, which can also determine the energy dependence. The test beam data can also be used to validate a simulation procedure to reproduce the response of the modules to charged pions. The response of the modules to neutral hadrons will be simulated and the sampling term for neutral hadrons will be determined.

The overall energy scale of the jets reconstructed at the ILC will be cross checked using di-jet events and reconstructed W and Z boson masses. At $\sqrt{s} = 500$ GeV with an integrated luminosity of 1 fb^{-1}/day we expect to collect 2,800 (1,900) di-jet (W^+W^-) events/day. With enough statistics the dependence of the reconstructed jet energy on the electro-magnetic fraction of a jet or the fraction of neutral hadrons in a jet can be studied.

Monitoring of individual RPC's

Under fixed operating conditions (high voltage and threshold setting) the performance of RPCs depends on the ambient temperature, the atmospheric pressure and, for completeness, the gas flow. The last item only impacts the noise rate and the pad multiplicity. However, above a minimum gas flow these are seen to be constant and do not depend on variations of the flow. The performance of the RPCs does not depend on the ambient air humidity.

The dependence on the environmental conditions can be parameterised [44] as

$$\Delta\varepsilon = [-0.06 \cdot \Delta p(100Pa) + 0.3 \cdot \Delta T(^0C)]\%$$

$$\Delta\mu = [-0.25 \cdot \Delta p(100Pa) + 2.0 \cdot \Delta T(^0C)]\%$$

In the following we assume that the changes in performance are uniform within an entire chamber. Two methods will be employed to monitor the chamber's performance: one utilising track segments in events from ILC collisions and the other utilising cosmic rays.

- Track segment monitoring

  Imaging calorimeters offer the possibility to reconstruct individual track segments within hadronic showers [46] or in $e^+e^- \to \mu^+\mu^-$ events. Such track segments can be used to monitor the MIP detection efficiency ε_i and the pad multiplicity μ_i of individual RPC's during the data taking period.

  It is estimated that a 3% measurement is achievable, either using track segment method or muon tracks, within approximately 5 days of running.

- Cosmic ray monitoring

  Cosmic rays are an ideal tool to monitor the performance of the chambers. With a crude estimate of the underground muon flux, horizontal chambers with an area of 2 m^2 obtain 1000 measurements per minute. The rate in vertical chambers will be reduced by say one order of magnitude. Nevertheless, the required precision of 3% can be obtained in less than one hour.

However, if the front-end power is pulsed, this will lead to a reduction in duty cycle of up to a factor of 200. In this case, time estimate needs to be increased to approximately 1 week. Further studies are needed to understand the cooling needs of the DHCAL and to define the optimal duty factor, taking into account the need for monitoring the performance of the RPCs.

In long-term studies of prototype RPCs, the efficiency and pad multiplicity were seen to vary by $\pm 0.9\%$ and $\pm 5\%$, respectively. Applying corrections for the environmental conditions (i.e. ambient temperature and air pressure) based on the above mentioned equations reduces these variations to $\pm 0.8\%$ and $\pm 3\%$.

Based on detailed simulations of the response of RPCs the effect of uncertainties in the calibration on the measurement of single particle energies was estimated. The studies showed that, for instance, for 10 GeV π^+ the energy resolution degrades by approximately by 1%, if the entire module's response is smeared by a Gaussian distribution with a sigma of 3%. This is the worst case scenario, where the responses of all layers in a given module are 100% correlated. If, on the other hand, all individual layers in a module fluctuate independently say by a Gaussian distribution with a sigma of 3%, the effect on the energy resolution is negligible.

Measurement of the noise rate

The background rate can be measured utilising the self-triggered mode of the front-end readout. Measurements on the prototype chambers typically showed a background rate of 0.1 - 0.2 Hz/cm^2 at room temperature. As an example Figure 4.3.10 shows the noise rate as function of high voltage setting for the same threshold as in the test beam.

Assuming a gate width of 200 ns and a total of 5×10^7 readout channels, the expected noise rate at the ILC will be about 2 hits/event in the entire DHCAL. Assuming a calibration of 13.6 hits/GeV, as obtained in recent simulations of the DHCAL, the noise contribution corresponds in average to around 150 MeV/event and can be ignored for all practical purposes.

Beam related background rates, due to neutrons for instance, will be measured using bunch-crossing events and algorithms for separating energy deposits from e^+e^- collisions and from beam backgrounds.

4.3.8 Alternative technologies

A number of viable alternative approaches to PFA-based hadronic calorimetry are also considered by SiD. Two, GEM and Micromegas, use advanced micro-pattern gas detector technologies benefitting from participation in the RD51 collaboration. A third approach uses

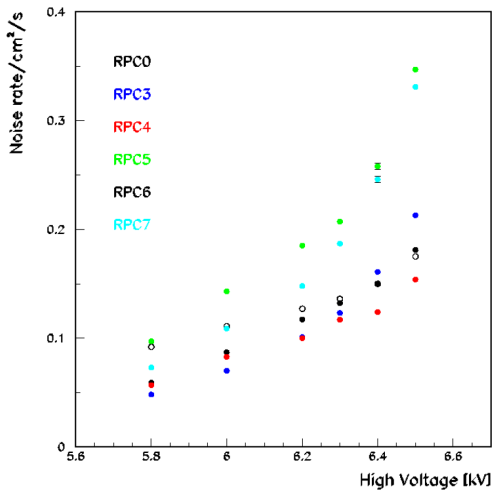

Figure 4.3.10: Noise rate as function of high voltage for six different chambers. The threshold was set at the default value of 110 counts. The default high voltage setting was 6.2 kV.

small scintillator tiles readout by silicon photomultipliers. As for the baseline RPC approach, all these alternatives are the subject of development within the CALICE collaboration.

GEM

We have also been developing a digital hadronic calorimeter (DHCAL) using GEM as the sensitive gap detector technology. GEM detectors can provide flexible configurations which allow small anode pads for high granularity. It is robust and fast with only a few nanosecond rise time, and has a short recovery time which allows a higher rate capability than other detectors. It operates at a relatively low voltage across the amplification layer, and can provide high gain using a simple gas ($ArCO_2$), which protects the detector from long term degradation issues, and is stable. The ionisation signal from charged tracks passing through the drift section of the active layer is amplified using a double GEM layer structure. The amplified charge is collected at the anode layer with pads at zero volts. The GEM design allows a high degree of flexibility with, for instance, possibilities for micro-strips for precision tracking layer(s) and variable pad sizes and shapes. Figure 4.3.11 depicts how the double GEM approach can be incorporated into a DHCAL scheme.

A number of double GEM chambers have been built and tested with cosmic rays,

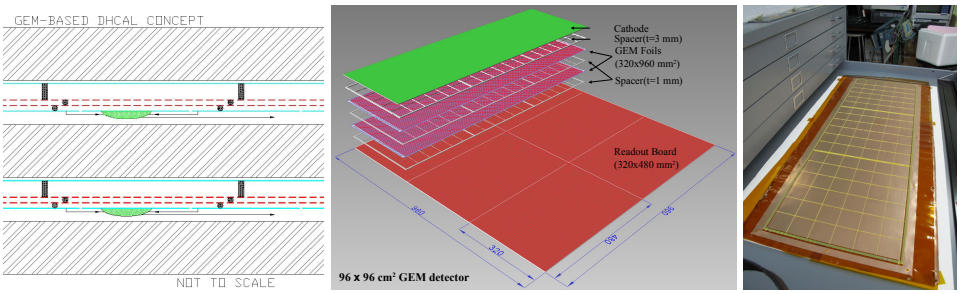

Figure 4.3.11: Left: GEM DHCAL Concept. Centre: Drawing of the large-area GEM chamber. Right: Large-area GEM chamber under construction.

sources, and test beam. Stable operation has been achieved with 390 V across each GEM foil, leading to a gain of 11,000. The resulting typical MIP signal size is 40-50 fC, well above the noise level from the readout KPiX chip from SLAC.

The next step in developing the GEM approach to digital hadron calorimetry is the construction of a number of 1 m $\times$ 1 m layers for exposure as part of a 1 m^3 test beam stack. 1 m x 33 cm foils developed with CERN are being used to assemble double-GEM prototypes of the same size. Following this, a number of 1 m $\times$ 1 m layers will be assembled. Figure 4.3.11 shows a schematic view of one of the 1 m $\times$ 33 cm layers under construction.

Single thick-GEMs [49] are also considered as an alternative to the double-GEM structure discussed above. A thick-GEM consists of a single circuit board about 0.5 mm thick and having holes of 200-400 µm in diameter. An advantage of thick-GEMs is a possible reduction in overall DHCAL active layer thickness and easier handling and construction compared with regular thin foils.

Micromegas

Introduction Digital calorimeters proposed for ILC or CLIC are expected to suffer from saturation due to the high particle multiplicity in the core of the showers. The resulting loss of linearity and resolution can in principle be mitigated if more than one threshold is used. A necessary condition for this approach to work is the proportionality between cell signals and the number of traversing particles. On average, this condition is met in Micro Pattern Gas Detectors like GEM and Micromegas because they are free of space charge effects.

Micromegas is a fast, position sensitive Micro Pattern Gas Detector operating in the proportional mode [50]. It functions in simple gas mixtures (*e.g.* Ar/CO_2) and at low fields and voltages ($<$ 500 V) and is thus extremely radiation hard. It is an alternative to RPCs that offers lower hit multiplicity and proportional signals well suited for a semi-digital readout.

On the other hand, Micromegas suffers from discharges but efficient protections exist.

Micromegas chambers developed for the active part of a semi-digital HCAL (SDHCAL) consist of a commercially available 20 µm thick woven mesh which separates the gas volume in a 3 mm drift gap and a 128 µm amplification gap (so-called Bulk). Micromegas of 32 $\times$48 cm^2 acting as signal generating and processing units have been designed and fabricated. They were used to construct three chambers of 1 m^2 size which are described below.

Mechanical layout and assembly The 1 m^2 chamber features 9216 readout channels (1 $\times$1 cm^2 anode pads) and consists of six Printed Circuit Boards (PCB) of 32 $\times$48 cm^2 placed in the same gas chamber. Front-end chips and spark protection circuits are first soldered on the PCBs. Then a mesh is laminated on the opposite pad side of each PCB to obtain an Active Sensor Unit (ASU). Having 6 meshes instead of a single larger one decreases proportionally the energy that is released in the front-end electronics circuitry during a spark (Figure 4.3.12).

Small spacers (1 mm wide, 3 mm high) are inserted between ASUs and support the cathode cover, defining precisely the drift gap. Plastic frames are closing the chamber sides, leaving openings for two gas pipes and flexible cables. The chamber is eventually equipped with readout boards and a patch panel for voltage distribution. The total thickness amounts to 9 mm which includes 2 mm for the steel cathode cover (part of the absorber), 3 mm of drift gap and 4 mm for PCB and ASICs. With this mechanical design, less than 2% of inactive area is achieved.

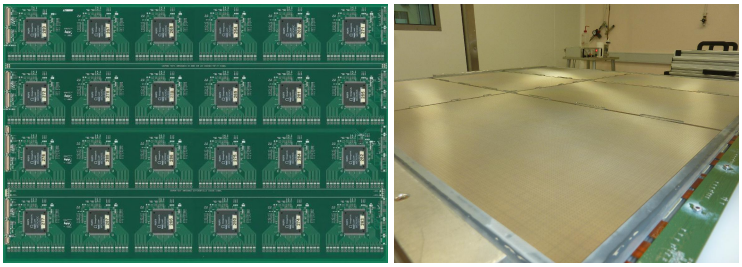

Figure 4.3.12: *One Active Sensor Unit (ASIC side) and the 1 m^2 prototype during assembly.*

Performance to MIPs The response to minimum ionising particles (MIPs) was studied in a 150 GeV/c muon beam at CERN/SPS. The 1 m^2 chamber was flushed with a non-flammable mixture of Ar/CF_4/iC_4H_{10} 95/3/2, the mesh voltages were varied between 300-420 V (gas gain G of 100-8000). A profile of the beam recorded in internal trigger mode is

shown in Figure 4.3.12 (left) and indicates that the noise level can be kept low and uniform.

The strong dependence of the detection efficiency on the applied voltage is shown in Figure 4.3.12 (centre). Thanks to the very low readout threshold (1-2 fC), a gas gain as low as 10^3 (at 365 V) is sufficient to detect MIPs with an efficiency larger than 95%. Upon full exposure of two chambers, detailed efficiency maps over 8 $\times$8 cm^2 regions were produced revealing an efficiency of (96 $\pm$ 2)% (Figure 4.3.12 (right)). Such a little variation indicates a good control of the chamber dimensions (gas gaps) as well as of the electronics parameters (gains, thresholds).

A benefit of Micromegas w.r.t. other gas detector technologies is the limited spatial extension of the avalanche signals. As a result of the little transverse diffusion experienced by the electrons in the gas (100-150 µm RMS), the hit multiplicity is below 1.15 up to 390 V (G = 3000). At higher gains, neighbouring pads become sensitive to single electrons, increasing the multiplicity to 1.35 at 420 V (G = 8000). There is however no reason to work in that regime as high MIP efficiency is reached at lower gains (G = 1000).

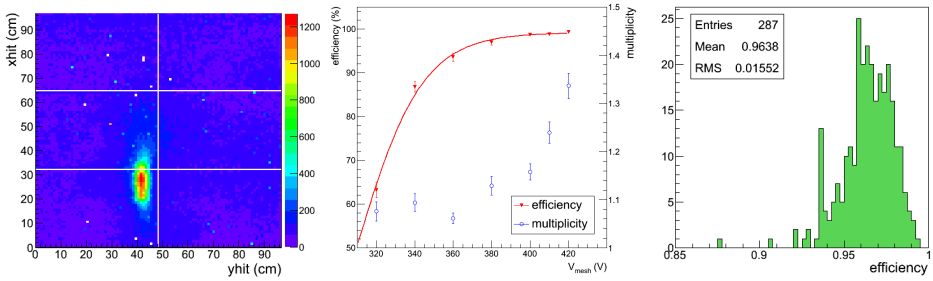

Figure 4.3.13: *Muon beam profile using internal trigger mode (left) efficiency and pad multiplicity.*

Performance to pions The response of the chamber to hadronic showers was studied with pions using first a 20 cm long block of iron (1 λ_I) upstream of the chamber. Later, two chambers were inserted inside the Fe/GRPC SDHCAL in the last two layers, behind 5 λ_I.

Directing a 150 GeV/c pion beam at the iron block, the distribution of the number of hits in the chamber was measured at mesh voltages of 325, 350 and 375 V (G of about 350, 800 and 1700). The number of hit distributions, shown in Figure 4.3.14 (left), exhibit a peak at $N_{\rm hit}$ = 1 and a long tail from penetrating and showering pions respectively. The distributions at 350 and 375 V yield different efficiency to penetrating pions but remarkably, have a similar tail. Accordingly, a gas gain as low as 800 is sufficient to image most of the shower. Such a low working gas gain greatly improves the stability of the detector.

A good understanding of the detector is being achieved by comparing test beam data to Monte Carlo predictions. Preliminary results are presented in Figure 4.3.14 (right) which shows the distribution after 5 λ_I of Fe for 100 GeV pions. The readout threshold was tuned so as to reproduce the efficiency to muons (Figure 4.3.14 (centre)). A satisfactory agreement is obtained for muons and pions meaning that the simulation is reliable. It should be stressed that no noise was introduced in the simulation, therefore, data are essentially free of noise.

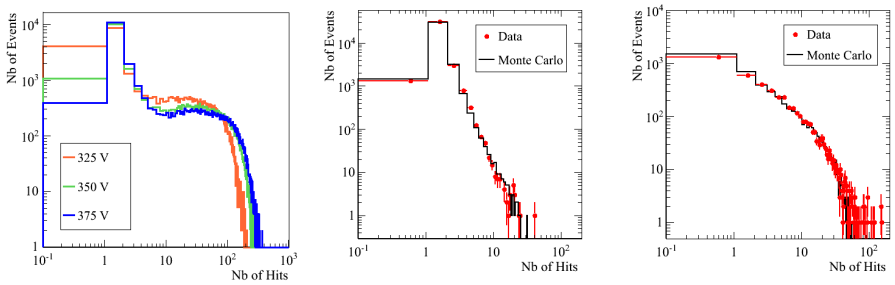

Figure 4.3.14: Hit distribution from 150 GeV/c pions traversing a 20 cm thick iron block at various mesh voltages (left). Hit distributions from 100 GeV muons (centre) and pions (right) at layer 48 of the CALICE Fe/GRPC SDHCAL.

Scintillators

The CALICE Collaboration has been pursuing the design and prototyping of a fine granularity scintillator-based hadron calorimeter. This option capitalises on the marriage of proven detection techniques with novel photodetector devices. The main challenge for a scintillator-based calorimeter is the architecture and cost of converting light, from a large number of channels, to electrical signal. Studies demonstrate that small tiles (4-9 cm^2) interfaced to Silicon Photomultipliers (SiPMs)/Multi Pixel Photon Counter (MPPC) photodetectors [51], [52] offer an elegant solution. SiPM/MPPCs are multi-pixel photo-diodes operating in the limited Geiger mode. They have distinct advantage over conventional photomultipliers due to their small size, low operating voltages and insensitivity to magnetic fields. The *in situ* use of these photodetectors opens the doors to integration of the full readout chain to an extent that makes a high channel count scintillator calorimeter entirely plausible. Also, in large quantities the devices are expected to cost a dollar per channel making the construction of a full-scale detector instrumented with these photo-diodes financially feasible.

A $\sim$ 1 m^3 size scintillator-SiPM prototype [53] has been designed, constructed and exposed to a test beam during the 2006-2009 period at CERN and Fermilab (see Figure 4.3.15).

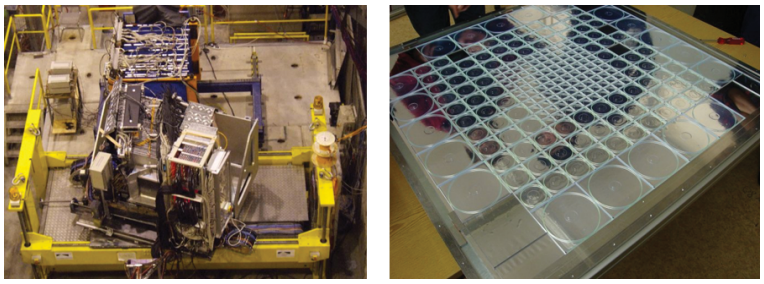

Figure 4.3.15: CALICE test beam setup at CERN (left) and an active layer of the scintillator-SiPM prototype (right)

The active layers have subsequently been embedded in a tungsten stack which has collected data in the 2010-2011 period. Over numerous run periods the technology has proven to be versatile and robust, millions of electron, pion and proton events in the 2-180 GeV/c range were written to disk. Ongoing analysis of the data collected, has gone a long way in establishing the scintillator-SiPM option as a calorimeter technology (see Figure 4.3.16), benchmarking hadron shower simulations [54] and testing the particle-flow paradigm using hadrons from real data [55].

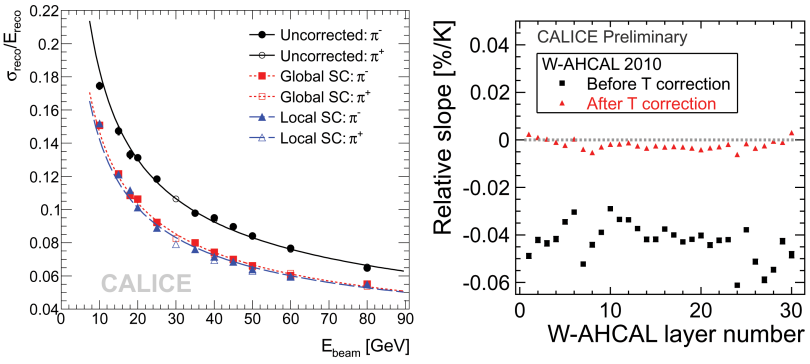

Figure 4.3.16: Single pion resolution using simple energy sum and software compensation techniques (left) and slope of the SiPM response temperature dependence for AHCAL layers without and with temperature correction (right)

The focus of the current and future R&D effort is to demonstrate the scalability of this technology taking into account the stringent constraints on the power consumption and me-

chanical compactness through the development of an Integrated Readout Layer (IRL). In general for the IRL, it is proposed to have a printed circuit board (HCAL Base Unit or HBU) inside the detector which will support the scintillator tiles, connect to the silicon photodetectors and carry the necessary front-end electronics and signal/bias traces (see Figure 4.3.17). This can however be achieved in a number of ways and a number of promising complementary approaches (e.g.fibre vs. direct or fibreless coupling of SiPMs to the tiles) have been developed in a coordinated fashion such that they can be characterised in a common electronics environment. This next generation front-end electronics carried aboard the HBUs is capable of self-triggering, precise time stamping, channel-by-channel bias control and a built-in LED calibration system. Commissioning of these readout slabs is at an advanced stage and is expected to expand into exposure in electron and hadron test beams in the near future.

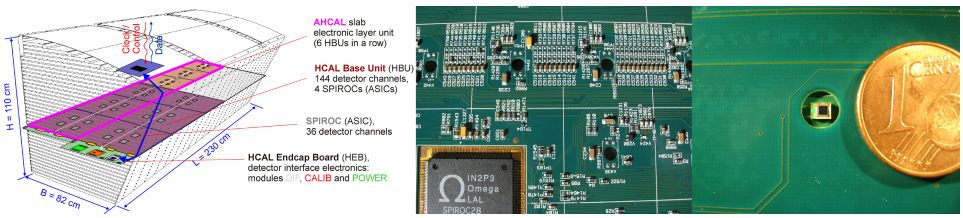

Figure 4.3.17: Conceptual design of a barrel wedge instrumented with IRL planes (left), a HBU prototype (centre) with a MPPC surface-mounted on it (right).

4.4 Summary

We have a silicon-tungsten electromagnetic calorimeter design that can satisfy the PFA requirements. We have developed a first-level mechanical design and have all the components and processes in place to construct and test a full-depth prototype. The technologies for PFA-based hadron calorimetry have seen significant development and testing since the submission of the SiD LOI. The construction of the cubic metre HCAL stack in the baseline RPC technology has provided much practical experience and confidence towards producing a full detector in this technology. The test beam data, providing unprecedented detail on hadronic showers, have shown that this is indeed a very promising technology, in the PFA context, for the SiD detector. We have also benefitted from the development of several alternative technologies.

Chapter 5

Muon System

The SiD muon system is designed to identify muons from the interaction point with high efficiency and to reject almost all hadrons (primarily pions and kaons). The muon detectors will be installed in the gaps between steel layers of the solenoid flux return. The required position and rate capabilities of the detectors are modest and can be met by several different detector technologies. The baseline design uses double layers of extruded scintillator strips read out by silicon photomultipliers (SiPMs). Resistive plate chambers (RPCs) are also under consideration as an alternative design.

The SiD muon selection will combine information from the central tracker, calorimeter, and muon detectors to construct 3-dimensional tracks through the entire detector for each muon candidate. Candidates will be required to penetrate a number of interaction lengths consistent with the muon momentum. In addition, the observed number and position of hits along the fitted track length can be used to further discriminate against hadrons. The first layers of the muon system may also be useful as a tail-catcher for the hadronic calorimeter.

Muon systems characteristically cover large areas and are difficult to access or replace. Reliability and low cost are major requirements. Over 2.4 m of steel thickness will be required for the solenoid flux return, providing > 13 nuclear interaction lengths to filter hadrons emerging from the hadron calorimeter and solenoid. Since the central tracker will measure the muon candidate momentum with high precision, the muon system only needs sufficient position resolution to unambiguously match calorimeter tracks with muon tracks. Present studies indicate that a resolution of ≈ 2 cm is adequate. This can be achieved by two orthogonal layers of 4 cm wide extruded scintillators or RPC pickup strips.

Full optimisation of the muon system design has not been completed. The total steel thickness is set by the solenoid flux return requirements. To check that the present design is thick enough we studied the misidentification rate of pions between 10 GeV and 50 GeV as a function of the depth in the flux return. As shown in Figure 5.0.1, requiring that the track

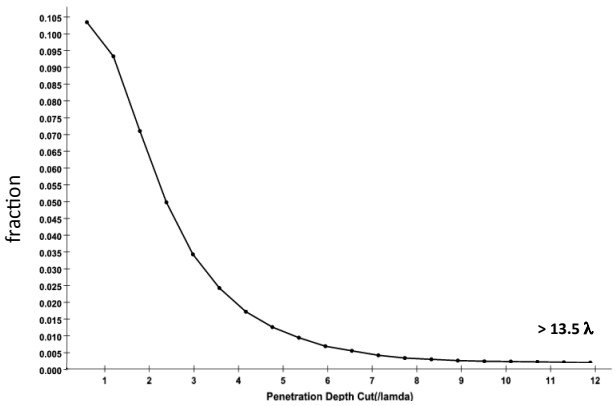

Figure 5.0.1: Misidentification of pions as a function of the depth of the last hit muon layer.

makes hits in some of the outer layers is sufficient to reduce the pion misidentification rate to 0.25%, consistent with the expected level of pion to muon decays. The present design, shown in Figure 5.0.2 has ten layers in the barrel section and nine layers in each endcap door. This provides a comfortable level of redundancy (≥ 6 layers) even in the region between the barrel and endcap. The optimum number of detector layers to cover the muon identification and tail catching functions was also studied for the CLIC case [56], where nine layers were found to be sufficient.

5.1 Backgrounds

Backgrounds in the muon system are expected to come primarily from beam losses upstream of the detector. The muon system is shielded from backgrounds generated at the collision point or along the internal beam lines by the calorimeters, which are greater than five absorption lengths thick. Therefore only penetrating backgrounds, such as high-energy muons or neutrons, affect the barrel muon detectors. Calculations [57] of the expected background from muons produced by collimators near the detector hall predict a rate of 0.8 muons/cm^2 per pulse train (1 ms) without muon spoilers, which is reduced to 3×10^{-3}/cm^2 per pulse train with the addition of muon spoilers. Physics backgrounds from two-photon processes producing hadrons or muon pairs significantly increase the expected signal rate in the endcap detectors near the beamline. At a radius of 22 cm the expected rate from hadrons and muons above 2 GeV is $\leq 0.04/\text{cm}^2$ per pulse train. The endcap detectors can also be hit by electromagnetic shower debris from local beam losses and may require additional shielding

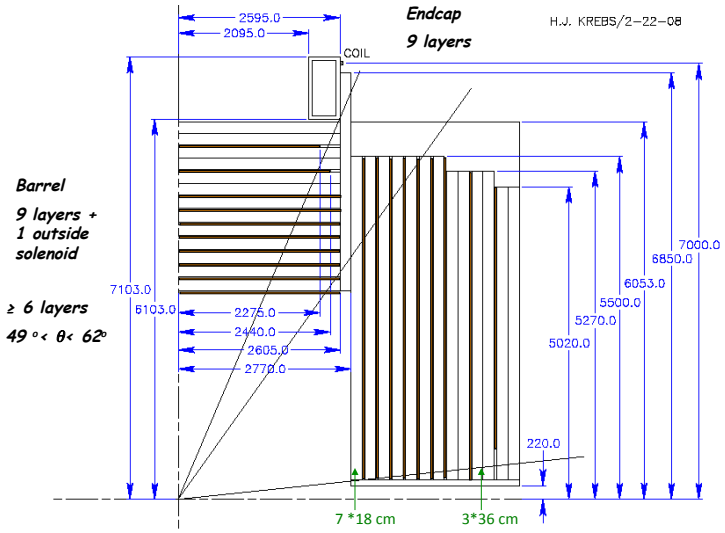

Figure 5.0.2: Quarter section view of the SiD steel flux return.

5.2 Detector design

The muon system will start outside of the highly segmented electromagnetic and hadronic calorimeters and the 5 T solenoid cryostat at a radius of 3.3 m. In the design shown in Figure 5.0.2 the barrel flux return is divided into seven layers of 18 cm steel and three layers of 36 cm steel in an octagonal barrel geometry. Endcaps of seven 18 cm thick steel octagons plus three 36 cm octagons will cap both ends of the barrel. The muon detectors will be inserted in the 4 cm gaps between the plates. In the barrel a detector layer is also inserted between the solenoid and the first steel plate. The size of the first barrel layer within each octant is approximately 2.9 m by 5.5 m, while the last layer is 4.7 m by 5.5 m. The total detector area needed in the barrel is $\approx$ 1600 m^2.

The endcap design is shown in Figure 5.2.1 (left). Each octagonal layer is made from three steel plates bolted together. The spacers between layers are staggered as seen in Figure 5.2.1 (right) to reduce projective cracks in the muon detection. The endcap detectors are subdivided by the spacers into rectangular or trapezoidal modules $\approx$ 1.8 m by 5.5 m. Each endcap has a total detector area of $\approx$ 1000 m^2.

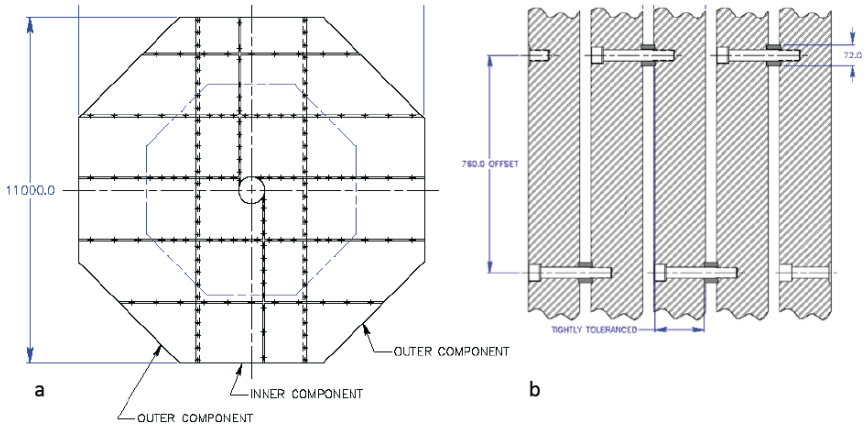

Figure 5.2.1: (left) Each layer of the endcap flux return is made of three vertical steel pieces bolted together. (right) Horizontal spacers separating the steel layers are offset by 0.7 m in alternate layers to avoid projective cracks.

5.2.1 Scintillating strips

Extruded scintillating strips have been used in MINOS [58] and T2K [59] and are planned for $\mu 2e$ [60] and SuperB [61]. Wavelength shifting fibre is run down the centre of each strip. A TiO_2 reflective coating is co-extruded on the outside of the scintillator. The fibres extend out of the strips by ~ 1 cm and are readout by SiPMs

The baseline muon detector employs 1 cm thick by 4.1 cm wide scintillating strips, arranged in back-to-back twin-planes with perpendicular strips as shown in Figure 5.2.2 (left). In the barrel strips in one plane are parallel to the beam direction (z-strips), while those in the adjacent plane are orthogonal (r, ϕ strips). These layers are glued together with aluminium sheets to form a rigid module. The aluminium sheets provide support while optically isolating the two layers. In the endcap, Figure 5.2.2 (right), the gaps between the steel layers are broken up by rows of horizontal spacers. The vertical strips are short (≈ 1.8 m) while the horizontal strips are ≈ 5.5 m long.

Particles emerging from e^+e^- collisions at the interaction region create optical pulses via dE/dx when traversing the scintillator strips placed in the gaps of the barrel and endcap Fe return yokes. A fraction of the light is captured in a 1.2 mm diameter wave-length shifting (WLS) fibre located in a groove that runs along the length of the scintillator bar. The light travels through the WLS over 2 m to 5 m distance before reaching the input face of a Si photo-diode (SiPM) matrix, where it triggers an avalanche in one of the few-hundred micron-sized individual photo-diodes cells whose outputs are ganged together through in-

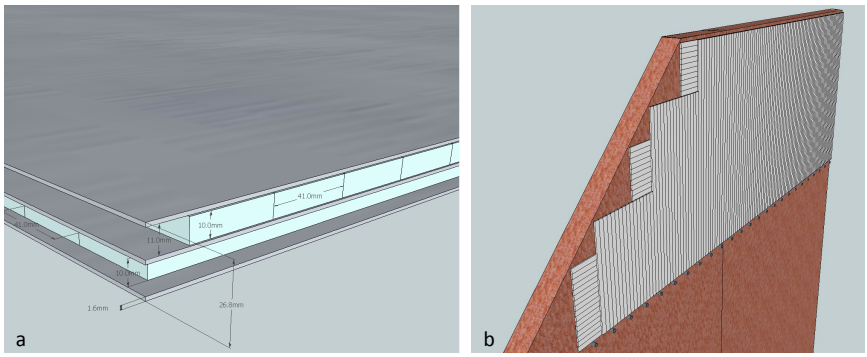

Figure 5.2.2: (left) Each gap in the barrel flux return is filled by two orthogonal planes of scintillating strips glued to three aluminium sheets to form a rigid rectangular sandwich. (right) The endcap modules are ≈ 1.8m high to slide between the spacers separating the endcap steel layers.

dividual output resistors to a common output. In our tests of candidate SiPMs for muon detection we have focused on devices with ≈700 cells with 40 µm × 40 µm size fitting inside a 1.2 mm diameter circle [62]. As the cells in the Si matrix have good uniformity with similar areas and Si thicknesses, the summed avalanche signal output of the ganged cells is proportional to the number of cells hit. Therefore the devices can be calibrated adequately by using the individual photoelectron peaks in the summed signal of the SiPM. The calibration procedure makes use of peaks with one or two photoelectrons, as well as noise peaks. Signals from individual SiPMs are then sent on to receivers and collected for further digital processing.

There are 7,451 axial barrel channels where both ends of the fibres are read for the barrel strips, making 14,902 readout channels. There are 10,810 (r, ϕ) scintillator strips that add 10,810 single ended readout channels to make the barrel (B) channel count 25,712. The reason for not reading out both ends of the (r,ϕ) strips is that there are more and consequently shorter WLS fibres (less occupancy) and less attenuation in these barrel channels. All the outer periphery ends of the Forward/Backward (F/B) channels are read (no double-ended readout). The F/B strip-scintillator planes add a 21,620 scintillator strips (21,620 channels of readout and electronics) to make a total of 25,712 central and 21,620 F/B in back-to-back quadrants for a total of 47,332 channels. The sum of WLS fibre and scintillator totals ≈ 164 km (≈ 86 km for the ten barrel planes and ≈ 78 km for the nine endcap planes).

Recently the University of Virginia HEP group have developed small molded plastic parts that capture the detector end of the WLS fibre and accurately position it relative to the centre of the SiPM which has 600 Si pixels contained inside a circular area of 1.2 mm

diameter. With this kind of connection of the polished signal fibre to the photodetector it should be possible to locate the readout devices on a separate long plastic or fibreglass strip that accepts the WLS ends for a plane or half plane of detectors as drawn in Figure 5.2.3.

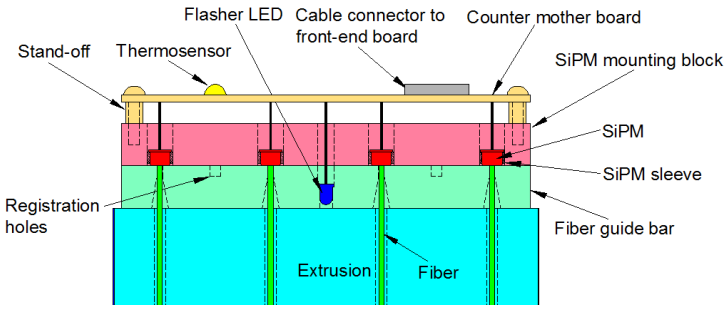

Figure 5.2.3: SiPMs are positioned at the end of each fibre by a SiPM mounting block and fibre guide.

A prototype strip/SiPM combination was tested in Fermilab Test Beam Experiment T995. Two 3.6 m long strips were connected by fibre to make an effective 7.2 m long strip. SiPMs were glued on both ends of the fibre. Beam was scanned along the length of the strip to study pulse height as a function of the distance from the SiPM. As seen in Figure 5.2.4 the number of photoelectrons can be easily counted on either end of the strip even if the beam is placed near one end. The pedestal was quite small and stable. Requiring two or more photoelectrons eliminates nearly all of the noise signals.

In Figure 5.2.5 multiple beam positions in two different prototype strips were used to measure the attenuation of the light signal with fibre/strip length. The data can be modelled by the sum of two exponential fall-offs. Near the sensor, the attenuation length is ~ 2.9 m. At 7 m from the sensor, the attenuation length is ≈ 6.5 m. Since the longest strips in SiD are less than six meters long the minimum expected pulse height is > 5 photoelectrons. With a threshold of two photoelectrons the scintillating strips with SiPM readout are very efficient.

5.2.2 Resistive Plate Chambers

Many large RPC systems have been built within the last ten years and understanding their performance will provide strong guidance for an SiD design. Several types of RPC construction have been used in high energy experiments. RPCs with Bakelite cathodes and anodes, initially reported in [63], found application in *BABAR*, CMS, ATLAS and a variety of cosmic ray and neutrino experiments. RPCs are inexpensive to build and can be easily constructed in a variety of shapes and sizes. There are, however, a few concerns about the use of RPCs in

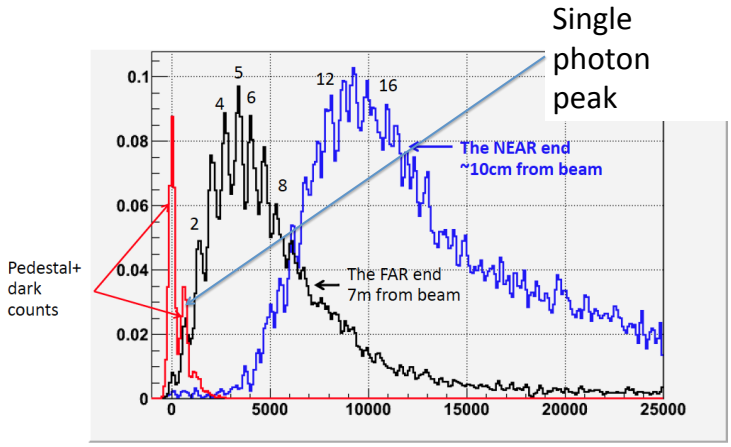

Figure 5.2.4: Test beam data of two strips coupled by fibre to simulate a single long strip. Pulse height from the top strip (blue) and the bottom strip (black) are shown. The beam is 10 cm from the end of the top strip.

future experiments. RPCs use fluorocarbon gases which are regulated as greenhouse warming gases and require nontrivial gas delivery systems adding to operational costs. Further restrictions on the use of fluorocarbon gases are possible in the future. RPCs have also had reliability problems (*BABAR* was forced to replace its original RPCs and Belle had startup problems). However, significant progress has been made in understanding RPC aging mechanisms. The current ATLAS [64] and CMS [65] detectors, which run in avalanche mode, have shown good stability even at the high background rates expected at the LHC. The second generation *BABAR* RPCs [66] and the Belle RPCs preformed reliably at the low signal rates ($< 0.2\text{Hz/cm}^2$) expected for SiD detectors. RPCs are a viable detector alternative for the muon system, particularly if the RPC option is chosen for the hadron calorimeter. Bakelite was chosen for the RPCs because for the foreseen plate thickness of 2 mm, glass is significantly heavier than Bakelite and more brittle. Given the large-area chambers needed for the muon system, a Bakelite RPC system is most likely easier to construct and install, hence a conservative choice was made.

A RPC design for the muon detector planes would utilise two layers of single gap RPC HV chambers (1×2 m) with orthogonal readout strips on either side assembled into modules of the required size to fill each slot in the octagonal barrel or endcap. The chamber size would be varied so that joints between chambers do not align in the top and bottom layer. If the single gap RPC efficiency is 90%, then an average module efficiency of 93% can be achieved.

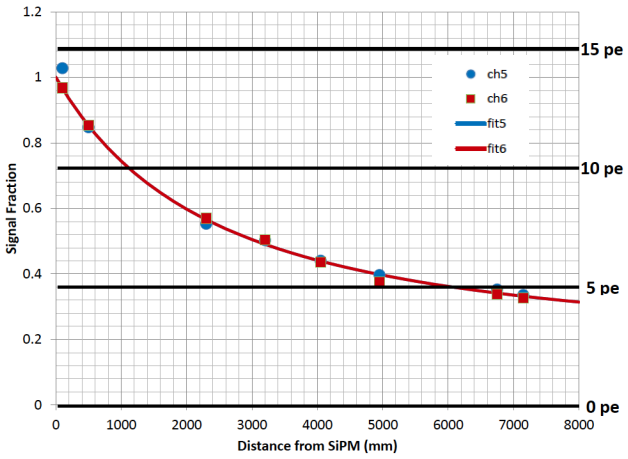

Figure 5.2.5: The fraction of the total light collected by the SiPM as a function of the beam position along the strip for two different strips (ch 5 and 6).

Close integration of the RPCs and front-end and digitisation electronics is necessary to minimise cabling and costs since the expected channel counts for the SiD detector are high (nearly one million for the muon system). One possible low cost solution that has been investigated is to adapt the KPiX chip, presently being developed for use in the SiD electromagnetic calorimeter, for use with RPCs. An RPC/KPiX interface board was designed and built to provide ribbon cable connections to a 64-channel KPiX chip (v7). The RPC strip signal is AC coupled to the KPiX input through a 5 nF blocking capacitor and a 2-stage diode protection network. Each strip is also tied to signal ground via a resistor external to the interface board.

A small (0.5 m $\times$ 0.5 m) test RPC with 13 strips was connected to the interface board by a 0.5 m cable. The chamber was operated at 9300 V in avalanche mode using a premix gas with composition of 75.5% Freon 134a, 19.4% Argon, 4.5% isobutane, and 0.5% SF6. The chamber efficiency had been previously measured to be $\approx$ 90% using *BABAR* electronics. The signal sum of the 13 RPC strips on the HV ground side (positive signal) is shown in Figure 5.2.6 (left). The sharp spike near zero is due to cosmic ray tracks that either missed the test RPC or to RPC inefficiency. The signal peak is centred at 3.8 pC with a width of 2.2 pC. The signal height is consistent with, but larger than, avalanche RPC signals measured by other groups ($\approx$ 1 pC), which used avalanche gases with no Argon component. The avalanche gas contains 19.4% Argon and is expected to have a higher gas gain. The charge distribution in the RPC pickup strips was also studied. For each trigger, the strip with

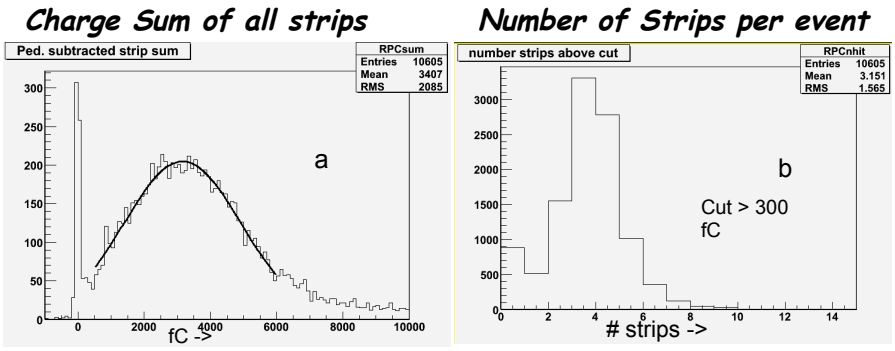

Figure 5.2.6: (left) Sum of the pulse heights in 13 RPC strips readout by a 64-channel KPiX chip (v7). The peak position of 3 pC and efficiency of $> 90\%$ are consistent with previous studies of avalanche mode RPCs. (right) The number of strips with a signal height above 300 fC per track.

the maximum charge has typically less than half of the total charge in the event. The strip multiplicity was measured as a function of the discrimination threshold. With a threshold of 300 fC, about 92% of the cosmic triggers have one or more strips hit and the average strip multiplicity is 3.1, more than twice that observed with *BABAR* electronics. Although a good proof of principle, these tests show that further characterisation and optimisation of the interface board between the RPC and chip is needed

Chapter 6

Superconducting Magnet System

6.1 Introduction

6.1.1 List of subsystems

The magnet subsystem consists of its own following subsystems:

1. A 6.8 m outside diameter $\times$ 6 m long 5 T superconducting solenoid with a separated iron plate flux return that is integral with the muon tracking system.

2. A superconducting 600 G dipole anti-dipole magnet (DID) integrated with the solenoid.

3. A power supply, a DC contactor, a pressurised water cooled dump resistor, and a conventional mechanical dump switch that move with the detector.

4. A 1.5 kW helium liquefier and 5000 litre LHe storage dewar that supply 4.5 K LHe to both the solenoid and to a pair of 2 K cold boxes for each of the superconducting focusing magnets (QD0).

5. Interconnecting cold, warm, and vacuum plumbing lines including those to QD0, mounted directly on the detector.

6. Controls and instrumentation for the magnets and helium liquefier.

The shared resource ILC helium compressor system and the two superconducting QDO focusing magnets with the internal design of their 2 K distribution boxes are not part of this subsection.

6.1.2 Design Philosophy

The superconducting solenoid is an expensive and technically challenging component. Its design is based on the successful 4 T CERN CMS superconducting solenoid, and thus a direct comparison is warranted in Table 6.1.1. High purity aluminium superconductor stabilisation with indirect LHe cooling will be used. The CMS individual self supporting winding turn design philosophy is used for SiD, becoming even more important due to the higher 5 T field and the increased radial softness of six layers versus four layers. Figure 6.1.1 is a cross-section of the SiD magnet.

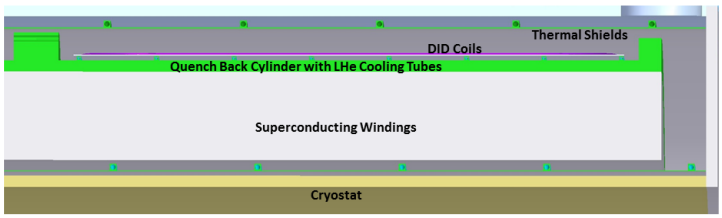

Figure 6.1.1: SiD Superconducting Magnet quadrant, showing: Solenoid with Winding/Quench Back Cylinder/LHe Cooling Tubes, Cryostat, Thermal Shields, and Detector Integrated Dipole.

The SiD solenoid has a stored energy per unit of cold mass of 12 kJ/kg that is only slightly larger than the CMS value. 12 kJ/kg is close to the upper bound that this type of large aluminium dominated magnet can be operated in a fail safe manner if the quench detection or energy extraction circuit were to fail. This specific energy density yields an average magnet temperature of 130 K. Prudent engineering for the SiD solenoid dictates that the total volume of aluminium stabiliser/structure cannot be reduced by much from the present baseline design.

6.2 Magnetic Field and Forces

6.2.1 Requirements and Design

The SiD magnet system requires a 5 T central field, an alternating 600 G field along the axis from the DID, and a fringe field of less than 100 G a meter from the outer iron surface. An economic solution to the fringe field requirement has not yet been found. It is certainly easily achievable with the addition of sufficient iron and air gaps. Some components such as the expansion turbines inside the helium liquefier will most likely require additional local iron shielding.

Table 6.1.1: SiD and CMS Superconducting Coil Comparison

Quantity	SiD	CMS	Units
Central Field	5.0	4.0	T
Stored Energy	1.59	2.69	GJ
Stored Energy Per Unit Cold Mass	12	11.6	kJ/kg
Operating Current	17.724	19.2	kA
Inductance	9.9	14.2	H
Fast Discharge Voltage to Ground	300	300	V
Number of Layers	6	4	
Total Number of Turns	1459	2168	
Peak Field on Superconductor	5.75	4.6	T
Number of CMS superconductor strands	40	32	
% of Short Sample	32	33	
Temperature Stability Margin	1.6	1.8	K
Total Cold Mass of Solenoid	130	220	tonne
Number of Winding Modules	2	5	
R_{min} Cryostat	2.591	2.97	m
R_{min} Coil	2.731	3.18	m
R_{max} Cryostat	3.392	3.78	m
R_{max} Coil	3.112	3.49	m
Z_{max} Cryostat	$\pm$ 3.033	$\pm$ 6.5	m
Z_{max} Coil	$\pm$ 2.793	$\pm$ 6.2	m
Operating Temperature	4.5	4.5	K
Cooling Method	Forced flow	Thermosiphon	

Eleven 20 cm thick iron plates with 4 cm gaps form both the barrel and end wall portions of the flux return. There is also a 5 cm gap between the barrel and door that is partially filled with barrel iron connecting plates. These connecting plates are also part of the solenoid axial restraint system. The door iron plates are held together with an iron cylinder on the ID and top plates on the OD.

6.2.2 Calculations

The results of two- and three-dimensional ANSYS magnetic field calculations of the magnet are shown in Figure 6.2.1. The 3D ANSYS model also includes the DID, barrel/door iron gap details, and the cryogenic chimney and current lead penetration details. The DID coil

position was provided by BNL using OPERA 3D and custom codes. The ANSYS 3D model uses an edge element formulation and has three million elements. Advances in computation give a significant advantage to SiD design as compared to prior CMS design work. The magnetic axial spring constant was found to be constant from 1 cm to 20 cm coil displacement. The axial magnetic force is maximum at full current; there is no iron saturation effect. An iron door HCAL was studied and rejected due to minimal improvement in field and field uniformity versus increased cost and complexity.

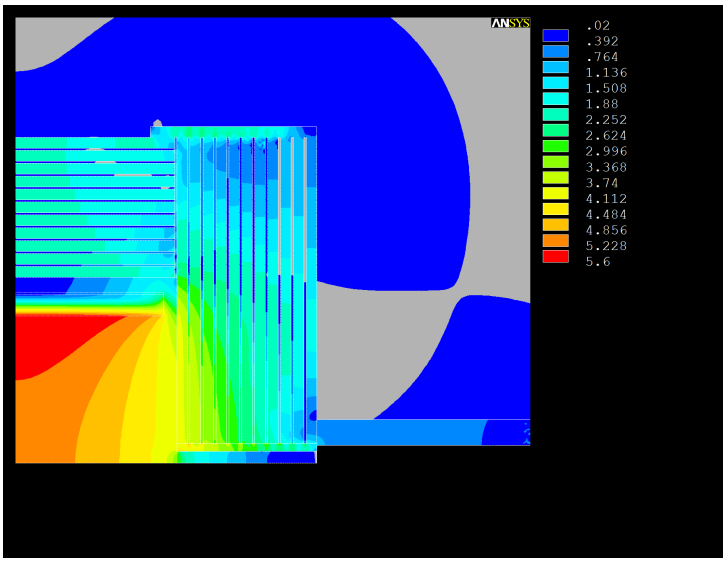

Figure 6.2.1: :2D Axisymmetric showing B_{max}. Only a small portion of the air is displayed. The gray/blue boundary is the 200 G line.

6.3 Mechanical Engineering

6.3.1 Solenoid Coil Production

The superconductor will be internally wound into two precision aluminium 5083-H321 mandrels using CMS winding procedures, including epoxy vacuum impregnation and mandrel joining techniques, and conductor splicing methods. The CMS coil winding experience will significantly reduce the SiD time and expense of winding line setup and commissioning. Coil winding and vacuum impregnation will take place at the vendors facility. The magnet will be shipped as two separate coils at 65 tonne each.

6.3.2 Integration of DID to solenoid

The Dipole Integrated Dipole/Anti-Dipole (DID) is mounted directly on top of the solenoid cooling tubes. The four separate 660 kA turn winding packages are sandwiched between a lower 3 mm Al sheet and an upper 5 mm Al sheet. Each package consists of five coils all electrically connected in series. The coil packages are mounted directly on top of the solenoid LHe cooling loops by metal screws attached to the solenoid winding mandrel. Twenty two solenoid splices rest on top of the upper DID Al sheet and are substantially supported by direct connection to the solenoid winding mandrel at the centre of the four DID winding packages. Conduction through the DID and direct physical connection through the DID centres establish cooling for the solenoid splices. All DID splices except for the two connections to the DID current leads are made in the space between the two aluminium sheets.

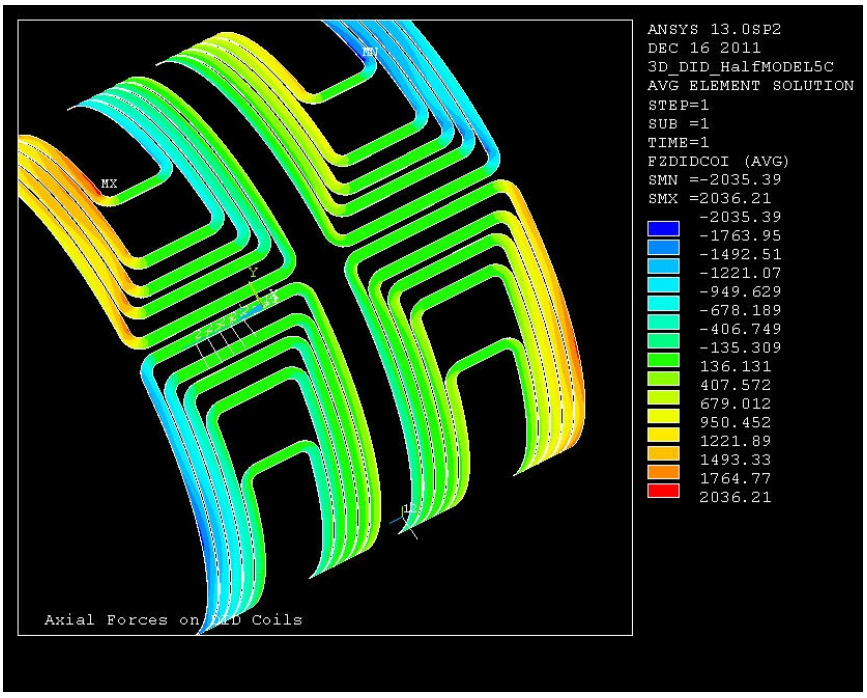

Figure 6.3.1: DID coils showing axial forces; Only half of the coils are shown

6.3.3 Thermal shield, cooling tubes, current leads and standpipe

Both the inner and outer thermal shields are directly mounted on the inner and outer vacuum shells with Ti 15-3-3-3 studs and small diameter fibreglass epoxy tubes. The shields are fixed at the midplane and contract symmetrically from both ends. The shields are made from aluminium alloy with appropriate high resistance joints to reduce eddy current forces during solenoid fast discharge. Baseline design for shield and coil cooling loops is square aluminium tubing welded to the aluminium shells with transition to round stainless steel tubing. All stainless steel or bimetallic tubing that is generally more leak tight is an option to be studied. Figure 6.3.2 is a view of the magnet major internal components.

The cryostat, ≈ 60 K thermal shield, current leads, tie rods, and instrumentation will all be designed using standard cryogenic techniques. Current leads will be very similar to the CMS current leads. Two separate iron penetrations will be used, a 70 cm $\times$ 40 cm chimney for the current leads and 36 cm diameter chimney for the cryogenic plumbing. Vacuum pump down will take place through both chimneys.

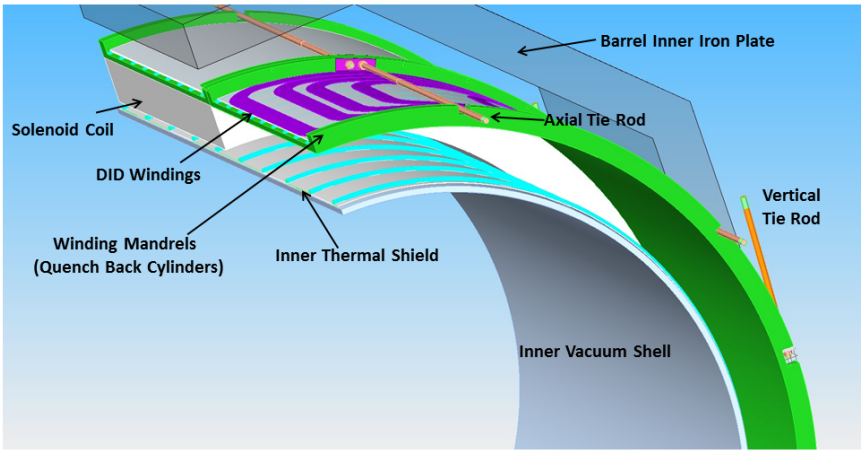

Figure 6.3.2: Magnet section showing principal elements.

6.3.4 Stress Analysis

ANSYS studies compared SiD and CMS solenoid stresses, deflections and forces. All stresses are evaluated after cool down and energisation. For this comparison the CMS conductor was used in the SiD analysis with results given in Table 6.3.1. Note that all stress and deflections are very similar for the two coils.

Table 6.3.1: Mechanical Comparison of the SiD and CMS Solenoids

QUANTITY	SiD	CMS
Von Mises Stress in High Purity Aluminium (MPa)	22.4	22
Von Mises Stress in Structural Aluminium (MPa)	165	145
Von Mises Stress in Rutherford Cable (MPa)	132	128
Maximum Radial Displacement (mm) 5.9	5	
Maximum Axial Displacement	2.9	3.5
Maximum Shear Stress on Insulation (MPa)	22.6	21
Radial Decentering Force (kN/cm)	380	80
Axial Decentering Force (kN/cm)	1830	850

Cold mass tie rods will be segmented into three different systems based on direction (axial, vertical and radial) just as they were with CMS and *BABAR*. They will be manufactured from age hardened Inconel 718. Radial and vertical loads will be carried to the cryostat outer wall. Axial loads will be carried to the cryostat end plates. In all cases, the tie rod systems are substantially stiffer than the magnetic spring constant.

6.3.5 Vacuum Shell Design

The 304 stainless steel vacuum shells will be built according to the ASME pressure vessel code design rules, but the cryostat will not be a coded vessel. Inner shell, outer shell and both end flanges are all 50 mm thick. In addition to the magnet weight and magnetic force loads, a detector weight of 450 tonnes, vacuum load and gravity self weight are imposed on the vacuum shell. Detector weight is carried by two linear rails on the inner shell. Total weight is transferred on two linear rails on the outer shell to the magnet iron. Solenoid axial decentering forces are transferred to the barrel/door spacer plates.

Linear and non-linear vacuum buckling ANSYS analysis has been completed. Primary stress results are summarised in Table 6.3.2. Local peak stresses are much higher especially for the magnetic axial decentering case. These peak stress values and maximum primary stress values can easily be reduced to ASME Section VIII Div. 2 allowables by small ad-

ditions of local reinforcing. The outer end plates will need radial rib reinforcing which is compatible with cable detector cable routing. ASME allowable stress is 138 MPa. A non-linear analysis gives a 0.62 MPa (6 atm.) vacuum buckling load.

Table 6.3.2: Cryostat vacuum shell maximal stress and deflection

LOAD	Stress (MPa)	Deflection (mm)	Location of Max Stress
Axial Magnetic	125	1.5	Axial Support Pad
Detector Mass	45	2.3	Inner Vacuum Shell
Cold Mass + Radial Magnetic	23	0.44	Vertical Tie Rod Support Pad
Vacuum	7.5	0.17	Outer Shell
Gravity on Shell	Small	0.11	Both Shells
All Loads Combined	**190**	**3.5**	**Vacuum Shell End Plate**

6.3.6 Assembly procedure

1. Coil mandrels are precision machined with welding of seamless end rings and cooling loops. Cooling loops are extensively leak checked.
2. Solenoid modules are wound with each layer in alternating direction.
3. The four DID coil modules are wound on a 3 mm thick Al sheet that is mounted to machined cylinder. Internal coil to coil splices for each of the four modules are completed. A 5 mm sheet is attached to the OD of the DID coils.
4. DID coils are vacuum impregnated. This is a higher temperature resin than the solenoid resin.
5. DID coils are mechanically attached on top of solenoid cooling loops with screws to the solenoid mandrel.
6. Solenoid modules with attached DID coils are vacuum impregnated.
7. The two mating ends of the solenoid modules are precision machined.
8. Solenoid modules are stacked vertical and joined above ground at the detector site.
9. All 24 solenoid splices are completed above the DID. All DID module to module splices are completed

10. Axial tie rods are attached to the solenoid.
11. Inner and outer thermal shields are mounted to inner and outer vacuum shells.
12. Inner and outer vacuum shells are placed on the solenoid.
13. Vertical and radial tie rods are attached to the outer vacuum shell.
14. All internal plumbing and electrical connections are completed along with mounting of the thermal shield end plates. Piping extends a short distance past the chimney opening. Solenoid lead ends and DID lead ends extend through the vacuum shell current lead opening and are wrapped in a loop.
15. Top and bottom vacuum end plates are welded.
16. All tie rods are tightened.
17. The completed magnet assembly is rotated horizontal on a shaft parallel to the ground using the overhead crane and two pulling cables.
18. The magnet is moved to the detector cavern and lowered vertically into the bottom half of the magnet iron.
19. Current lead and cryogenic chimney pipe assembly are completed and welded.

6.4 Cryogenics

A helium refrigerator/liquefier of approximately 1.5 kW of 4.5 K refrigeration is located on the detector near the top. This choice means that the liquefier high pressure helium and compressor suction return lines must be flexible for push-pull operations. The QD0 2 K vacuum pumping lines must also be flexible. The liquefier supplies both forced flow 4.5 K saturated LHe and 40 to 80 K helium for the thermal shield and support rod thermal intercepts. The liquefier is a custom built commercial product whose detailed design and construction will be carried out by industry as part of the complete cryo plant procurement. A 5000 litre LHe storage dewar is stationed next to the refrigerator liquefier and can almost be considered part of the liquefier. It serves as a pressure buffer for forced flow operation and as a LHe supply reservoir during liquefier down times. This technique was used successfully for a decade of running *BABAR*.

The detector valve box near the top of the detector is used to minimise flexible connections between detector and refrigerator. It also serves as the distribution point for supply of LHe to the two superconducting QD0 final focusing magnets 2 K cold boxes that are fixed on the detector. Figure 6.4.1 is a flow diagram of the SiD cryogenic system.

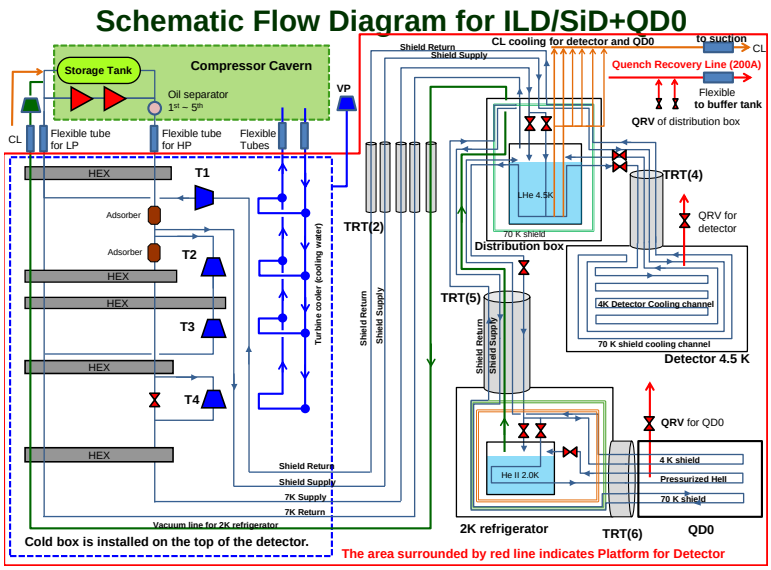

Figure 6.4.1: Cryogenic Flow Schematic

6.5 Conductor

6.5.1 Solenoid baseline conductor (CMS)

A slightly modified CMS conductor is the SiD baseline design. The CMS conductor is fabricated by ebeam welding structural aluminium to the coextruded high purity Al/superconducting cable insert. A superconductor stability margin similar to CMS will be used requiring that the Rutherford cable be increased in size from 32 to 40 strands. In comparison to CMS short sample percentage will improve from 33% to 32%, but the thermal margin will decrease from 1.8 K to 1.6 K. All magnet ANSYS finite element stress analysis to date has been with this conductor.

6.5.2 Modified CMS Conductor Choices

Many other conductor designs are possible. One possibility is replacement of the high purity aluminium with an Al-0.1%Ni alloy that is stronger but still has good conductivity. This material was used for the ATLAS Central Solenoid conductor. Coextrusion tests of this alloy are currently being pursued by CERN. Many other dilute aluminium alloys (e.g. scandium or binary elements) that form small intermetallic precipitates are possible but largely unexplored. Still other high purity reinforcement such as the standard TiB_2 grain

refiner or carbon nanotubes are possibilities. Replacement of the structural aluminium with internal stainless steel rope would simplify conductor manufacture if a different method of coextrusion such as the ConKlad process could be industrialised for this size.

ANSYS coupled transient electromagnetic and thermal diffusion model was used to evaluate conductor stability. With large size high purity aluminium stabilised superconducting conductors, current is slow to diffuse into the high purity aluminium during a temperature excursion reducing conductor stability. ANSYS results show that equivalent conductor stability is achieved when both types of CMS aluminium are replaced with a single aluminium that has one third the electrical and one third the thermal conductivity of the high purity aluminium.

6.5.3 DID conductor

The dipole coils are to be wound from a high purity aluminium and a CMS single superconducting strand co-extrusion. Two layers of 75 turns of 2.5 mm $\times$ 1.8 mm superconductor per winding are proposed. There will be 0.5 mm of fibreglass cloth between each turn and each layer. 875 A at 1/3 of $I_{critical}$ is the operating point. The stored energy for an independently powered DID is in the range of 240 kJ. When coupled to the solenoidal field, stored energy increases by $\approx$ 8 MJ. Because the stored energy is so small, the volume fraction of high purity aluminium to superconductor needed for safe energy extraction during a quench has been reduced from the CMS 12.4 to a ratio of 2.5. Forces on each of the four coils are rather large in sum but spread somewhat uniformly and manageable (4100 kN radial and 7800 kN axial).

6.6 Electrical

6.6.1 Magnet Safety

The lower stored energy and inductance of the SiD magnet compared to CMS make it easier to protect in the event of a quench. A conservative 300 V to centred tapped ground is chosen. Experimental tests and computer simulations show that the CMS quench propagation velocity around one complete turn is faster than turn to turn quench propagation through the insulation. Because we have chosen identical CMS conductor size and insulation thickness with very similar conductor electrical and thermal properties, peak temperatures will be less than the CMS 80 K with dump resistor but equal to CMS 130 K with dump breaker failure). Both SiD and CMS safety rely on the winding mandrel serving as a quench back cylinder spreading the quench on the outer layer and absorbing some of the stored energy. Fast discharge of the DID as a solenoid quench propagator to reduce winding peak temperature and

stress is reasonable. However, the detailed transient 3D ANSYS calculations remain to be done.

6.6.2 Power Supply, Dump Resistor and Dump Switch

The power supply, contactor, dump resistor dump switch are attached on the side of the detector near the top. These three components are arranged to minimise the 18 kA buswork. Power supply, DC contactor and mechanical dump switch are standard design components procured from outside vendors. The DC contactor allows for normal slow mode discharge and fast discharge. The power supply operates in only one quadrant, positive current and positive voltage. Therefore, more robust free wheeling diodes can be employed instead of thyristors as were selected for CMS which permitted voltage control ramp down. The SiD magnet does not have a current reversal switch. The dump switch is a conventional commercially purchased double pole mechanical breaker with arc chutes. Both the positive and negative legs are mechanically ganged together ensuring that they open at the same time. The breaker with controls is housed in a steel box 2.6 m $\times$ 0.9 m $\times$ 1.5 m (high). The power supply is a standard water cooled power supply design tailored to low inductance operation. Overall dimensions of this unit are 3.7 m $\times$ 1.0 m $\times$ 2.0 m (high).

A novel compact pressurised water cooled dump resistor will be used instead of a very large air cooled dump resistor such as the type used for CMS and other large superconducting magnets. An ASME coded vessel holding 3100 litre of water will rise to a conservative design value of 150 C at 0.48 MPa assuming the worse case of all 1.56 GJ deposited as sensible heat in the water of the resistor. Correct dimensioning of the stainless steel resistor element ensures that boiling heat transfer is only a third of the peak nucleate boiling flux at the metal/water interface. A 1.50 m diameter $\times$ 3.5 m tall cylindrical tank could be used. Internal connections will provide for both fast dump and normal slow dump modes. A centre tap grounding wire is attached to the electrical centre of the resistor.

Chapter 7

Engineering, Integration and the Machine Detector Interface

7.1 Introduction

The ILC Reference Design Report [67] was based on a site presumed to run ∼100 m below a topographically flat landscape. It specified the civil engineering parameters of a shared underground interaction region (IR) Hall accessed by two shafts symmetrically located around the beam line. More recently:

- A set of functional requirements for the design of the detectors and the IR was defined [68].
- The SiD and ILD detector concepts were validated.
- A platform similar to the CMS shaft plug was agreed to be the means of effecting the push-pull exchange of the detectors.
- A new cavern layout was designed featuring one shared 18 m diameter central shaft directly over the interaction point, serviced by a 4000 tonne gantry crane, separate assembly areas accessible to the sliding platform and separate garage areas for major detector component replacement, each serviced by an 8 m equipment shaft and a 5.6 m personnel elevator shaft. See Figure 7.2.1.
- The possibility has arisen that the ILC would be built in a mountainous site where the IR would be accessed by a tunnel of limited diameter of length of order 1 km.

These features are described in more detail in PB: REF TO the common section of this Detailed Baseline Document and in the ILC Technical Design Report PB:REF.

Table 7.2.1: List of SiD element masses and sizes. For each barrel component the size given is the outer diameter × length (z), and for each endcap component it is length × outer diameter.

Name	Mass (10^3 kg)	# Subcomponents	Mass (10^3 kg)	Size (m×m)
Barrel	4220			
ECAL	60	12	5.0	2.8×3.5
HCAL	367	12	31.7	5×5.9
Tracker	3	1	3	2.5×3.3
Coil	180	2	90	6.8×5.9
Magnet Yoke	3360	8	420	12×5.9
Yoke Arch Supports	150	2	75	12×1
Peripherals	40			
Each of Two Endcaps	2450			
ECAL	10	1	10	0.15×2.5
HCAL	23	1	23	1.2×2.8
Muon System	30			2.6×12
MDI Components	10			
Endcap Steel Plates	2200	11	200	0.2×12
Endcap Leg Supports	140	2	70	2.6×6
Infrastructure	37			

7.2 IR Hall Layout Requirements and SiD Assembly

The main subcomponents of SiD are its central barrel and its two endcaps. The majority of the SiD's mass results from the flux return iron. The iron will be shipped to the ILC site from an industrial production facility in the form of sub-modules suitably sized (∼100 tonne) for road transportation. The solenoid coil will likewise be wound industrially and transported in sections, probably two, amenable to transport. We expect the VXD, Tracker, ECAL, HCAL and muon system modules to be built at collaborating labs and universities and transported to the ILC site for final assembly. Table 7.2.1 lists the masses and sizes of the SiD elements that determine the crane capacity and shaft size for installation.

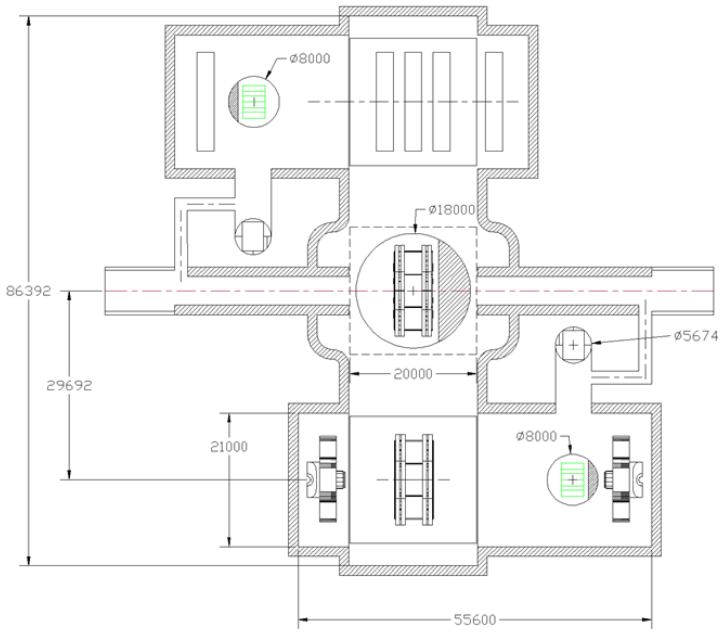

Figure 7.2.1: Layout of the IR Hall for vertical access, showing installation shafts and push-pull platforms.

7.2.1 Vertical Access (Europe and Americas sites)

Figure 7.2.1 shows the layout of the IR Hall. This allows the 3 m thick SiD push-pull platform to be positioned directly under the gantry crane. The service caverns allow for storage of the endcaps and unimpeded access to the barrel region for the initial installation or replacement of detector subcomponents. Access to the service caverns is through an 8 m diameter shaft serviced by a 40 tonne crane.

The vertical access assembly presumes that the SiD magnet, comprising the superconducting coil, iron barrel yoke and iron endcap doors, will be pre-assembled and tested in an assembly hall above ground. Any detector subcomponents, notably the HCAL and ECAL, that are ready in time can be installed and tested above ground. Then SiD's three main subcomponents, the majority of the barrel and the two endcaps, will each be lowered as units onto the platform below.

The basic requirements for the assembly hall above ground are:

- A devoted crane with a minimum of 215 tonne main hook capacity, set by the largest subcomponent weight. The ILD and SiD cranes should roll on the same bridgework

so that they can be used in tandem if the need arises.

- A steel reinforced concrete platform, upon which SiD will be assembled, which is structurally robust when supported on three sides as it slides over the 18 m diameter main access shaft to deliver the SiD barrel and doors to the gantry crane.

- A c. 4000 tonne capacity gantry that can lower the roughly 15 m $\times$ 5 m $\times$ 6 m 3500 tonne instrumented SiD Barrel and the two 11 m $\times$ 14 m $\times$ 6 m 2500 tonne endcaps onto the push-pull platform in the IR Hall.

It is foreseen that the surface assembly hall is aligned with its long axis parallel with the beam line. The construction platform will move in this direction as well. Its width is 20 m, approximately the width of the building, while the length will be large enough to comfortably house the barrel and the doors when open. The platform surface will be at floor grade and thus run in a track. The doors will move across the platform-floor junction on the rollers when required to mate with the barrel. The SiD barrel, once lowered, will remain stationary on its platform. The endcaps, which must be routinely opened to service the detector, will move on a system of rollers guided by hardened rails. The current plan is to lower the doors first and to put them in their service caverns to await mating with the barrel. Once the barrel and endcaps have been lowered the main shaft and gantry crane are no longer needed.

The above-ground assembly sequence for a vertical access site can also be used for a horizontal access subterranean site. In the latter case the individual subcomponents are separately transported through an access tunnel of limited diameter to the IR Hall, where a 215 tonne bridge crane suffices for installation. In either case a plausible assembly sequence is:

- Assemble the two endcap leg supports on top of the platform.

- Transport each of the eleven 200 tonne endcap plates in three industrially manufactured segments to the crane and assemble into 11 m x 11 m octagonal plates. Mount each on the support legs and make plate to plate connections.

- Install muon chambers from the sides into each gap, and the endcap HCAL and ECAL to the innermost face.

- Assemble detector mounted PACMAN shielding on the endcaps.

- Once endcaps are completed move them to their alcoves.

- Assemble lower halves of barrel arch supports.

- Assemble industrially manufactured ∼100 tonne barrel steel stacked plate segments into sixteen ∼210 tonne half-wedges and use the crane to assemble the five lower barrel wedges, forming a cradle open at the top.
- Assemble the solenoid coil segments and DID coils into their cryostat and test at low current. Lift coil with fixture and thread into the cradle.
- Finish the remaining three barrel wedges, install muon system and finish with shear plates at each wedge-to-wedge junction.
- Thread solenoid with an assembly beam and mount the HCAL assembly spider onto it. Load each of the twelve 32 tonne HCAL wedges onto the spider and push into barrel on rollers.
- Repeat HCAL sequence with the much lighter ECAL.
- Thread in Tracker and VXD units when available.

The QD0 assembly (QD0, masks, FCAL) will need to be installed below ground. The platform will transport the doors to the alcove area, whence the assembly will be loaded from the rear.

7.2.2 Horizontal Access (Japan sites)

The barrel and endcap installation procedures outlined above are directly applicable. One need only plan for the lengthier procedure of loading the heavy sub-elements onto the tunnel transport carts and their delivery to the IR Hall assembly area.

The Japan site design specifies an 11 m diameter tunnel, which is sufficient to transport the largest element of SiD, its solenoid. Figure 7.2.2 shows the SiD solenoid being transported around the final right-angle bend to the IR Hall where it is lifted by the 215 tonne crane and placed in the cradle formed by the lower elements of the SiD barrel yoke. Clearly, if the ILC schedule permits below-ground assembly of the detectors for the vertical access site, the diameter of the access shaft could be reduced from 18 m to 11 m.

7.2.3 Detector Access for Repairs

The upper part of Figure 7.2.3 shows SiD with one of its endcaps opened by 2 m, sufficient to expose the FCAL region and the Tracker. This is the basic configuration for quick repair opportunities that may occur while SiD is on the beamline. In the lower part of Figure 7.2.3 the endcap has been opened by 2.8 m, the maximum possible for SiD without having to disconnect the QD0 cryostat. In this figure, the Tracker has been slid to one side to expose

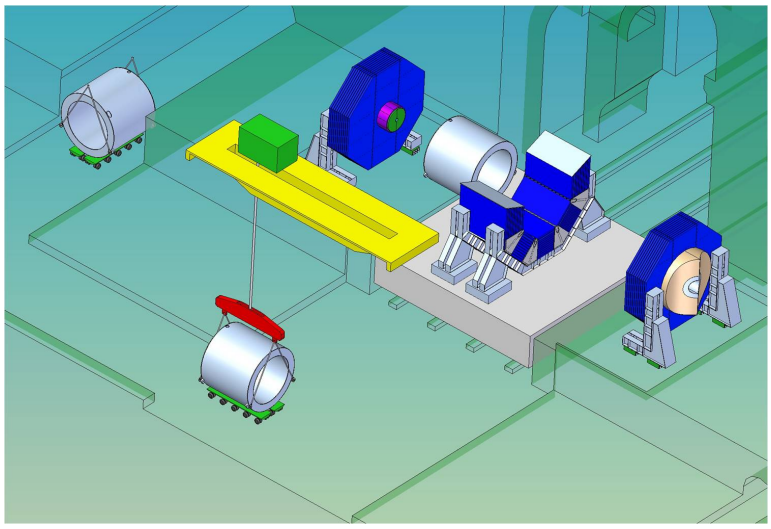

Figure 7.2.2: Transporting the largest detector element, the SiD Solenoid, through the 11 m diameter access tunnel to the assembly area where the 215 tonne crane can lift it and place it within the SiD barrel.

the VXD, a manoeuvre that would require the use of some portion of the tracker installation tooling. As such, it would probably be scheduled for a time when SiD is off the beamline. Repairs more major than replacement of a VXD module, such as replacement of the Tracker, barrel ECAL or barrel HCAL, will take place off the beamline.

7.3 Detector Exchange Via a Sliding Platform

7.3.1 Introduction

Among the challenges to be addressed in the push-pull operation are the reproducibility of tight alignment to the beam at the ± 1 mm level; the time requested to complete the swap cycle must be as low as reasonably achievable since it will be reduce the integrated luminosity; umbilicals are needed to keep the detector connected to the DAQ and services such cryogenics.

7.3.2 Platform

These requirements have been addressed by developing the concept of a reinforced concrete platform 20 $\times$ 20 m^2 in area and 3.8 m tall, with a total mass of $\sim$4500 tonne. To

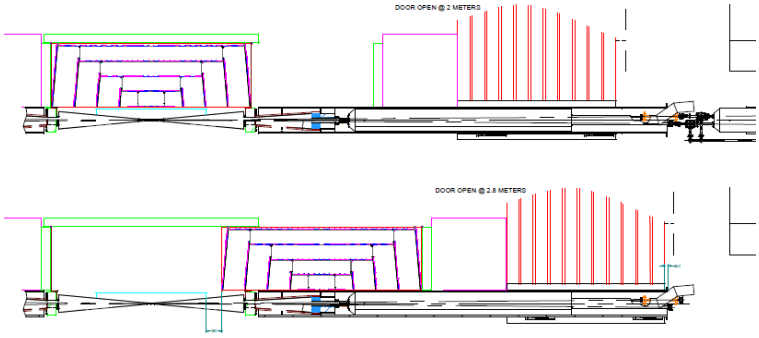

Figure 7.2.3: Upper: SiD with one of its endcap doors opened by 2 m, sufficient to expose the FCAL region and the Silicon Tracker. Lower: the door has been opened by the maximum 2.8 m and the tracker has been slid to one side to expose the VXD for repair or replacement.

compensate for their different heights the SiD platform is thicker than that of ILD. Assuming the total SiD mass to be 9000 tonne, preliminary calculations have shown [69] that the maximum static deformation achievable is less than 1mm at the locations where the detector is supported by the platform. The construction will be very similar to the concrete slab designed for the CMS detector [70].

The movement system is designed for a total mass of detector and platform of $\sim$14,000 tonne. Two options are under consideration, air pads and Hillman rollers, each with hydraulic jacks above. For the air pads the expected friction is 1% and the total force required for the horizontal motion is 140 tonne. Assuming a maximum load capacity of 350 tonne for a single air pad, SiD will require the installation of 40 units under the platform. For the rollers the friction will be $\sim$3% and the force required for the horizontal motion will be $\sim$420 tonne, while only 14 units with 1000 tonne load capacity will be required. In both cases, the floor will need to be hardened with steel to prevent wear that would spoil the alignment performance. A reliable linear guiding system built in the floor is also essential for air pads as well as for rollers. The force required in both cases for the horizontal motion can be comfortably provided by a set of hydraulic climbing jacks. Another set of hydraulic jacks will be placed at the beamline location of the platform to correct the final transverse alignment, if needed.

7.3.3 Vibration analysis and Luminosity Preservation

A structural dynamic model of the QD0 supported from SiD, including the platform, has been developed to calculate the free modes as well as the transfer function between the

ground and the doublet. Using different ground vibration models available in the literature, that correspond to different accelerator sites, a maximum r.m.s. displacement of 20 nm has been calculated, more than a factor two below the maximum allowed. A campaign of experimental measurements of vibrations has been carried out to validate some key features of the model: the simulation of the reinforced concrete platform and correlation measurements between distant locations in the detector hall of CMS at CERN and SLD at SLAC. The reinforced concrete slab of CMS has been instrumented with geophones in various locations and the data have been used to benchmark a finite element model of the platform [71]. Good agreement between experimental data and simulation has been found with an internal damping ratio of 6.5%, somewhat higher than the values recommended for similar materials. The difference can be explained by the soil deformation and the presence of wheels, both of which were not included in the model. The measurements done at CMS and SLD have shown a good correlation at low frequencies between points at the two extreme sides of the cavern, i.e. the location of the final focus system [72].

7.3.4 Push Pull Detector Exchange Process and Time Estimate

The sequence of push-pull operations should allow a fast detector interchange to minimise loss of beamtime; realistically it should not take more than a few days. Defining as $t = 0$ the time when the beams have been dumped and the interlocks are released to allow the access of the technical personnel, the key steps are the opening of the PACMAN shielding, the breaking of the vacuum between the QD0 and the QF1, a reasonably fast horizontal movement from the IP to the garage position with an easy and reliable alignment system. The cryogenic system will stay on during the push-pull, with the umbilical able to accommodate the $\sim$30 m movement requested. Figure 7.3.1 summarises the sequence of steps and the minimum required time for the push-pull operation.

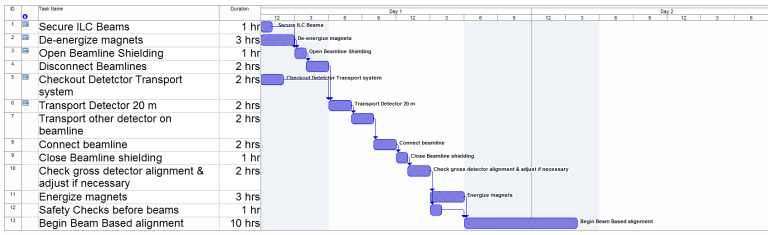

Figure 7.3.1: Summary chart of push-pull operational steps.

7.4 Beampipe and Forward Region Design

7.4.1 Introduction to the Near Beamline Design

The SiD near-beamline design minimises the radial space required for the support and alignment of the final quadrupole lens QD0 to limit any loss of tracking and calorimeter acceptance. In the SiD design the silicon tracker slides over the QD0 support to expose the vertex detector for servicing (see Figure 7.2.3).

7.4.2 Beampipe

The beampipe through the central portion of the vertex detector has been taken to be all-beryllium. Within the barrel region of the vertex detector, the beryllium beampipe forms a straight cylinder with inner radius of 1.2 cm and a wall thickness of 0.04 cm. At z = $\pm$6.25 cm, a transition is made to a conical beampipe with a wall thickness of 0.07 cm. The half angle of the cone is 3.266°. Transitions from beryllium to stainless steel are made beyond the tracking volume, at approximately z = $\pm$20.5 cm. The initial stainless steel wall thickness is 0.107 cm; it increases to 0.15 cm at approximately z = $\pm$120 cm. The half angle of the stainless steel cone is 5.329°. The inner profile of the beampipe is dictated by the need to avoid the envelope of e^+e^- pairs from beamstrahlung.

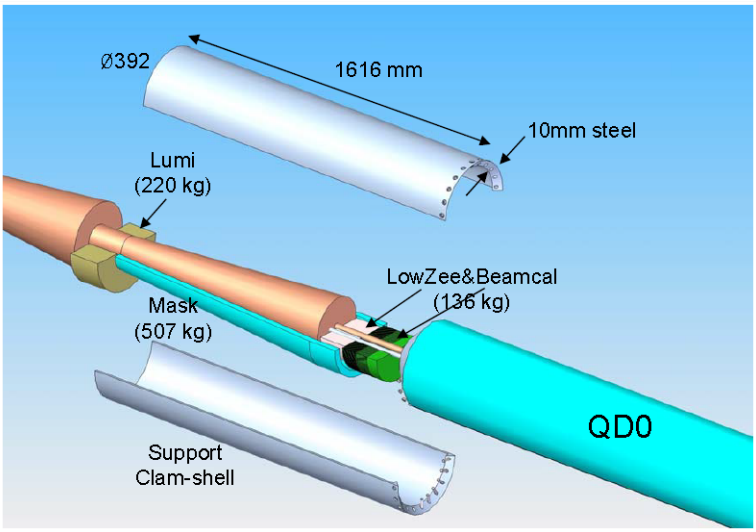

Figure 7.4.1: Detail of the LumiCal, mask and BeamCal which must be supported by the QD0 support tube and alignment system.

7.4.3 LumiCal, BeamCal, Mask and QD0 Support and Alignment

The QD0 support tube (Figure 7.4.1) is extended toward the IP to support the 220 kg LumiCal, the 507 kg 3 cm thick conical tungsten mask, the lightweight 13 cm thick 25 cm diameter borated polyethylene neutron absorber and the 136 kg BeamCal. The low-z end of the support tube will be split along its centreline so that it can be opened to install the mask, absorber and BeamCal. The LumiCal will be bolted to the front end of the tube and be positioned so that it hangs 10 cm in front of the endcap ECAL when the detector is closed. While this choice complicates the vertex detector support system, it minimises any loss of acceptance between the LumiCal and the ECAL endcap. The loading of the support tube results in a deflection of 100 µm when the door is closed, growing to 2.2 mm when the door is opened the nominal 2 m required to service the detector when on beamline, and 6 mm when the door is opened the maximum 2.8 mm allowed by the location of QF1 and the obstruction of the cryo-transfer line joining QD0 to its local 2 K refrigerator. A wedge mover system will need to act in conjunction with the door opening mechanism to keep the front end of the LumiCal fixed in space.

The beampipe through BeamCal terminates in a commercial flange. The conversion of the common beampipe to separate incoming and outgoing beampipe takes place in the 215 mm space between the back of BeamCal and the front face of the QD0 cryostat at 3.283 m from the IP and is illustrated in Figure 7.4.2.

%endfigure

7.4.4 Vacuum System and Performance

The vacuum requirements for the final focus and interaction region lengths of the beampipe have been specified [73] as 10 nTorr from 200-800 m from the IP, 1 nTorr in the region from 200 m up to the QD0 quadrupole and ”much looser” than 1 nTorr between the QD0 cryostats. The region between QD0 and QF1 is evacuated to $<$ 10 nTorr by the pumping action of the two cryostats and the 100 l/s ion pump on each beam line in front of QF1 Achieving 1 nTorr upbeam of QF1 will be a challenge. With a 20 mm diameter stainless beampipe and 50 l/s ion pumps every 2 m, the average pressure is 23 nTorr. Likely, either distributed pumping (antechamber, pumpscreens or NEG coatings) and/or larger diameter beampipes with bakeout facilities will be required to meet the 1 nTorr tolerance.

7.4.5 Feedback and BPMs

The intratrain feedback system is based on that described in the RDR [67]. A prototype system has been developed and tested with beam at ATF [74]. The parameters of the BPM and kicker required for ILC have been specified [75]. By combining a ground motion model

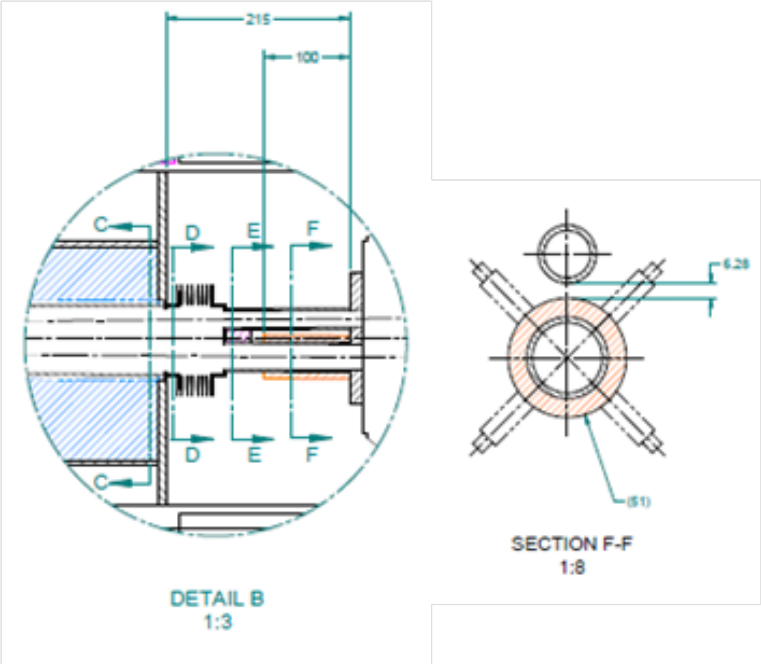

Figure 7.4.2: The BPM region between BeamCal and QD0.

with a set of transfer functions describing the vibrational effect of the magnet support system, in this case the SiD platform and detector, the reduction of luminosity loss can be studied [76, 77].

The left side of Figure 7.4.3 shows the fractional loss of nominal luminosity as a function of the rms jitter of the opposing SD0/QD0 magnet systems when they are supported from SiD and the SF1/QF1 magnets are, like all the other magnets in the final focus, assumed to be rigidly attached to the ground. The feedback system limits the luminosity loss to 2% (4%) of the nominal value for rms motions up to 50 nm (200 nm), ∼10 (∼40) times the vertical spot size of beam at the IP. The right side of Figure 7.4.3 shows the contribution of mechanical jitter to the total jitter in the case where the ground motion model is that of the noisiest site studied (DESY near Hamburg). Even in this extreme case, the feedback system would limit luminosity loss to 2% with up to 17 nm of additional mechanical jitter, coming from, for example, vibrations induced by the liquefier or flow of liquid helium. A modelling program to ensure that the ground to magnet transfer function is correct is ongoing [78].

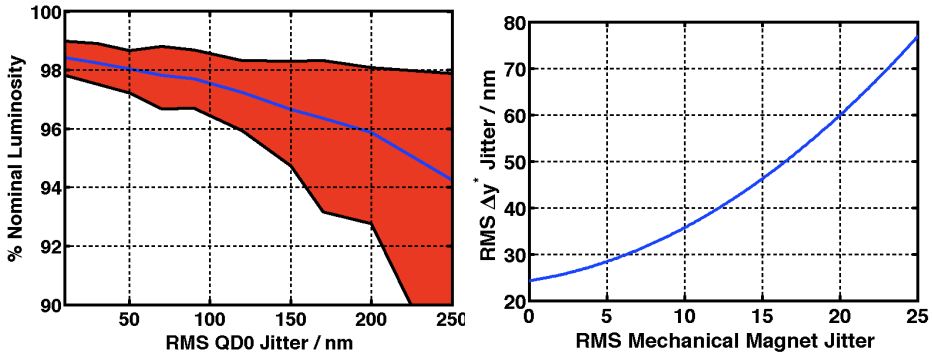

Figure 7.4.3: The fractional loss of nominal luminosity as a function of the rms x and y vibration of the SF1/QF1 and SD0/QD0 magnet systems (left). Contribution of mechanical jitter to overall vibration budget (right)

7.4.6 Frequency Scanning Interferometric (FSI) Alignment of QD0 and QF1

The FSI system incorporates multiple interferometers fed by optical fibres from the same laser sources, where the laser frequency is scanned and fringes counted, to obtain a set of absolute lengths [79, 80, 81]. To monitor the position of the QD0 cryostat to the required accuracy [68] of 50 µm in x, y, and 20 μrad in roll, pitch and yaw a network of "optical trusses" between beam launchers at known positions and reflectors placed on the QD0 cryostat is needed. Simulations [82], conservatively assuming 500 µm length accuracy, indicate that a network of four beam launchers placed on the front face of the QF1 cryostat, each of which sends a split beam to two of four similarly situated reflectors on the back end of the QD0 cryostat, and a similar network tying the inner edge of the innermost HCAL endcap to the front end of the QD0 cryostat, can achieve an precision of $\sim$1 µm in x and y and $\sim$1 μrad in all axis rotations. Schemes that can tie this network across the IP are important to develop.

Chapter 8

Forward Systems

8.1 Forward Detector

The forward region is defined as polar angles $|\cos\theta| > 0.99$ ($\theta < 140$ mrad), which is the angular region forward of the coverage of the SiD Endcap ECAL. The angular coverage is completed by two detectors, the Luminosity Calorimeter (LumiCal) and the Beam Calorimeter (BeamCal). As discussed in more detail below, the LumiCal is an annular calorimeter located approximately 1.6 m from the interaction point (IP), subtending angles between 40 mrad and 90 mrad. The BeamCal, the most forward of all the SiD subsystems, lies at a distance of approximately 2.8 m from the IP, subtending angles between 3 mrad and 40 mrad.

The instrumentation goals in this region are:

- Measurement of the integrated luminosity using small-angle Bhabha scattering (LumiCal) to an accuracy better than 10^{-3};
- Precise determination of the luminosity spectrum by measuring the acolinearity angle of Bhabha scattering (LumiCal);
- Extension of the calorimeter hermeticity into the small angles for physics searches (LumiCal and BeamCal);
- Instantaneous luminosity measurement using beamstrahlung pairs (BeamCal);
- Provide a two-photon veto for new particle searches (BeamCal).

The detector challenges include good energy resolution, radiation hardness, interfacing with the final focus elements, high occupancy rate requiring special readout, and performing the

physics measurements in the presence of the very high background in the forward direction (see Chapter 11.5.1).

8.1.1 Design criteria

LumiCal Physics Requirements

The number of Bhabha events per bunch crossing for a detector with minimum and maximum polar angle coverage θ_{min} and θ_{max} (in mrad) is:

$$N = 0.5\text{pb}\frac{\text{L}}{\text{R}}\int_{\theta_{\text{min}}}^{\theta_{\text{max}}}\frac{\text{dcos}\theta}{\sin^4\theta/2} \sim 6\times10^{-6}\left(\frac{1}{\theta^2_{\text{min}}}-\frac{1}{\theta^2_{\text{max}}}\right)$$

for $\sqrt{s}$ =0.5 TeV, L=$2\times10^{34}\text{cm}^{-2}\text{s}^{-1}$, and bunch crossing rate R=$1.4\times10^4\text{s}^{-1}$. Our goal is to measure the luminosity normalisation with an accuracy of several 10^{-4} for $\sqrt{s}$ =0.5 TeV. To do this one needs $\approx 10^8$ events collected over $\approx 10^7$ s, or about ten events per second. One can then calculate the absolute luminosity with $\approx 10\%$ statistical error every several minutes during the run. With a bunch crossing rate of $1.4\times10^4\text{s}^{-1}$, we need $> 10^{-3}$ events per bunch crossing. To achieve this statistical accuracy, we start the fiducial region for the precision luminosity measurement well away from the beamstrahlung pair edge at θ=20 mrad, with a fiducial region beginning at θ_{min}=46 mrad, which gives $\approx 2\times10^{-3}$ events per bunch crossing.

Luminosity precision and detector alignment

Since the Bhabha cross section is $\sigma \sim 1/\theta^3$, the luminosity precision can be expressed as

$$\frac{\Delta L}{L} = \frac{2\Delta\theta}{\theta_{min}},$$

where $\Delta\theta$ is a systematic error (bias) in polar angle measurement and $\theta_{min} = 46$ mrad is the minimum polar angle of the fiducial region. Because of the steep angular dependence, the precision of the minimum polar angle measurement determines the luminosity precision. To reach the luminosity precision goal of 10^{-3}, the polar angle must be measured with a precision $\Delta\theta < 0.02$ mrad and the radial positions of the sensors must be controlled within 30 µm relative to the IP.

Monitoring the Instantaneous Luminosity with BeamCal

The colliding electron and positron bunches at the ILC generate large Lorentz forces, which cause radiation of gammas called beamstrahlung. Under the ILC Nominal beam parameters at $\sqrt{s}$ = 0.5 TeV, approximately 75k of the beamstrahlung photons convert into e^+e^- pairs. Since the number of pairs is directly proportional to the beam overlap, the instantaneous luminosity can be monitored to ≈10% per beam crossing by detecting pairs in the BeamCal.

Dynamic range and MIP sensitivity

While minimum ionising particles (MIP) deposit 93 keV in a 320 μm-thick Si layer, a 250 GeV electron can deposit up to 160 MeV or 1700 MIP equivalents in a single cell near shower maximum. If we want a 100% MIP sensitivity, the S/N ratio for MIP should be greater than 10, and the dynamic range of the electronics needs to be at least 17,000. This dynamic range can be achieved by using a 10-bit ADC with two gain settings.

Radiation hardness

The beamstrahlung pairs will hit the BeamCal, depositing 10 TeV of energy every bunch crossing. Sensor electronics could be damaged by the energy deposition, and sensor displacement damage could be caused by the resulting neutrons. The radiation dose varies significantly with radius, and a maximum dose of up to 100 MRad/year is expected near the beampipe. The main source of neutrons is from secondary photons in the energy range 5-30 MeV, which excite the giant nuclear dipole resonance, with subsequent de-excitation via the evaporation of neutrons. The neutron flux is approximately $5 \times 10^{13}\mathrm{n/cm^2}$ per year.

8.1.2 Baseline Design

The layout of the forward region is illustrated in Figure 8.1.1. The LumiCal covers the polar angles from 40 mrad to 90 mrad, and the BeamCal from 3 mrad to 40 mrad.

The LumiCal consists of two cylindrical C-shaped modules surrounding the beampipe. The inner radius is 6 cm centred on the outgoing beam line with a horizontal offset of Δx = 1.1 cm (158 cm × 0.007). The inner radius is dictated by the requirement that no detector intercepts the intense beamstrahlung pairs, which are confined within 4 cm radius by the 5 Tesla solenoid field. The longitudinal structure follows the ECAL design, consisting of 30 alternating layers of tungsten and silicon. The first 20 layers of tungsten each have a thickness equivalent to 2.5 mm (or 5/7 radiation length) of pure tungsten. The last 10 layers have twice this thickness, making a total depth of about 29 radiation length. The sensor is segmented with a $R-\phi$ geometry; a fine radial segmentation with 2.5 mm pitch is used to

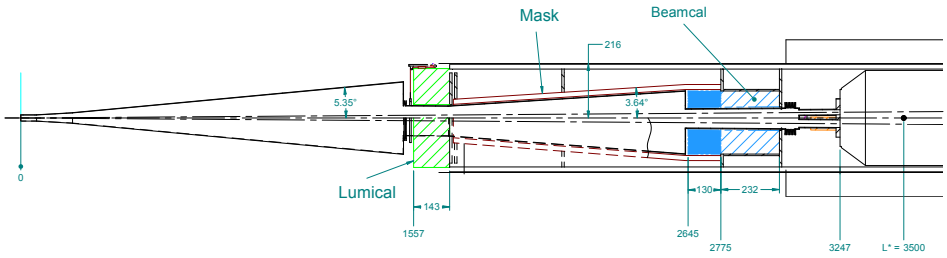

Figure 8.1.1: The SiD forward region.

reach the luminosity precision goal of 10^{-3}. The azimuthal division is 36 with each sensor covering 10 degrees. Table 8.1.1 summarises the LumiCal parameters as well as those for the BeamCal, the description of which follows.

Table 8.1.1: Forward Calorimeter Parameters

Parameter	LumiCal	BeamCal
z Extent	155.7 – 170.0 cm	277.5 – 300.7 cm
Inner radius	6.0 cm	2.0 cm
Outer Radius	20.0 cm	13.5 cm
Instrumented	42 – 110 mrad	5 – 45 mrad
Fiducial	46 – 86 mrad	—
Tungsten thickness	2.5/5.0 mm (20/10 layers)	2.5 mm
Sensor thickness	320 µm	320 µm
Radial division	2.5 mm	5.0 mm (2.5 mm $R > 7.5$ cm)
Azimuthal division	36 segments	5.0 mm

The BeamCal consists of two cylindrical C-shaped modules split in half horizontally to accommodate the incoming and outgoing beam lines. The inner radius is 2 cm, centred on the outgoing beam line, and the outer radius is 13.5 cm. A second hole, of radius approximately 1 cm and displaced from the centre by approximately 5 cm, allows for the incoming beam line. The longitudinal structure consists of 50 alternating layers of tungsten and silicon. The tungsten thickness is 2.5 mm, making a total depth of 36 radiation lengths. The inner region, at a radius of $R < 7.5$ cm, has a high signal rate from beamstrahlung pairs. The segmentation in this region is approximately 5mm $\times$ 5mm, which is roughly one half of the Molière radius. This segmentation is optimised so that tell-tale electrons or positrons from

Table 8.1.2: BeamCal instrumentation ASIC specifications summary. Note that these prototype chip specifications are based on a now-outdated version of machine parameters; the next prototype will address the change.

Input rate	3.25 MHz during 0.87 ms, repeated every 200 ms
Channels per ASIC	32
Occupancy	100%
Resolution	10 bits for individual channels, 8 bits for fast feedback
Modes of operation	Standard data taking (SDT), Detector Calibration (DCal)
Input signals	37 pC in SDT, 0.74 pC in DCal
Input capacitance	40 pF (20-pF detectors and 20-pF wires)
Additional feature	Low-latency (1 µs) output
Additional feature	Internal pulser for electronics calibration
Radiation tolerance	1 Mrad (SiO_2) total ionising dose
Power consumption	2.19 mW per channel
Total ASIC count	2,836

two-photon processes can be detected in the high beamstrahlung pair background. The outer region $R > 7.5$ cm is treated as a "far LumiCal" and has the same geometrical segmentation as the LumiCal.

Currently two electronic readout chips are being developed. The KPiX chip with 1024 channels is designed primarily for the ECAL. The chip has four hits per bunch train to be stored for each channel. The FCAL chip with 64 channels is designed to handle the 100% occupancy in the BeamCal. The chip has 2820 buffer space so that a complete bunch train can be stored. Although the LumiCal occupancy is not 100%, the LumiCal region smaller than about 10 cm will have more than four hits per bunch train. Therefore, the LumiCal is foreseen to use the FCAL chip in the inner region and the KPiX chip in the outer region.

8.1.3 Forward Systems Development Work

In this section we present the recent developments on the forward systems that have been carried out in the framework of the SiD collaboration. These developments are a component of the overall R&D effort for linear collider forward systems.

FCAL Electronics Development

The initial set of specifications for the BeamCal instrumentation ASIC is listed in Table 8.1.2.

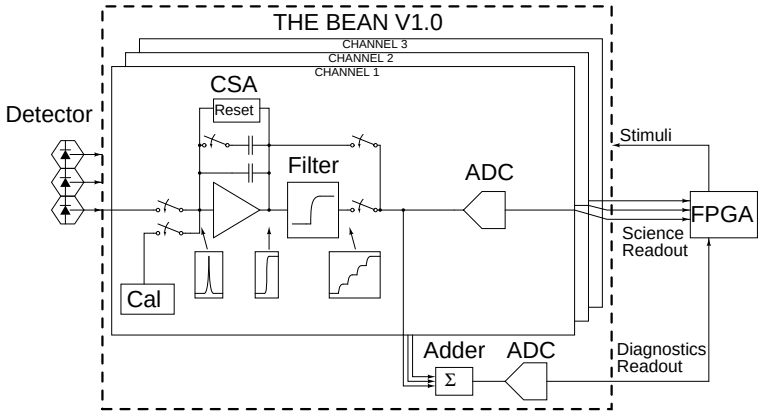

Figure 8.1.2: The simplified block diagram of the Bean ASIC.

The Bean (BeamCal Instrumentation IC) prototype is a custom IC designed in a 180-nm CMOS process as a proof-of-concept to fulfil the BeamCal instrumentation specifications. The Bean block diagram, shown in Figure 8.1.2, depicts the three channels of the prototype ASIC, as well as the adder that combines the outputs of all channels to provide a fast feedback signal. Each channel has a dual-gain charge amplifier, a precharger and calibration circuit, a filter, connecting buffers, and a dedicated analog-to-digital converter (ADC). The filter is only necessary in the calibration mode of operation (DCal mode), since in the standard data taking mode (SDT) the charge amplifier bandwidth is sufficient for filtering purposes. Future revisions of the Bean will be designed for a new set of machine specifications and will include additional channels, improved features, and a digital memory array.

Circuit description

The charge amplifier was designed around a single-ended folded cascode amplifier with capacitive feedback. The feedback network has two selectable capacitors to implement the two gains for the SDT and DCal modes of operation. The feedback network also has a reset transistor that discharges the feedback capacitance in order to reset the charge amplifier between pulses, and a slow reset-release circuit that opens the reset transistor gradually in order to reduce the noise due to split doublets.

The charge amplifier and a dummy baseline generator are connected to the fully-differential ADC when in SDT mode, or to the fully-differential filter when in DCal mode, through level-shifting buffers. The filter is a switched-capacitor integrator that effectively reduces series noise by averaging eight samples of the charge amplifier output in the analog domain.

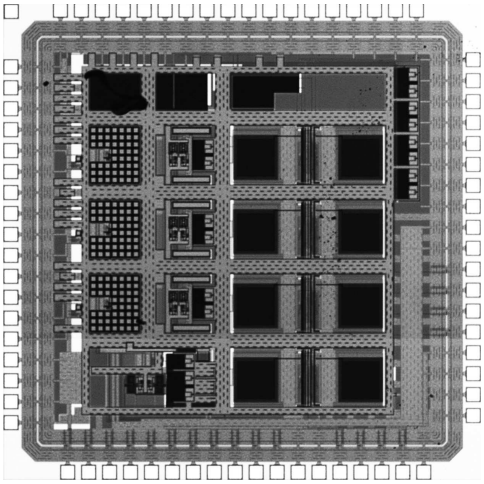

Figure 8.1.3: The Bean microphotograph.

In order to provide the low-latency output[1] that combines the outputs of all channels in the chip, an analog adder is used. The adder operates in the sampled-data domain using switched capacitors, and can be easily scaled to include more channels. Both the signal and the adder output are digitised using a custom 10-bit successive approximation register (SAR) ADC. The converter samples the differential input voltage and, using an internal digital-to-analog converter (DAC), produces a voltage that tries to match the input voltage. Using a binary search algorithm for the internal DAC output voltage, on each conversion step the ADC produces the next significant bit of the digital output, starting from the most significant bit. The full conversion takes less than 250 ns to complete.

The Bean die (Figure 8.1.3) measures 2.4 mm $\times$ 2.4 mm. The channel pitch is 360 µm and includes generous power buses; four 1.8-V power supplies are required by the chip.

Test results

The Bean ASIC was tested for linearity, crosstalk gain, adder operation and gain, bandwidth, weighting function, and noise. The chip linearity meets the specifications, with less than 1% nonlinearity mainly due to the charge amplifier finite open-loop gain. The ADC nonlinearity contribution is negligible, except for a few missing codes due to the inductance in the reference lines. This problem will be fixed in future revisions of the chip. Figure 8.1.4 shows the channel integral nonlinearity (INL) and differential nonlinearity (DNL) for the SDT mode.

[1] The low-latency output will be used for beam tuning and diagnostics.

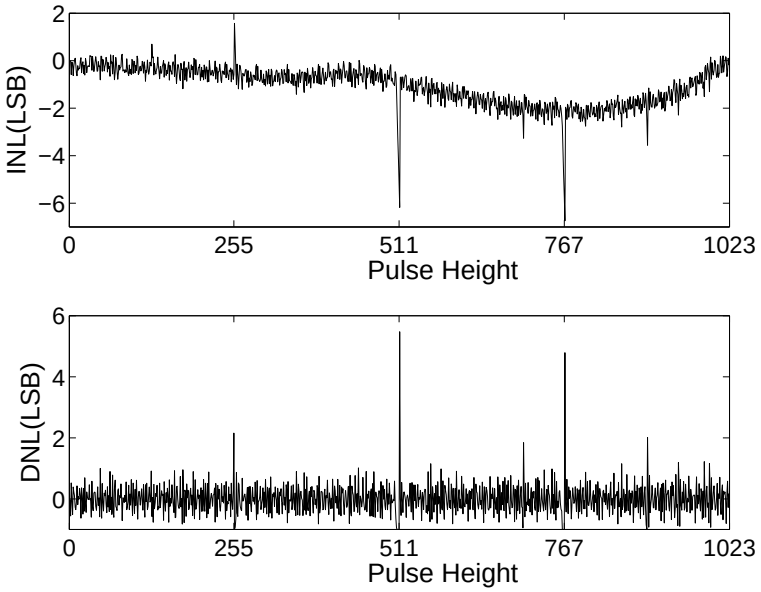

Figure 8.1.4: The Bean integrated (INL) and differential (DNL) non-linearity in the standard data-taking (SDT) mode.

The crosstalk, for either mode of operation, was measured to be less than 1.7%, and it is mostly due to indirect channel-to-channel coupling. The gain from each channel to the adder output was measured. Since there are three channels, the gain from each channel should be 0.33. The measured gains range from 0.329 to 0.345, well within the expectations. The adder digital output is available in less than 1 µs from the pulse injection at the chip input. This low latency in providing the chip output is compatible with the fast feedback requirement specifications.

A 'chip bandwidth' test was performed to quantify the residual effect of an input pulse at the output measured in subsequent cycles. If the residual effect on subsequent cycles is null, then the chip can operate at the maximum speed without piling up data from different cycles. The bandwidth measurement was done by injecting a large input at a certain cycle, and measuring the output for that cycle and subsequent cycles. The test results show no evidence of memory effect in either mode of operation, which allows to operate the chip for 100% occupancy.

From the chip weighting function and from the amplifier input-referred noise power spectral density and the detector leakage current, it is possible to compute the chip signal-to-noise ratio. The weighting functions were obtained through SPICE simulations, and then

measured using the test setup described earlier. The measured weighting functions match the expectations, supporting the use of switched-capacitor filters.

The chip noise was measured in LSB units by using the histogram method. The capacitance at the chip input, mostly due to the test PCB, is higher than the expected input capacitance from the specifications, and consequently the noise measured is higher. In order to obtain fair measurements, noise was then estimated from the measured noise, scaling it down according to the ratio between actual and specified input capacitance. The noise estimation is 0.6 LSB in the SDT mode, and 1.41 LSB in the DCal mode. Most of the noise in the DCal mode is due to a design flaw in the filter amplifier, and will be fixed in future revisions of the chip.

Electromagnetic Radiation Damage Studies

The expected integrated dose of 100 MRad per year of electromagnetically-induced radiation poses a challenge to the design of the BeamCal. Standard n-bulk silicon diode sensors are not thought to be capable of withstanding such a dose without degrading to unacceptable levels of charge collection efficiency.

Prior studies [83] suggest substantially greater electromagnetic radiation tolerance for p-bulk sensors. However, particularly for p-type sensors for which damage from electromagnetic irradiation may be minimised, damage may be dominated by the hadronic component of the electromagnetic shower. Thus, a radiation-damage study of various silicon-sensor technologies is getting underway. This study will explore the charge-collection efficiency of both n- and p-type float-zone and magnetic Czochralski sensors exposed to electromagnetic showers radiation as well as that from a beam of pure electromagnetic particles, so that the two potential sources of radiation damage can be separated. GEANT4 simulations suggest a shower-maximum exposure rate of

$$1\ \text{MRad} \simeq \frac{0.8}{I_{beam}(\text{nA}) \cdot E_{beam}(\text{GeV})} \text{hours}$$

Even for a low-intensity beam, such as that of the SLAC ESTB testbeam facility, a four-hour run will expose a sample sensor to 100 MRad. An initial campaign of electromagnetic radiation damage studies is proposed for early 2013; if successful, the setup will be offered as a facility for the study of radiation hardness for other sensor technologies provided by the FCAL collaboration.

Chapter 9

Electronics and DAQ

SiD has a coherent approach to its electronics architecture that is intended to satisfy all the subsystems requirements. It is closely tied to the unique ILC timing structure with a long bunch train with 1 ms duration and then a period of 199 ms quiet time. The SiD electronics is designed to cope with up to 8192 bunches per train and a bunch spacing of down to 300 ns and can easily satisfy the current ILC requirements of up to 2625 bunches per train and a bunch spacing of 344 ns [84]. A simplified block diagram of the SiD data-acquisition from the front-end electronics to the online-farm and storage system is shown in Figure 9.0.1.

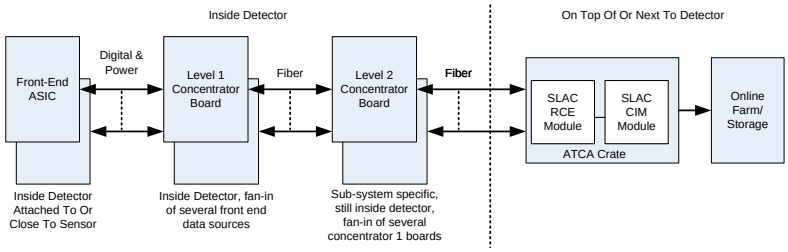

Figure 9.0.1: Simplified block-diagram of the SiD detector control and readout chain using the ATCA RCE and CIM modules.

9.1 ASIC developments

All subsystems with the exception of the Vertex detector (for which the sensor technology has not been selected yet) and the BeamCal (which has approximately unit occupancy) are

foreseen to be read out by variants of KPiX as the front-end Application-Specific Integrated Circuit (ASIC). For the BeamCal the Bean ASIC has been developed to address its specific requirements, see Section 8.1.3.

9.1.1 KPiX

KPiX [24, 25] is a multi-channel system-on-chip, for self triggered detection and processing of low level charge signals. Figure 9.1.1 shows a simplified block diagram of the KPiX, processing signals from 1024 input channels. The low level charge signal at the input is processed by the charge amplifier in two ranges with an automatic range switching controlled by the range threshold discriminator. The built-in calibration is covering the dynamic full range of up to 10 pC. Leakage compensation is available for DC-coupled detectors and either internal or external trigger options can be selected.

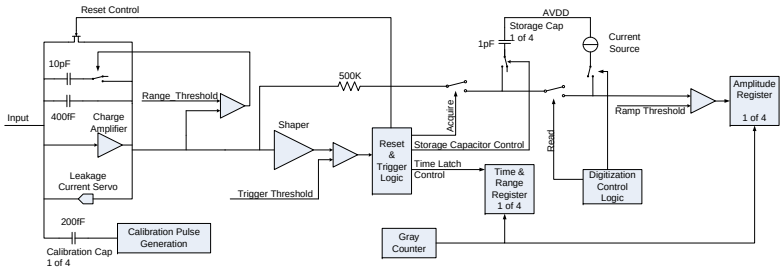

Figure 9.1.1: Simplified block-diagram of one KPiX channel

Up to four sets of signals for each channel can be stored in one acquisition cycle corresponding to one ILC bunch train. The timestamp is stored using a 13 bit deep counter, while the signal amplitude is first stored as a voltage on a capacitor before its subsequent digitisation using a Wilkinson-type ADC with 13 bit resolution. At the end of the acquisition and digitisation cycle nine words of digital information are available for each of the 1024 cells of the KPiX chip. The data is then read out serially from the KPiX before the next acquisition cycle starts. The power consumption for each individual channel is less than 20 µW. The latest version of KPiX has been manufactured using a 250 nm mixed-mode CMOS process and is currently being tested [25].

Table 9.1.1 lists the currently foreseen number of KPiX ASICs for each subsystem. Tracker, ECAL, and HCAL use the 1024-channel version of the KPiX while the Muon subsystem uses a 64-channel KPiX version.

Table 9.1.1: Approximate count of KPiX ASICs for each subsystem.

Sub-System	KPiX Count	Channels/KPiX
Tracker	27464	1024
ECAL	102573	1024
HCAL	35071	1024
Muons	8839	64
Total	173947	

9.2 On-Detector Electronics

As illustrated in Figure 9.1.1, several front-end ASICs (KPiX, Bean or Vertex ASICs) are connected to a Level-1 Concentrator (L1C) board using LVDS. The main functions of the L1C board are to fan out incoming signals and commands to the front-end modules and to bundle data from the front-end modules for transmission to the Level 2 Concentrator (L2C) boards. Additionally it can perform zero-suppression and sorting of the incoming event data. Just as an example, for the ECAL Barrel a total of 96 1024-channel KPiX chips would be served by eight front-end cables with twelve KPiX per L1C board. The total number of Level 1 concentrator boards in the ECAL Barrel would be 821 L1C boards and 52 L2C boards (80000 KPiX, 96 KPiX for each L1C board, 16 L1C boards for each L2C board). Figure 9.2.1 shows a block diagram of the L1C board.

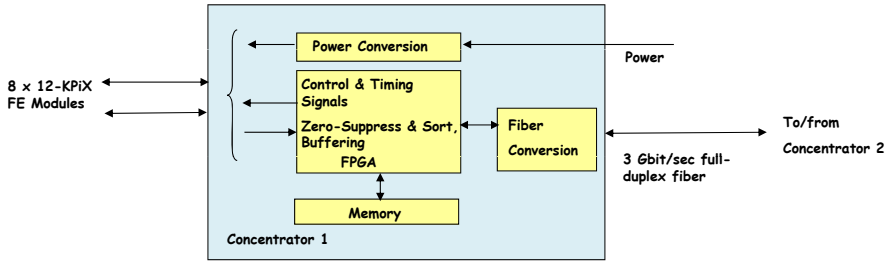

Figure 9.2.1: Block Diagram of the Level 1 Concentrator Board

The Level 1 Concentrator boards are in turn connected via 3-Gbit/s fibres to the Level-2 Concentrator boards. Besides distributing signals to/from the L1C boards, the L2C boards merge and sort the data-streams of the incoming event data received from each L1C board

before transmission to the off-detector processor boards. The L2C boards are either located inside the detector or outside, depending on the sub-system. E.g. for the ECAL Barrel there are 52 L2C boards inside the detector volume.

9.3 Off-Detector Electronics

The L2C boards are connected via fibres to ATCA crates either on or next to the detector. ATCA (Advanced Telecommunications Computing Architecture) is the next generation communication equipment currently used by the telecommunication industry. It incorporates the latest trends in high-speed interconnect, processors and improved Reliability, Availability, and Serviceability (RAS). Essentially, instead of parallel bus back-planes like VME, it uses high-speed serial communication and advanced switch technology within and between modules, redundant power, plus monitoring functions. For SiD the usage of 10 Gbit/s Ethernet is foreseen as the serial protocol.

Two custom ATCA boards, the Reconfigurable Cluster Element (RCE) Module and the Cluster Interconnect Module (CIM) were already designed previously. Based on those two modules, a second generation RCE was built, as shown in Figure 9.3.1 which combines the switch interconnect function of the CIM onto the RCE itself. A 96-port 10 Gbit/s Ethernet ASIC is placed on the RCE, providing communication between all the RCE modules in a crate and to destinations external to the crate with data rates up to 10 Gbit/s. The RCE modules connect via the backplane to the Rear Transition Modules (RTM) which interface via 48 3-Gbit/s fibre links to the sub-system L2C boards. The main ATCA board can hold up to five daughter-cards (shown in Figure 9.3.1) each with a Virtex FPGA with two embedded PowerPC processors, four Gbytes of DDR3 memory, 8 Gbytes/sec cpu-data memory interface, four 10-Gbit/s Ethernet event data interfaces, and an open-source RTEMS realtime operating system.

One ATCA crate can host up to 14 RCE boards, providing connections to $48 \times 14 =$ 672 3-Gbit/s fibre links into the detector for a 2 Tbit/s IO.

The maximum available data transfer rate is up to 520 Gbit/s, while the estimate for the complete SiD detector is approximately 320 Gbit/s including a factor of two safety margin. In principle, a partially loaded ATCA crate could serve the complete detector. However for partitioning reasons, the ability to run each of the subsystems completely independently during commissioning is highly desirably, and therefore a crate for each subsystem is planned.

The data is further sorted by an event-by-event basis in the ATCA system and then sent to the online processing system for potential further data reduction. Whether further data reduction is required is not determined yet, and the data may directly be forwarded to the offline system. Note that the event data is zero-suppressed in the sub-systems without the

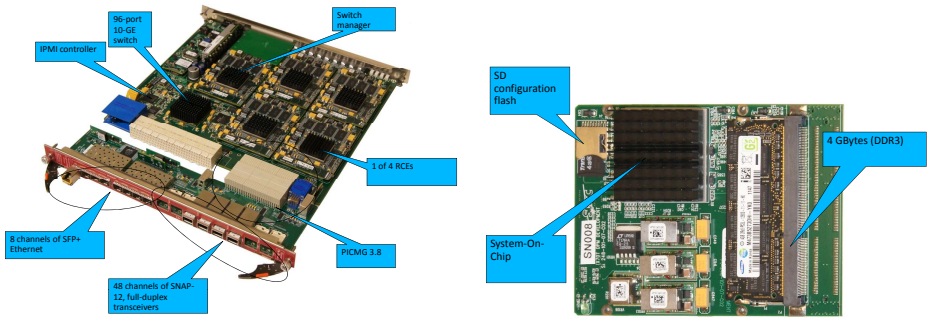

Figure 9.3.1: ATCA Reconfigurable Cluster Element (left) and RCE daughter module (right)

need for a global trigger system. All data produced in the front-ends above a programmable threshold is subsequently read out. For diagnostics and debugging, the DAQ includes the ability to assert calibration strobe and trigger signals, transmitted to the front-ends via the Level-2 and Level-1 Concentrator boards using the fibres shown in Figure 9.0.1.

Power Conversion circuits on the Level 2 and Level 1 Concentrator boards supply the power to the front-ends, starting with 48 V or higher voltages from off-detector supplies and then using DC-DC converters. Alternatively, serial powering architectures are also under consideration. The power supplies will be located in several racks on or next to the detector.

Environmental and health monitoring circuits are also included on the concentrator boards. In addition there may be additional monitoring boards in the detector, connected to RCE fibre interfaces. In addition there are crates of monitoring modules mounted in several racks on or next to the detector.

9.4 Overview of Electronics Channels and Expected Data Rates

Table 9.4.1 provides a global overview of the electronics channels of the full SiD detector. For each SiD subdetector the detector granularity, as currently used in the simulation model, and the approximate number of readout channels are listed. Preliminary studies have been carried out to estimate the average and maximum cell occupancies to be expected for a full bunch train at the ILC at 1 TeV. The number of bits per hit provides a first estimate, and is based on an approximation for individual hits with full on-detector zero-suppression and without local on-detector clustering. The KPiX chip presently provides fast buffering of up to 4 hits per channel. The KPiX design can be adapted to contain a larger buffer depth if deemed required for high-occupancy regions. The estimated data volume per bunch train is

also listed.

The beam parameters at 1 TeV presume 476 ns bunch separation and 2500 bunches per train. In the vertex and main tracker regions, it was found that the occupancy from $\gamma\gamma \rightarrow$ hadrons events is typically more than one order of magnitude below the occupancy from incoherent pairs. The occupancies in the vertex and tracker have therefore been calculated using incoherent pairs only. Average cluster sizes of 3.1 and 2.6 have been assumed for the pixel and strip detectors respectively. To account for uncertainties in the production of incoherent pairs and their associated impact on the detector, a safety factor of five has been included in the table. The table will be complemented at a later date with estimated occupancies in the calorimetry and muon system.

Table 9.4.1: Overview of readout details for the various subdetectors of the SiD detector concept. Occupancies and data volumes are for a full bunch train at 1 TeV and include beam-induced background as well as charge sharing between pixels/strips. A safety factors of five has been applied to the rates of incoherent pairs.

	cell size (mm^2)	number of channels (10^6)	av. to max. occ. (%)	approx. # bits per hit (bit)	data volume (Mbyte)
VTX barrel	0.02×0.02	408	50 - 60	32	1600
VTX disks inner	0.02×0.02	295	4 - 70	32	100
VTX disks outer	0.05×0.05	980	0.5 - 20	32	40
TRACKER barrel	0.05×100	16	12 - 300	32	20
TRACKER disks	0.05×100	11	4 - 500	32	4
ECAL barrel	3.5×3.5	72		40	
ECAL endcap	3.5×3.5	22	-	40	
HCAL barrel	10×10	30		40	
HCAL endcap	10×10	5	-	40	
LumiCal	2.5×var.	0.061	-	40	
BeamCal	2.5(5.0)×var.	0.076		40	
MUON barrel	41×var.	0.026	-	32	
MUON endcap	41×var.	0.022	-	32	

Chapter 10

Simulation and Reconstruction

10.1 Overview of the Simulation and Reconstruction Software

A large fraction of the software for the generation, simulation and reconstruction is shared between the ILD and SiD detector concepts (see the Common Section). The generated events are simulated in the SiD detector by SLIC [85], a program encapsulating the functionality of the GEANT4 [86] toolkit, but providing the ability to define all aspects of the detector at runtime. The output information consists of ideal hits in the sensitive detectors which contain the primary information regarding the energy deposition, hit position, time and Monte Carlo particle causing the energy deposition. At this level each of the physics events at 1 TeV is merged with a simulated event containing the equivalent of one bunch crossing of incoherent pair interactions. Additionally, hits and particles from $\gamma\gamma \rightarrow$ hadrons events are merged with each physics event. The number of $\gamma\gamma \rightarrow$ hadrons events follows a Poisson distribution with a mean of 4.1 (1.7) at 1 TeV (500 GeV). Events produced for the 500 GeV study are not merged with incoherent pairs background.

The energy deposits in the active material of the detectors are then digitised into simulated hits using the `org.lcsim` reconstruction framework [87]. A more detailed description of the digitisation is given in Section 10.4. Pattern recognition and track fitting is the task of the SeedTracker algorithm, which has been used successfully in the benchmarking of SiD detector variants at a 500 GeV ILC [1] as well as at a 3 TeV CLIC [56]. The algorithms of the PANDORAPFA package [88] are responsible for the calorimetric reconstruction and the creation of particle flow objects (PFOs). In a first step, muons are identified, their hits removed from the calorimeters, and the remaining hits are clustered using a cone clustering algorithm. Charged particles are created through the positive match of a track with a cluster, where consistency of the measured energies is ensured through iterative re-clustering. The

remaining clusters are assigned to neutral PFOs. A more detailed description of the particle ID is given in Section 10.5.1.

Vertices from secondary interactions are found by the LCFIPlus [89] flavour tagging package. This step is executed before the jet clustering, and all tracks in an event are used as input to the vertex finding algorithm, thereby eliminating the splitting of secondary decays across jets. The found vertices are then used in the jet clustering, which is described in more detail in Section 11.2.1.

10.2 The SiD DBD Production

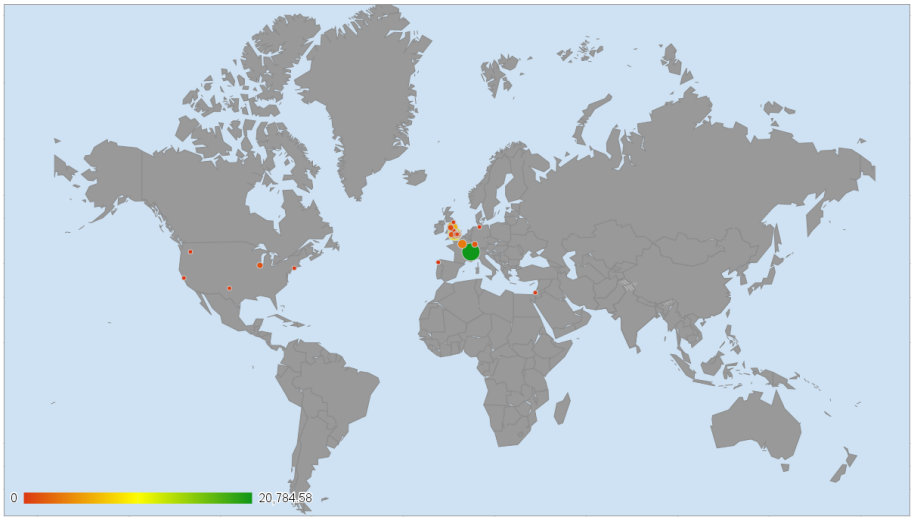

Figure 10.2.1: DIRAC production

All of the detector response simulation and event reconstruction was performed on the Grid using the ILCDIRAC [90] grid production tool. This software was used for the full chain of production cataloguing, job submission (and automatic-resubmission when necessary), error-handling, and monitoring. All of the jobs were submitted under the common ILC Virtual Organisation. Figure 10.2.1 shows a worldwide density plot of the Computing Elements used for the physics benchmarking production. Major contributors were CERN, various Grid sites in the UK (primarily RAL and Manchester), and OSG resources at FNAL and PNNL.

10.3 Simulating the SiD Detector Geometry

10.3.1 The SIDLOI3 Model

The SIDLOI3 detector model reflects the design of SiD, as described in this document, as faithfully as possible. All of the tracker elements are therefore modelled as planar silicon wafers with accompanying support structures. The geometry of the services (power and readout) are simplified, but reflects the gross amount and general distribution of the materials. The calorimeters are modelled as polygonal staves in the barrel region or planes in the endcaps, with interleaved readouts. However, since this model was used to characterise the detector response and as the basis for the physics benchmarking analyses, the design had to be frozen before all of the final subdetector designs became available, so some of the details of the implementation may differ from that described in the subdetector chapters. The complexity of this detector model does not lend itself easily to a simple textual description. We therefore give a brief, general description of each subdetector and present a few figures to give an indication of the level of detail implemented in this model. For the complete details of the model as implemented in GEANT4 see [91].

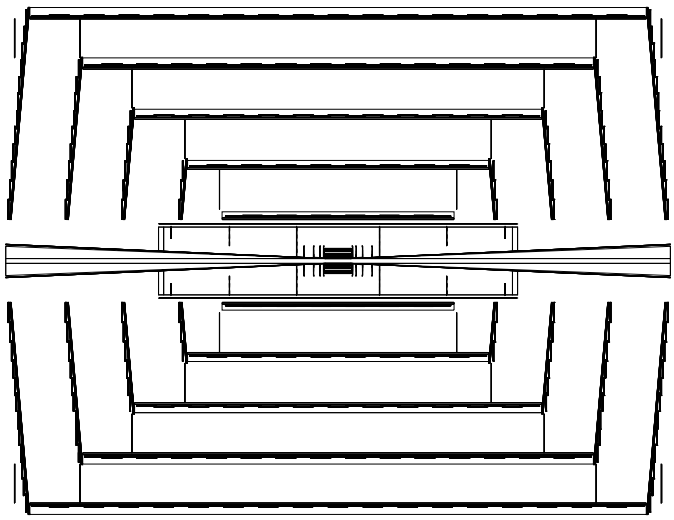

Figure 10.3.1: R-z view of the tracking system as implemented in SIDLOI3 model. Some support and readout structures have been hidden to improve the visibility of sensors.

A cross-section of the tracking detector is shown in Figure 10.3.1. This is to be compared with Figure 3.2.1 showing an engineering elevation view of the tracking system. An orthographic cutaway view of the central tracker as implemented in the SIDLOI3 model is shown in Figure 10.3.2 (left). An orthographic cutaway view of the complete detector as implemented in the SIDLOI3 model is shown in Figure 10.3.2 (right). The electromagnetic barrel calorimeter is modelled as a dodecagonal tube with overlapping staves. The hadron calorimeter barrel is composed of twelve symmetric staves. Finally, the octagonal layout of the magnetic flux return yoke, with its eleven layers of muon detection instrumentation is clearly visible.

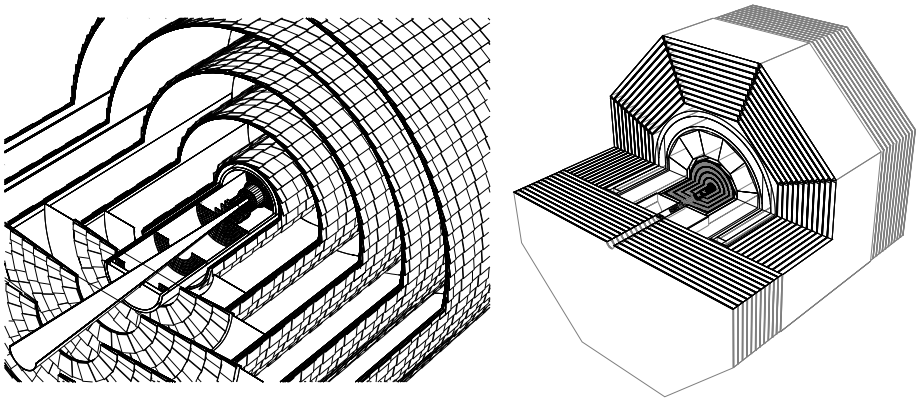

Figure 10.3.2: Cutaway view of the tracking system as implemented in SIDLOI3 (left) and the calorimeters (right) Some support and readout structures have been hidden to improve the visibility of sensors (left) and the calorimeters.

Figure 10.3.3 (left) shows the cumulative hadronic interaction lengths of the SiD detector elements as a function of the polar angle θ, demonstrating the good containment of hadronic showers in the calorimeters and the self-shielding provided by the thick mantle of the flux-return steel, while Figure 10.3.3 (right) displays cumulative material (expressed as a fraction of X_0) of the tracking region.

10.4 Simulation of the full Detector Response

The hits which are recorded and written out from the full Monte Carlo simulation contain ideal information. To simulate the response of a realistic, physical detector, this information needs to be converted to information which represents the electronic readout that would be collected from the detector. We refer to this process as hit digitisation.

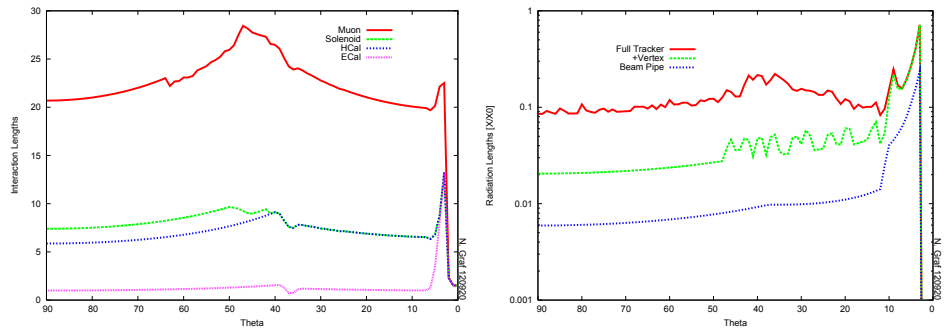

Figure 10.3.3: The nuclear interaction lengths of SIDLOI3 (left) and the radiation lengths of SIDLOI3 tracking system (right) as a function of the polar angle θ.

10.4.1 Silicon Pixel and Strip Hit Digitisation

The silicon-based tracking detectors are precision devices with very high intrinsic spatial resolutions. In order to realistically model their response, the effects of charge drift and diffusion in the silicon, as well as effects of pulse shaping and electronic noise need to be implemented in the simulation. The charge deposition for silicon strip detectors is simulated using an algorithm based on the CDF silicon sensor simulation and the readout employing the KPiX chip is simulated. An extension of this model to pixels is used to model the response of the vertex detector elements.

Additionally, the general-purpose package PixSim is available to model the response of pixelated silicon sensors. It simulates the generation of the charge carriers in the active media of the detector, the propagation of these carriers through the pixel volume under the influence of both electric and magnetic fields, taking into account diffusion of the carriers in the process of such propagation, the collection of the carriers by charge collecting electrodes, the forming of the signals and the processing of the resulting signals by electronics and reconstruction software. It is extremely flexible, allowing all aspects of different readout technologies to be studied in detail.

10.4.2 Calorimeter Hit Digitisation

Calorimeters are designed to measure the energy of incident particles by inducing them to catastrophically interact (shower) in the detector and to record the deposited energy. Because of the vast number of secondary particles produced when an incident particle showers, and because precise details of these secondary particles are unimportant to the energy measurement, we do not by default record ideal hits for each of them. Instead, we define

volume elements in which we simply sum up the total amount of deposited energy, and record the earliest time of deposition from each separate incident particle. Since we are employing sampling calorimeters, we need to multiply this energy deposited in the sensitive readout layers by sampling fractions to estimate the total amount of energy deposited in the calorimeters. These sampling fractions are determined from the response of SIDLOI3 to single particles. Muons, photons and K_L^0 at a variety of energies are used to determine the MIP, electromagnetic, and hadronic sampling fractions, respectively.

10.4.3 Clustering

The association of nearby strips, pixels or volume elements into a single hit is referred to as clustering. The signal sharing across readout elements can lead to improvements in the measurement precision and is therefore a crucial step in the reconstruction. However, overly aggressive clustering can easily lead to a degraded performance. The algorithms used by PANDORAPFA to cluster energy depositions in the calorimeters are described in the common software section of this document (see the Common Section). The silicon strip and pixel signals are clustered using a nearest neighbour algorithm. Hash maps are used to achieve approximately linear scaling of clustering time. Settable parameters are provided for noise, readout and clustering thresholds. Tracker hits are then created from these clusters. The position measurements (1D for strips, 2D for pixels) are derived from the energy-weighted centroids of the clusters, and the uncertainties are provided on a cluster-by-cluster basis. These hits are the input for the track finding.

10.5 Detector Performance

10.5.1 Particle Identification: Photon, Electron and Muon ID

Particle identification (particle ID), and in particular lepton identification will be central to many physics studies at the ILC. In particular, particle ID plays an active role in the PANDORAPFA reconstruction. Muons are identified and all of their hits removed before the calorimeter hits are clustered. The track-cluster agreement is optimised using various re-clustering strategies, which are guided by identifying the cluster as belonging to an electromagnetic or a hadronic interaction.

The particle identification has been evaluated on samples of single photons, electrons, muons and pions of 10 GeV and 100 GeV, respectively (see Figures 10.5.1,10.5.2,10.5.3). In these plots, the reconstructed particle is required to have the same type as the generated particle, and a loose energy cut of five times the resolution of the EM calorimeter above or below the generated particle is applied. The default for neutral particles is the neutron

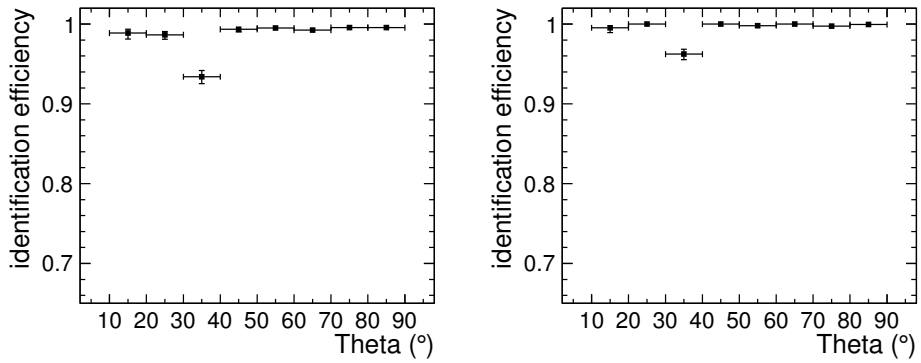

Figure 10.5.1: Particle identification efficiency for 10 GeV photons (left) and 100 GeV photons (right) as a function of the angle θ.

hypothesis, while charged particles are assigned the pion hypothesis by default. The performance of the reconstruction as shown here has not been optimised for particle identification efficiency, but rather for jet energy resolution. We expect a significant improvement can be achieved - particularly in the transition region between calorimeter barrel and endcap - with dedicated particle identification algorithms that are optimised for performance with a digital HCAL.

10.5.2 Jet Flavour Tagging: Efficiency and Purity

The ability to tag bottom and charm decays with high purity is a crucial aspect in the design of the vertex detector. The flavour tagging performance of the SiD detector concept has been studied in the context of the $t\bar{t}h$ analysis for b-tagging in a multi-jet environment, and for tagging of bottom and charm quarks, as well as gluons, in the context of the measurement of the Higgs branching ratios. Figure 10.5.4 shows the b-tagging efficiency of a light quark sample (red curve) or a charm quark sample (green curve) versus the b-tagging efficiency of a bottom quark sample. The neural networks have been trained on a sample of di-jets at $\sqrt{s} = 91$ GeV and tested on a statistically independent sample.

Vertex Resolution

One of the most important variables in jet flavour tagging networks is the decay length of the secondary vertices. The vertex resolution of the SiD vertex detector has been assessed in a sample of Z decays to light quarks at $\sqrt{s} = 91$ GeV. Figure 10.5.5 (left) shows the

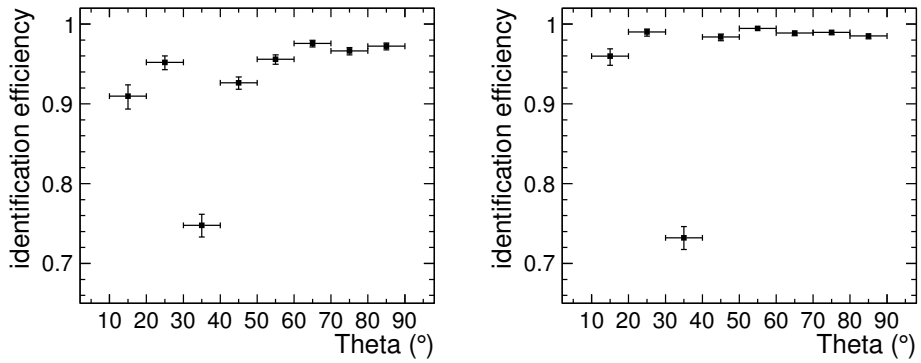

Figure 10.5.2: Particle identification efficiency for 10 GeV electrons (left) and 100 GeV electrons (right) as a function of the angle θ.

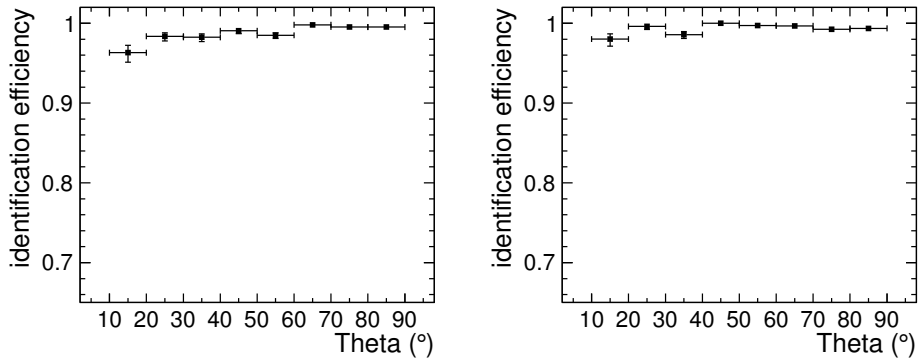

Figure 10.5.3: Particle identification efficiency for 10 GeV muons (left) and 100 GeV muons (right) as a function of the angle θ.

position of the reconstructed primary vertex. The physics interaction has been generated at the position (0, 0, 0), and the primary vertex constraint, which is used in the production, has been turned off for the purpose of this study.

Figure 10.5.5 (right) shows the resolution of the primary vertex position versus the number of tracks originating from the primary interaction. Even though different algorithms are used to reconstruct primary and secondary vertices, the secondary vertex resolution can be inferred from this figure if the number of tracks is known.

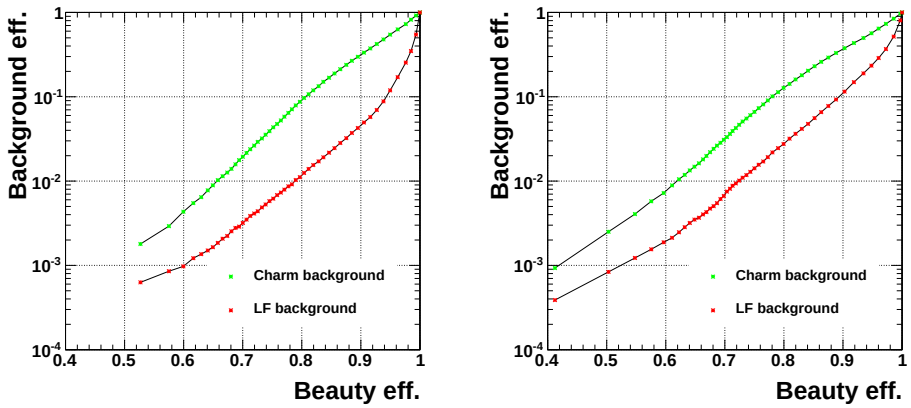

Figure 10.5.4: Mis-identification efficiency of light quark events (red points) and charm quark events (green points) as beauty quark events versus beauty identification efficiency in di-jets at $\sqrt{s} = 91\,\text{GeV}$. The performance is shown without background (left) and when including background from $\gamma\gamma \to$ hadrons events and incoherent pairs (right).

10.5.3 Di-Jet Energy Resolution

The design of the SiD detector concept has been optimised for jet energy resolution using the particle flow approach. This puts stringent requirements on the interplay of the various subdetectors and has led to the choice of calorimeters with a high degree of segmentation and transverse granularity. In addition, sophisticated reconstruction algorithms are necessary to obtain a jet energy resolution that allows to separate W and Z decays.

Figure 10.5.6 (left) shows the PFA di-jet energy resolution without the effects from jet finding or background. The events consist of Z′ bosons of different masses decaying at rest to a pair of light quark jets. Figure 10.5.6 (right) shows the di-jet energy resolution in $e^+e^- \to$ ZZ events at different collision energies, where one Z decays to neutrinos, the other one to two light quarks that give rise to two jets. The events have been clustered into two jets using the k_t algorithm as implemented in the FASTJET [92] package. The jets are combined to form a Z boson. As the energy is shared between the two Z bosons, the reconstructed energy is expected to be one half of $\sqrt{s}$. The energy distributions of Z bosons at different energies are shown in Figure 10.5.7. To avoid a bias from possible tails, it has become common practice to compute the rms90 value when describing the energy resolution of a particle flow algorithm. It is defined as the root-mean-square of the distribution in the smallest range that contains 90% of the events.

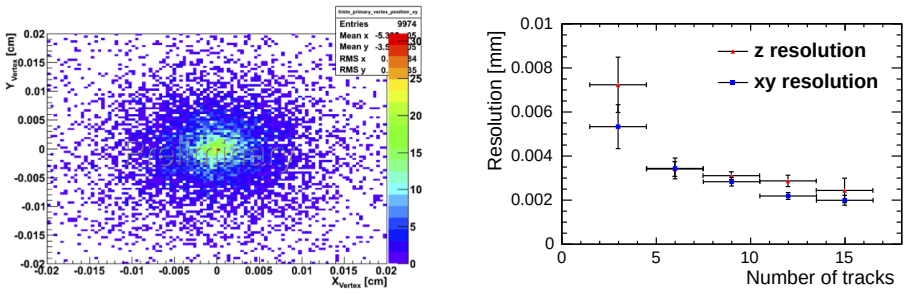

Figure 10.5.5: Position of the reconstructed primary vertex (left) and resolution of the primary vertex position as a function of the number of tracks originating from that vertex (right).

The value at each point in Figure 10.5.6 (right) is computed as rms90(E)/E and given in per cent. A relative Poissonian error of $1/\sqrt{N}$ has been assigned, where N is the number of successfully reconstructed events out of 10000 generated events at each energy. The addition of background from $\gamma\gamma \rightarrow$ hadrons events and incoherent pairs results in only a minor change in resolution in these events. The difference can be explained by the additional background energy in the reconstructed jets balancing the small reconstruction bias towards lower energies in events without background.

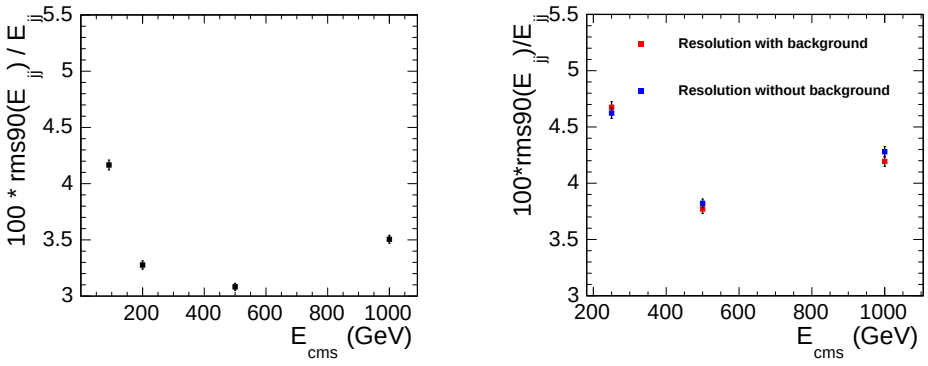

Figure 10.5.6: Left: Energy resolution of reconstructed Z′ events of different masses decaying at rest to a pair of light quark jets. Right: Energy resolution of reconstructed ZZ events with and without the backgrounds from $\gamma\gamma \rightarrow$ hadrons events and incoherent pairs at different values of $\sqrt{s}$. In these events, one Z boson decays invisibly and the other to a pair of jets.

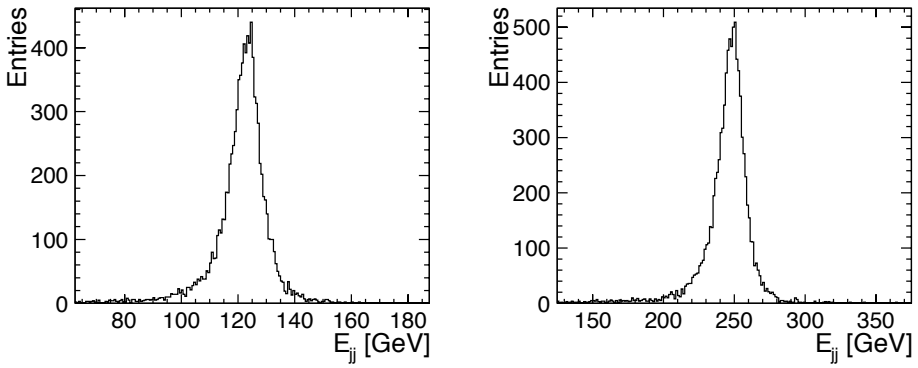

(a) $\sqrt{s} = 250\,\mathrm{GeV}$

(b) $\sqrt{s} = 500\,\mathrm{GeV}$

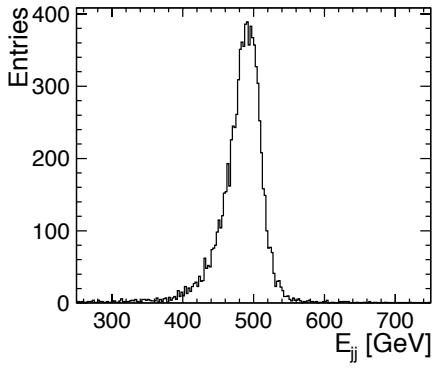

(c) $\sqrt{s} = 1000\,\mathrm{GeV}$

Figure 10.5.7: Distributions of the reconstructed energy in Z Z events at different values of $\sqrt{s}$, where one Z decays invisibly and the other to a pair of jets.

Chapter 11

Benchmarking

11.1 Event Generation

The event generation was a collaborative effort between SiD and ILD. The WHIZARD Monte Carlo was used for the generation of all $2 \to n$ processes, $n = 2,3,4,5,6$, where n is the number final state fermions (e,μ,τ,u,d,s,c,b), and the two initial state particles are e^+e^-, $e^+\gamma$, $e^-\gamma$, or $\gamma\gamma$. The PHYSSIM Monte Carlo program was used to generate the $t\bar{t}h$ signal process and eight fermion background. All event samples were generated with 100% polarisation for the initial state electron and positron. The event generation output was stored on the grid, and a complete copy was also kept on SLAC NFS. A complete review of the event generation process is given in the chapter on common tasks and issues.

11.1.1 Signal and Background samples used for full simulation and reconstruction

Events from stdhep files with different 100% initial state polarisations and possibly different final states were combined to form "mixed stdhep files" with 80% electron and 20% (30%) positron polarisation for $\sqrt{s}$ =1000 (500) GeV. Only mixed stdhep files were used as input to the full simulation and reconstruction in SiD. These are summarised in Table 11.1.1. Separate mixed background files were generated for the dominant $\nu\bar{\nu}h$ background, while everything else was lumped together in "all other SM processes". The composition of the events in "all other SM processes" is shown in Table 11.1.2.

Table 11.1.1: Mixed stdhep files used as input for full simulation and reconstruction

Process	$\sqrt{s}$ (GeV)	# Events (10^6)	$\mathscr{L}$ ab^{-1}
$t\bar{t}h$	1000	0.4	52
$ttZ, ttbb$	1000	0.4	15
tt	1000	1.0	2.0
$\nu\bar{\nu}h,\ h \to b\bar{b}, c\bar{c}, WW^*, gg$	1000	3.1	7.4
$\nu\bar{\nu}h,\ h \to \mu^+\mu^-$	1000	0.5	6400
$e\nu W, eeZ, \nu\nu Z \to e\nu qq, eeqq, \nu\nu qq$	1000	4.0	0.034
$eeZ, \nu\nu Z, WW \to ee\mu\mu, \nu\nu\mu\mu$	1000	1.0	0.004
WW	1000	6.0	2.0
all other SM processes	1000	6.0	$1 \cdot 10^5 - 1.0$
$t\bar{t}$	500	2.0	1.0 per m_{top}
$t\bar{t}$ background SM processes	500	2.0	varies
TOTAL		26	

Table 11.1.2: Contents of "all Other SM Processes" Mixed File.

Process	$\mathscr{L}$ ab^{-1} per pol.	# Events (10^5) P(e^-/e^+) -0.8/+0.2	# Events (10^5) P(e^-/e^+) +0.8/-0.2	Weight
$e\gamma \to e\gamma$	$4 \cdot 10^{-5}$	0.5	0.5	$2.5 \cdot 10^{+4}$
$e^+e^- \to 2f, 4f$	0.034	3.7	2.0	29
$e\gamma \to 3f$	0.003	3.5	3.1	330
$e\gamma \to 5f$	0.25	3.1	2.1	4
$e^+e^- \to 6f$	1.0	1.8	0.6	1
$\gamma\gamma \to 2f$	0.001	5.7	5.7	7700
$\gamma\gamma \to 4f$	0.083	2.5	2.5	12
$\gamma\gamma \to$ minijets:				
$4 < p_T < 40$ GeV	0.012	9.2	9.2	$80 - 9000$
$p_T > 40$ GeV	0.105	2.3	2.3	12

11.2 Analysis Tools

In this section the software tool common to more than one of the detector benchmark analyses are described.

11.2.1 Jet finding

To reconstruct jets in hadronic final states, the Durham algorithm as implemented in LCFIPlus or the k_t algorithm from the FastJet [93, 94] package were used. Especially for the reconstruction of jets in the forward direction, where the contribution from beam-related backgrounds is larger, the k_t algorithm developed for hadron collisions is more suitable. This was already demonstrated for the CLIC CDR. More details and the parameters used for the jet finding are given in the descriptions of the individual analyses.

11.2.2 Multivariate analysis tools

The traditional approach in high energy physics to separate a signal from backgrounds is based on a set of fixed cuts. However, for complex final states and large backgrounds this method is often not optimal. Hence multivariate analysis techniques like artificial neutral networks or boosted decision trees (BDTs) are commonly used today. The implementations of these models in the TMVA [95] were used for the benchmark analyses described in the following unless explicitly stated otherwise.

11.3 Summary of the LOI Results

For the SiD LOI [1] several physics performance studies have been conducted to quantify the physics performance of the SiD detector concept. Also these studies were used to broaden and emphasise the physics case of the ILC. From a list of physics benchmark reactions [96] six reactions were selected by the ILCSC Research Director. Three of them were conducted at a centre-of-mass energy of 250 GeV using a dataset of 250 fb^{-1}.

- $e^+e^- \to \mathrm{e^+e^-h}, \mu^+\mu^-\mathrm{h}$
- $e^+e^- \to \mathrm{hZ^0}$ $\mathrm{h} \to \mathrm{c\bar{c}}$ $Z \to \nu\bar{\nu}, \mathrm{q\bar{q}}$
- $e^+e^- \to \mathrm{hZ^0}$ $\mathrm{h} \to \mu^+\mu^-$ $Z \to \nu\bar{\nu}, \mathrm{q\bar{q}}$

The remaining three were conducted at $\sqrt{s}$ =500 GeV using a dataset of 500 fb^{-1}.

- $e^+e^- \to \tau^+\tau^-$

- $e^+e^- \to t\bar{t} \to 6$ jets
- $e^+e^- \to \tilde{\chi}_1^+\tilde{\chi}_1^-, \tilde{\chi}_2^0\tilde{\chi}_2^0$

In addition to these compulsory LOI benchmark reactions SiD has also investigated the the $e^+e^- \to \tilde{b}\tilde{b},\ \tilde{b} \to b\tilde{\chi}_1^0$ process. For all the LOI analyses, the SM Higgs mass was set to 120 GeV and the top quark mass was set to 174 GeV. In the following a short summary of the results from the individual benchmark analyses will be given, all results from the LOI are summarised in Table 11.6.1 as well. Compared to the DBD the detector simulation for the LOI [1] is less detailed, especially in the description of individual detectors modules.

For the analyses at $\sqrt{s} = 250$ GeV a dataset of 250 fb^{-1} was used using a polarisation set of 80% right-handed e^- and 30% left-handed e^+. This polarisation parameter set is then referred to as 80eR. Additional signal samples with 80% left-handed e^- and 30% right-handed e^+ (80eL)have also been provided.

One of the key measurements is the decay-mode measurement of the Higgs mass and cross-section using the process $e^+e^- \to hZ^0\ Z \to e^+e^-, \mu^+\mu^-, h \to$ anything. The recoil mass against the Z can then be measured very accurately using the leptonic Z decays.

The distributions for the recoil measurements in both the e^+e^-h and $\mu^+\mu^-h$ channels are shown in Figure 11.3.1. Main background sources include mainly di-boson production (W^+W^-,Z^0Z^0). The amount of W^+W^- background can be greatly reduced by running exclusively with the 80eR configuration.

A summary of the results of both leptonic Z modes and using both 80eR and 80eL is given in Table 11.3.1.

Table 11.3.1: Summary of Higgs mass and hZ^0 cross-section errors for different channels and the different luminosity assumptions. The error includes the measurement statistical error and the systematic error due to the finite statistics of the Monte Carlo training sample.

80eR (fb^{-1})	80eL (fb^{-1})	Channel	ΔM_H (GeV)	$\Delta\sigma_{hZ^0}/\sigma_{hZ^0}$
250	0	e^+e^-h	0.078	0.041
250	0	$\mu^+\mu^-h$	0.046	0.037
250	0	$e^+e^-h + \mu^+\mu^-h$	0.040	0.027
0	250	e^+e^-h	0.066	0.067
0	250	$\mu^+\mu^-h$	0.037	0.057
0	250	$e^+e^-h + \mu^+\mu^-h$	0.032	0.043

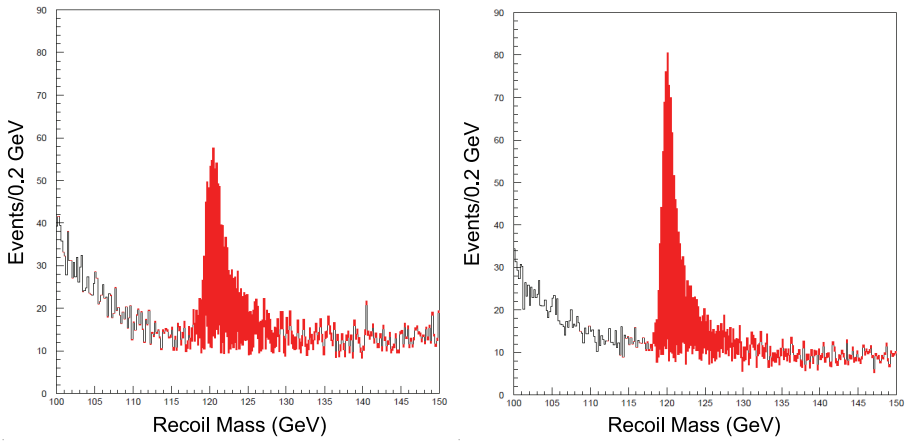

Figure 11.3.1: Recoil mass distributions following selection cuts for e^+e^-h (left) and $\mu^+\mu^-h$ (right) assuming 250 fb^{-1} luminosity with 80eR initial state polarization. The signal in red is added to the background in white; background is assumed constant over 5 GeV sections.

Measuring the branching ratios of the Higgs boson is of vital important to establish its nature. For the LOI the decays of the Higgs into $c\bar{c}$ and $\mu^+\mu^-$ have been studied using the Higgsstrahlung process, where the Z decayed either in $q\bar{q}$ or $\nu\bar{\nu}$. This separation of the $h \to c\bar{c}$ decay mode took advantage of the excellent c-tagging cabalities of SiD (see [1]) and employed neural networks to separate the $c\bar{c}$ signal from the overwhelming $h \to b\bar{b}$ background. For the $c\bar{c}$ branching ratio, the finally achieved accuracy is 11% ($Z \to \nu\bar{\nu}$) and is 6% $Z \to q\bar{q}$) respectively.

For the rare Higgs decay into $\mu^+\mu^-$ the challenge is to extract the signal out of an overwhelming Standard Model background of mainly four-fermion events. While for the $Z \to \nu\bar{\nu}$ decay mode, it has been proven quite difficult to extract the signal in the LOI analysis, the LOI analysis has demonstrated sensitivity in the hadronic channel, selecting 7.6 signal events over a background event of 39.3 events with a signal efficiency of 62%. This yields a measurement of the cross-section of this process of $\sigma_{hZ^0,h\to\mu^+\mu^-} = 0.074 \pm 0.066$ fb.

For the analyses at $\sqrt{s} = 500$ GeV a dataset of 500 fb^{-1} was used with a polarisation set of 80% right-handed e^- and 30% left-handed e^+.

The first analysis using the 500 GeV dataset studies the process $e^+e^- \to \tau^+\tau^-$ and tries to measure the τ polarisation with high precision. the measurement of the τ polarisation allows a search for multi-TeV Z' resonances. The identification of 250 GeV τ leptons and their decay modes is demanding for the entire detector. Tightly collimated jets with only

a few tracks must be reconstructed to identify the underlying charged hadron and π^0 constituents. Therefore additional reconstruction algorithms were applied in a second pass of the reconstructione, which were dedicated for identifying τ decays. This leads to τ samples with purities of 85% or larger. To measure the polarisation the optimal observable technique [97, 98] is used to measure the mean polarisation $< P_\tau >$ over all τ production angles. For the study two datasets with 250 fb^{-1} each were used using a polarisation of 80% right-handed e^- plus 30% left-handed e^+ (80eR) and 80% left-handed e^- plus 30% right-handed e^+ (80eL). The true $< P_\tau >$ values are 0.528 (80eR) and -0.625 (80eL) respectively.

The $< P_\tau >$ is then derived using a fit to the optimal observable as defined in [97, 98]. The results obtained for the mens polarisation are $< P_\tau >= 0.501 \pm 0.010$ (stat.) $\pm$ 0.006 (sys.) (80eR) and $< P_\tau >= -0.611 \pm 0.009$ (stat.) ± 0.005 (sys.) (80eL).

The second benchmark at $\sqrt{s}$ =500 GeV looked at top pair production, where both top quarks decay hadronically. The goal is to measure the cross-section, the top-quark mass and the forward-backward assymetry (A^t_{FB}). Events are selected by requiring two b-tagged jets and the events being compatible with a six-jet configuration. The mass is then reconstructed applying a constrained kinematic fit to all pre-selected events and selecting only candidate events with a good fit probability. The top mass and cross-section is then extracted using fit to the mass peak (see Figure 11.3.2). This yields a top-quark mass of 173.918$\pm$0.053 and a cross-section of 284.1$\pm$1.4 fb.

The forward-backward assymetry measurement again serves a window to new physics at the terascale [99]. A key tool for this analysis is the usage of the reconstructed vertex and jet charges. In this analysis both A^b_{FB} and A^t_{FB} are measured, yielding A^b_{FB}=0.272 ± 0.015 and A^t_{FB}=0.342 ± 0.015 respectively.

The last compulsory benchmark at $\sqrt{s}$ =500 GeV is the measurement of the masses of charginos and neutralinos in the processes $e^+e^- \to \tilde{\chi}^+_1\tilde{\chi}^-_1 \to W^+W^-\tilde{\chi}^0_1\tilde{\chi}^0_1$ and $e^+e^- \to \tilde{\chi}^0_2\tilde{\chi}^0_2 \to Z^0Z^0\tilde{\chi}^0_1\tilde{\chi}^0_1$. The analysis focussed on the final states with four jets and missing energy and thereby focussed on measuring the gaugino masses using di-jet final states from the two gause bosons. The four reconstructed jets where then paired using a χ^2 fit maximining the compatibility with the two di-jet pairs having equal masses. This then also allows separating the $\tilde{\chi}^+_1\tilde{\chi}^-_1$ from the $\tilde{\chi}^0_2\tilde{\chi}^0_2$ process by using the obtained di-jet resolutions (see Figure 11.3.2).

The masses of the gauginos was then derived using a template fit to the energy distributions of the reconstructed bosons. For the $\tilde{\chi}^\pm_1$ and $\tilde{\chi}^0_1$ masses from the $e^+e^- \to \tilde{\chi}^+_1\tilde{\chi}^-_1 \to W^+W^-\tilde{\chi}^0_1\tilde{\chi}^0_1$ process the resulting mass uncertainties are 450 MeV and 160 MeV. Using the $e^+e^- \to \tilde{\chi}^0_2\tilde{\chi}^0_2 \to Z^0Z^0\tilde{\chi}^0_1\tilde{\chi}^0_1$, uncertainties of 490 MeV and 280 MeV are obtained, which is higher due to smaller cross-section of $e^+e^- \to \tilde{\chi}^0_2\tilde{\chi}^0_2$ and the lower sample purity.

Additionally to these six compulsory benchmarks, SiD also looked into the $e^+e^- \to \tilde{b}\tilde{b}$, $\tilde{b} \to b\tilde{\chi}^0_1$ process at $\sqrt{s}$ =500 GeV in scenarios where the sbottom is the next-to-lightest

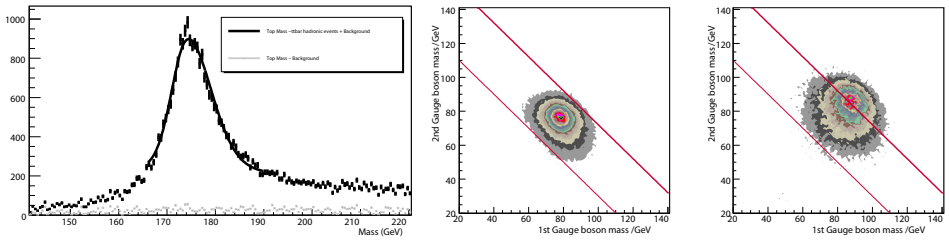

Figure 11.3.2: Top analysis: Distribution of the top invariant mass after kinematic fitting (left). Chargino/neutralino analysis: The reconstructed boson masses from the four jets, selecting chargino events with a pure chargino signal (center); and a pure neutralino signal (right). The region between the two straight lines indicates the allowed chargino selection window.

supersymmetric particle (NLSP) [100]. It has been shown, that SiD has sensitivity for this scenario up to sbottom masses close to the kinematic limit.

11.4 DBD Benchmark Reactions

For the DBD three additional benchmarks at $\sqrt{s}$ =1 TeV have been defined [101] using again a Higgs mass of 125 GeV and a data sample of 1 ab^{-1}.

The first benchmark is the process $e^+e^- \rightarrow t\bar{t}h$, where the Higgs decays into $b\bar{b}$. The final states include eight jets (all-hadronic) and six jets, a lepton and missing energy (semi-leptonic). The aim is to measure the Yukawa-coupling to $t\bar{t}$.

The second benchmark is a measurement of the Standard Model Higgs boson branching ratios into $b\bar{b}$,$c\bar{c}$,W^+W^-,gg and $\mu^+\mu^-$ using the $e^+e^- \rightarrow \nu_e\bar{\nu}_e h$ production process.

The last benchmark is a measurement of the forward $e^+e^- \rightarrow W^+W^-$ pair cross-section using considering both hadronic and leptonic decays of the W^+W^- pairs. The goal is to measure in situ the effective left-handed polarization $(1-P_{e^-})(1+P_{e^+})/4$ for each of two polarization configurations.

Additionally, one benchmark from the LOI had to be repeated using the DBD detector layout and the updated simulation and reconstruction software. SiD has chosen to repeat the $e^+e^- \rightarrow t\bar{t}$ analysis at $\sqrt{s}$ =500 GeV.

11.4.1 Measurement of the top Yukawa coupling

Two measurements of the cross section for the process $e^+e^- \rightarrow t\bar{t}h$ are described in the following. The Feynman diagrams for this process are shown in Figure 11.4.1. Here h is a

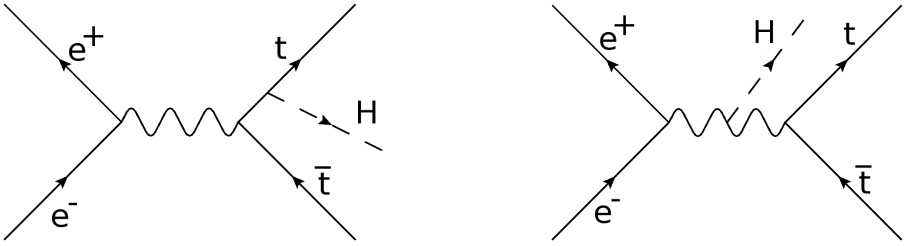

Figure 11.4.1: Diagrams for $t\bar{t}h$ production in e^+e^- collisions.

Standard Model Higgs boson of mass 125 GeV. The diagram shown on the left represents the dominant contribution to the cross-section. Hence the measurement of the $t\bar{t}h$ cross-section at the ILC allows a direct extraction of the top Yukawa coupling, y_t, with good precision. The contribution to the cross-section from Higgs radiation off the intermediate Z boson represents a small correction which needs to be taken into account in the extraction of y_t from the measured cross-section. In the analysis presented here, the Higgs decay $h \to b\bar{b}$ is considered. Two final states are investigated in the following:

- **8 jets:** In this case both top quarks decay hadronically. Hence this final state contains eight jets out of which four originate from beauty quark decays.

- **6 jets:** Here one top quark decays hadronically and the other top quark decays leptonically. The final state contains four b-jets, two further jets, an isolated lepton and missing energy. Only electrons and muons are considered as isolated leptons in the final state.

This study requires jet clustering in complex hadronic final states, missing energy reconstruction, flavor-tagging and reconstruction and identification of high energy leptons. Hence it represents a comprehensive check of the complete analysis chain and overall detector performance.

An overview of the cross-sections for the signal final states as well as for the considered backgrounds is shown in Table 11.4.1. For the measurement in the final state with six jets all other $t\bar{t}h$ events, i.e. all events where both top quarks decay leptonically or hadronically, or events were the Higgs boson does not decay into a beauty quark-antiquark pair, are treated as background. For the eight jets final state events where at least one top quark decays leptonically or where the Higgs boson does not decay into a beauty quark-antiquark pair are considered as background.

Table 11.4.1: Production cross-sections times branching ratios or production cross sections for the signals and for the considered backgrounds. All samples were generated assuming a Standard Model Higgs mass of 125 GeV. The numbers for "other $t\bar{t}h$" processes in this table do not inlcude both of the signal final states (see text). The $t\bar{t}Z$ and $t\bar{t}g^*$ samples do not contain events where both top quarks decay leptonically. The $t\bar{t}$ samples contain all possible decays of both top quarks.

Type	Final state	P(e^-)	P(e^+)	Cross-section [$\times$ BR] (fb)
Signal	$t\bar{t}h$ (8 jets)	-80%	+20%	0.87
Signal	$t\bar{t}h$ (8 jets)	+80%	-20%	0.44
Signal	$t\bar{t}h$ (6 jets)	-80%	+20%	0.84
Signal	$t\bar{t}h$ (6 jets)	+80%	-20%	0.42
Background	other $t\bar{t}h$	-80%	+20%	1.59
Background	other $t\bar{t}h$	+80%	-20%	0.80
Background	$t\bar{t}Z$	-80%	+20%	6.92
Background	$t\bar{t}Z$	+80%	-20%	2.61
Background	$t\bar{t}g^* \to t\bar{t}b\bar{b}$	-80%	+20%	1.72
Background	$t\bar{t}g^* \to t\bar{t}b\bar{b}$	+80%	-20%	0.86
Background	$t\bar{t}$	-80%	+20%	449
Background	$t\bar{t}$	+80%	-20%	170

Event reconstruction

As a first step of the event reconstruction chain, isolated leptons are searched for. The particle flow objects (PFOs) identified as muons or electrons are excluded from the jet reconstruction procedure. Only PFOs in the range $20^\circ < \theta < 160^\circ$ are considered in the following. The Durham jet clustering algorithm is used in the exclusive mode with six or eight jets. A B-tag value is obtained for each jet.

To form $W^\pm$, top and Higgs candidates from the reconstructed jets, the following function is minimised for the 8 jets final state:

$$\frac{(M_{12}-M_{W^\pm})^2}{\sigma_{W^\pm}^2}+\frac{(M_{123}-M_t)^2}{\sigma_t^2}+\frac{(M_{45}-M_{W^\pm})^2}{\sigma_{W^\pm}^2}+\frac{(M_{456}-M_t)^2}{\sigma_t^2}+\frac{(M_{78}-M_{\mathrm{h}})^2}{\sigma_{\mathrm{h}}^2}, \tag{11.4.1}$$

where M_{12} and M_{45} are the invariant masses of the jet pairs used to reconstructed the $W^\pm$ candidates, M_{123} and M_{456} are the invariant masses of the three jets used to reconstruct the

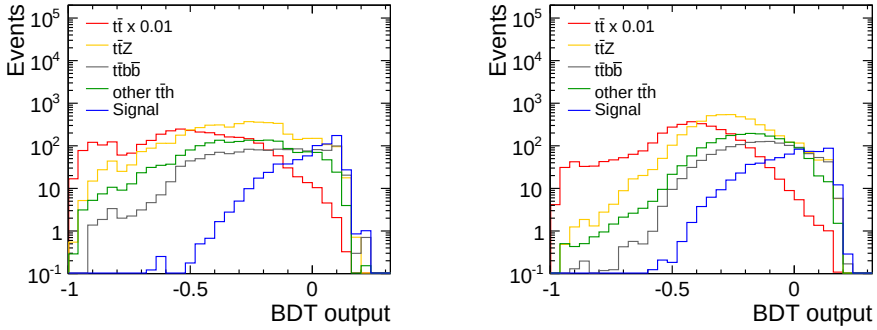

Figure 11.4.2: Output distributions of the BDTs for the eight (left) and six (right) jet final states. The signals are shown in blue while the backgrounds are shown in different colours. The distribution for $t\bar{t}$ was scaled by a factor 0.01.

top candidates and M_{78} is the invariant mass of the jet pair used to reconstruct the Higgs candidate. M_W, M_t and M_h are the nominal $W^\pm$, top and Higgs masses. The resolutions $\sigma_{W^\pm}$, σ_t and σ_h were obtained from reconstructed jet combinations matched to $W^\pm$, top and Higgs particles on generator level. The corresponding function minimised for the six jets final state is given by:

$$\frac{(M_{12}-M_{W^\pm})^2}{\sigma_{W^\pm}^2}+\frac{(M_{123}-M_t)^2}{\sigma_t^2}+\frac{(M_{45}-M_\mathrm{h})^2}{\sigma_\mathrm{h}^2}. \tag{11.4.2}$$

Event selection

Events were selected using boosted decision trees as implemented in TMVA (see Section 11.2.2). The BDTs were trained separately for the eight and six jet final states. The following input variables were used:

- the four highest B-tag values;
- the event thrust;
- a transition value from the Durham algorithm. For the six jet final state $Y_{6\to5}$ is used while $Y_{8\to7}$ is used for the eight jet final state;
- the number of reconstructed PFOs in the range $20^\circ < \theta < 160^\circ$;
- the number of identified isolated electrons or muons;

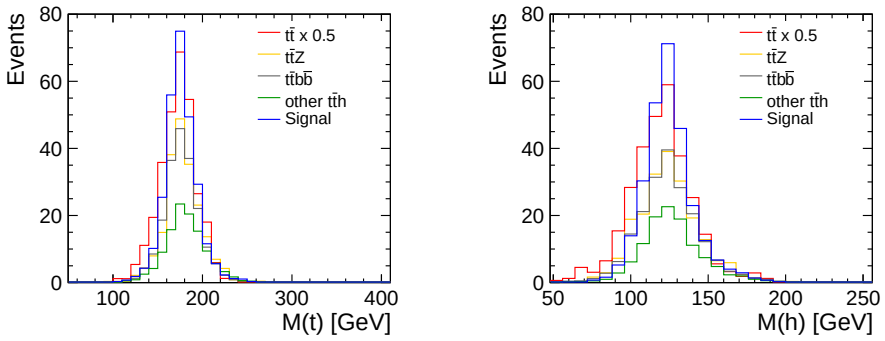

Figure 11.4.3: Reconstructed top (left) and Higgs (right) masses for selected (BDT > 0.0266) six jet events. The signal is shown in blue while the backgrounds are shown in different colours. The distribution for $t\bar{t}$ was scaled by a factor 0.5.

- the missing transverse momentum calculated from the reconstructed jets;
- the total visible energy defined as the scalar sum of all jet energies;
- the masses M_{12}, M_{123} and M_{45} as defined above.

For the eight jet final state two additional variables are included:

- M_{456} and M_{78} as defined above.

The output values of the BDTs for the signals and the different backgrounds are shown in Figure 11.4.2 for both final states. To select events, cuts on the BDT output values are applied. The cuts were optimised by maximising the signal significance given by: $\frac{S}{\sqrt{S+B}}$, where S is the number of signal events and B is the number of background events. As an example, the reconstructed top and Higgs masses in six jet events after the cut on the BDT output are shown in Figure 11.4.3.

Results on the cross section and top Yukawa coupling

The cross section can be directly obtained from the number of background-subtracted signal events after the event selection. Assuming an integrated luminosity of 1 ab^{-1}, the cross section can be measured with a statistical accuracy of 12.3% using the eight jet final state and with a statistical accuracy of 13.6% for the six jet final state. This translates to precisions on the top Yukawa coupling of about 6.2% and 6.8% from the eight and six jet final states, respectively. If both measurements are combined, the top Yukawa coupling can be

Table 11.4.1: Simulated data samples used for the $\nu_e\bar{\nu}_e h$ analysis.

Process	Polarization	#events
higgs_ffh_nomu	-80/+20	1,544,398
evW_eeZ_vvZ_semileptonic	-80/+20	6,570,292
all_other_SM_background	-80/+20	3,232,672

extracted with a statistical accuracy of 4.6%. The precision for the six jets final state could be improved further if τ-leptons were included in the reconstruction.

11.4.2 Higgs branching fractions

Here the process to be studied is $e^+e^- \to \nu_e\bar{\nu}_e h$ at $\sqrt{s}$ =1 TeV, where h is a SM Higgs boson of mass 125 GeV. This benchmark study provides a test of jet energy resolution, missing energy reconstruction, flavour-tagging, and reconstruction and identification of electrons and muons in the forward region. We measure the cross-section times branching ratio for the Standard Model Higgs boson decays into $b\bar{b}$,$c\bar{c}$,W^+W^- and gg using the $e^+e^- \to \nu_e\bar{\nu}_e h$ production process. We focus on the WW fusion process which dominates at high energies since the cross-section grows as $log(s)$. The datasets used for this analysis are shown in Table 11.4.1.

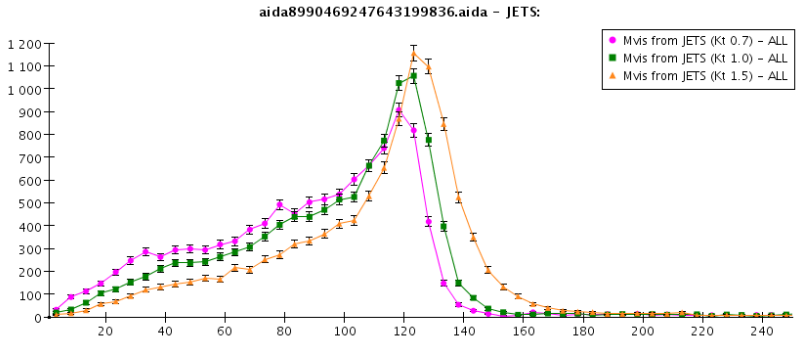

Figure 11.4.4: Visible mass distributions for $\nu_e\bar{\nu}_e h$ for jet clustering size parameter values from 0.07 to 1.5.

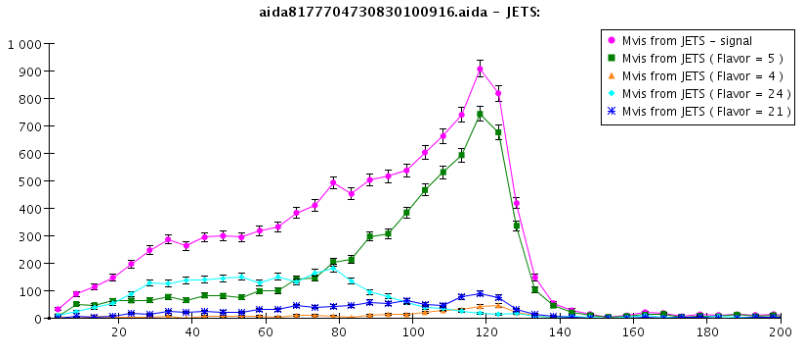

Figure 11.4.5: Visible mass distributions for $\nu_e\bar{\nu}_e$h for the various Higgs decay modes.

Events are clustered into two jets using the k_t algorithm. Events are preselected by requiring that the visible energy $E(\text{visible})$ and total visible transverse momentum $p_T(\text{visible})$ satisfy

$$100 < E(\text{visible}) < 400 \text{ GeV}, \quad 20 < p_T(\text{visible}) < 250 \text{ GeV}.$$

The jet clustering size parameter used for the k_t algorithm was chosen to be 1.5 based on the visible mass resolutions. A comparison of the visible mass distributions for different jet clustering sizes are shown in Figure 11.4.4 and the signal visible mass distributions separated by decay mode are shown in Figure 11.4.5.

The major background is from W$e\nu$ eeZ and $\nu\nu$Z events. The remaining background is rejected and the decay modes of the Higgs are discriminated by using Fisher Discriminants trained on small samples of the simulated signal and backgrounds. The input variables are the number of good tracks, the number of isolated electrons, the b and c flavour tagging outputs, the visible mass of the jets and the jet masses. Distributions of these input variables after the preselection are shown in Figure 11.4.6. The probability distributions for each of the Higgs decay modes are shown in Figure 11.4.7.

The cuts on the Fisher discriminant which maximized the $S/\sqrt{S+B}$ for each decay mode were applied. The selection efficiencies for each of the modes after preselection are $b\bar{b}$ (80%), $c\bar{c}$ (90%), W^+W^- (90%) and gg (90%). The overall selection efficiencies are $b\bar{b}$ (xxx), $c\bar{c}$ (xxx), W^+W^- (xxx) and gg (xxx). Using these efficiencies and the estimated number of background events we find that the SiD detector would obtain the relative uncertainties in the Higgs $\sigma \times BR$ shown in Table 11.4.2.

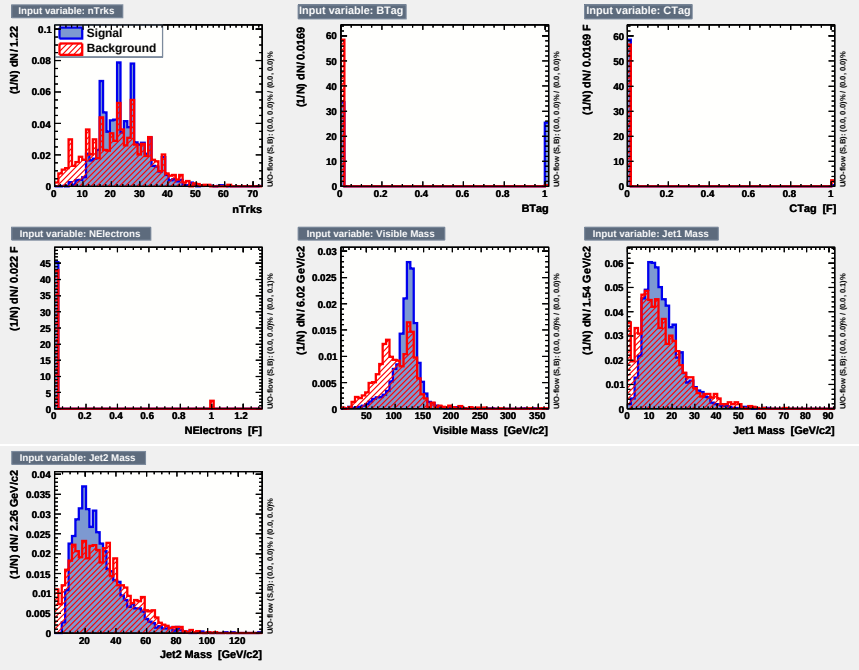

Figure 11.4.6: Distributions of the input variables for the training of the Fisher Discriminant for selecting signal events and separating the Higgs decay modes.

11.4.3 Measurement of beam polarisation using W^+W^- pairs

The baseline ILC design at $\sqrt{s}$ =1 TeV includes longitudinal electron and positron beam polarisations of 80% and 20% respectively. Polarimeters upstream and downstream of the collision point measure the average beam polarisation before and after collision, but cannot provide an estimate of the luminosity weighted beam polarisation without complex modelling of the beam collision process. Physics processes that are sensitive to beam polarisation, however, can directly measure the luminosity weighted beam polarisation.

The process $e^+e^- \rightarrow W^+W^-$ is very sensitive to beam polarisation. It is dominated by t-channel neutrino exchange in the forward region, where only left handed electron and right-handed positrons contribute, and continues to exhibit polarisation dependence in the central and backwards regions through s-channel Z boson production. The production of W^+W^- in the forward region has the advantages of high statistics and negligible sensitivity to new physics.

The primary objective of this benchmark is the measurement of the effective left and

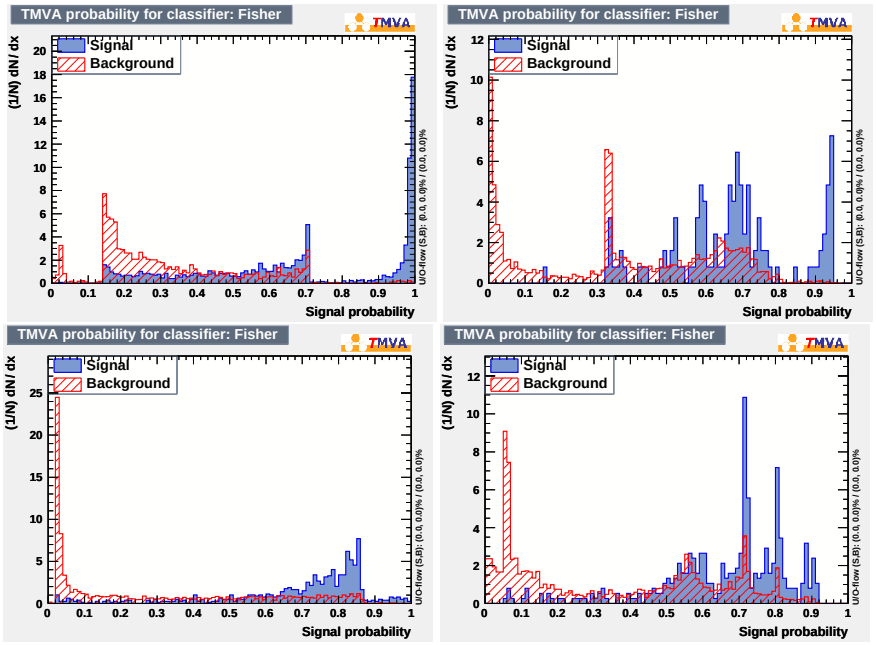

Figure 11.4.7: Probability distributions for selecting Higgs boson decays to each of $b\bar{b}$,$c\bar{c}$,W^+W^- and gg from the Fisher Discriminant.

right handed polarisations

$$a = \frac{(1-P_{e^-})(1+P_{e^+})}{4} \ , \qquad b = \frac{(1+P_{e^-})(1-P_{e^+})}{4}$$

through a measurement of the W production and decay angles Θ and θ in $e^+e^- \to W^+W^- \to q\bar{q}q\bar{q}$, $q\bar{q}l^-\bar{\nu}$ at $\sqrt{s}$ =1 TeV in the forward region $0.8 < \cos\Theta$. This measurement is made independently for two different configurations, $(P_{e^-},P_{e^+}) = (-0.8,0.2)$, $(+0.8,-0.2)$ assuming 500 fb^{-1} integrated luminosity for each configuration. This benchmark study provides a test of jet reconstruction of boosted W bosons in forward regions, jet energy resolution, differential luminosity measurement, and reconstruction and identification of leptons in the forward region.

Once a and b have been measured the actual electron and positron polarisations P_{e^-} and P_{e^+} can be extracted using the relations

$$P_{e^-} = b-a \pm \sqrt{(b-a)^2 - 2(a+b) + 1}$$
$$P_{e^+} = P_{e^-} - 2(b-a) \ .$$

Table 11.4.2: Relative uncertainties on the Higgs $\sigma \times BR$ expected for an integrated luminosity of 1 ab^{-1} at $\sqrt{s}$ =1 TeV using the SiD detector.

h→	#events	$\Delta(\sigma \times BR)$
$b\bar{b}$	xxx	xxx
$c\bar{c}$	xxx	xxx
W^+W^-	xxx	xxx
gg	xxx	xxx

The sign ambiguity is resolved using knowledge of the signs of the beam polarisations.

The production angle Θ is defined to be the polar angle of the W^- in the W^+W^- rest frame. No attempt is made to measure the charges of the hadronically decaying W's in the fully hadronic topology $W^+W^- \to q\bar{q}q\bar{q}$, and so $|\cos\Theta|$ is used in this case. The charge of the decay lepton determines the charge of the W for the semileptonic topology $e^+e^- \to W^+W^- \to q\bar{q}l^-\bar{\nu}$.

For the semileptonic topology the decay angle θ is defined to be the polar angle of the fermion in the W^- rest frame ($W^- \to l^-\bar{\nu}$) or the antifermion in the W^+ rest frame ($W^+ \to l^+\nu$). For the fully hadronic topology $|\cos\theta|$ is used where θ is the polar angle of either of the two jets in the W^- rest frame.

The effective right handed polarisation b is measured rather poorly in the forward region $0.8 < \cos\Theta$ due to the dominance of the polarisation configuration with left-handed electrons and right handed positrons. Therefore the effective polarisation parameters a and b are also measured using the entire solid angle $-1 < \cos\Theta < 1$, with the caveat that the result is only valid for Standard Model W^+W^- production. Only the semileptonic topology is used for measuring the polarisation outside the forward region.

Finally, it can also be assumed that the magnitudes of the beam polarisations don't change as the signs of the polarisations are changed. In this case data from the two polarisation configurations $(P_{e^-}, P_{e^+}) = (-0.8, 0.2)$, $(+0.8, -0.2)$ can be combined in order to measure $|P_{e^+}|$and $|P_{e^-}|$. The measured parameters a and b are replaced by

$$\alpha = \frac{(1+|P_{e^-}|)(1+|P_{e^+}|)}{4}\,, \qquad \beta = \frac{(1-|P_{e^-}|)(1-|P_{e^+}|)}{4}$$

and the absolute polarisation values are given by

$$|P_{e^-}| = \alpha - \beta \pm \sqrt{(\alpha-\beta)^2 - 2(\alpha-\beta) + 1}$$
$$|P_{e^+}| = 2(\alpha-\beta) - P_{e^-}\ .$$

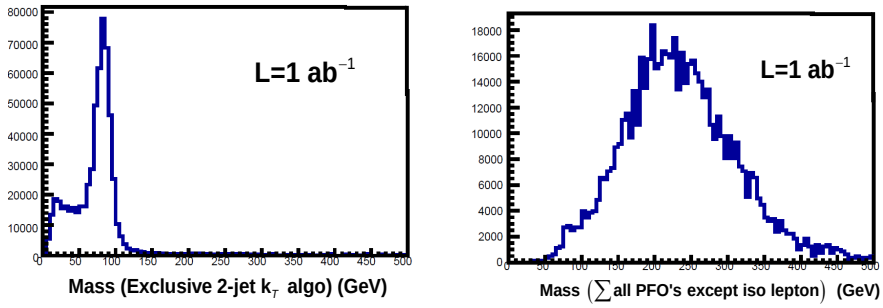

Figure 11.4.8: Mass of the hadronically decaying W in semileptonically W^+W^- events using the 2 jets from the exclusive k_t jet algorithm (left) and using all PFO objects other than the isolated charged lepton (right). The broad and displaced mass distribution on the right results from including PFO objects arising from background processes.

Event reconstruction

The analysis is performed using a list of particle flow objects (PFO's) provided by the event reconstruction program. The large number of e^+e^- pairs produced in the bunch collision creates in each event a pair of large energy PFO's at small angle, one on each side of the collision point. This background is eliminated by removing any PFO with energy greater than 1600 GeV and pseudo-rapidity larger than 1.

Isolated electrons, muons and photons must be identified to separate W pairs from background processes and to classify a W^+W^- event as semileptonic or fully hadronic. The algorithm to identify isolated objects loops through electrons, muons and photons with $p_T > 25$ GeV, removes them one at a time from the PFO list, and performs the inclusive k_t jet algorithm with R=0.7 on the modified PFO list. For each inclusive jet with $E_{jet}/E_{lepton} > 2E_{lepton}$ the variable $\rho = 2E_{lepton}(1-\cos\theta_{jet-lepton})$ is calculated where $\theta_{jet-lepton}$ is the angle between the lepton and the jet. If the minimum value of ρ over all jets is greater than 2 then the object is said to be isolated.

Further event reconstruction depends on whether an event contains one or zero isolated objects. If an event contains zero isolated electron, muons and photons, then the 4-jet exclusive k_t jet algorithm with R=0.7 is applied to the PFO list. The three jet pair combinations are considered, and the one that minimises $(M_{12}-M_W)^2+(M_{34}-M_W)^2$ is chosen to represent the W^+W^- in the fully hadronic mode. The exclusive mode of the k_t jet algorithm is used because it discards beam jets and returns only central jets. In this way the $\gamma\gamma \rightarrow$ hadrons

Table 11.4.3: Number of events passing semileptonic W^+W^- cuts for 500 fb^{-1} luminosity.

Type	Solid Angle	P(e^-)	P(e^+)	Number of events
Signal	$0.8 < \cos\Theta < 1.0$	-80%	+20%	122300
Signal	$-1 < \cos\Theta < 0.8$	-80%	+20%	37040
Signal	$0.8 < \cos\Theta < 1.0$	+80%	-20%	8490
Signal	$-1 < \cos\Theta < 0.8$	+80%	-20%	3216
Background	$0.8 < \cos\Theta < 1.0$	-80%	+20%	3547
Background	$-1 < \cos\Theta < 0.8$	-80%	+20%	5050
Background	$0.8 < \cos\Theta < 1.0$	+80%	-20%	3985
Background	$-1 < \cos\Theta < 0.8$	+80%	-20%	3699

background is minimized [56].

If an event contains one isolated electron or muon and no other isolated object then the lepton is removed from the PFO list and the 2-jet exclusive k_t jet algorithm with R=0.7 is performed using the modified PFO list. The 2-jet system returned by the k_t jet algorithm represents the hadronically decaying W in the semileptonic W^+W^- topology. The neutrino from the leptonically decaying W is reconstructed assuming that the W^+W^- is produced back-to-back: $\vec{p}_\nu = -(\vec{p}_{lepton} + \vec{p}_{2jet})$.

Event selection

Semileptonic W^+W^- events are selected by requiring that there be exactly one isolated electron or muon, that the total number of PFO's in the hadronically decaying W (the two jets returned by the two-jet exclusive k_t jet algorithm) be greater than 12, that the mass of the hadronically decaying W be greater than 60 GeV and less than 100 GeV, that the mass of the leptonically decaying W be less than 250 GeV, and that the energy of the hadronically decaying W be greater than 300 GeV. The cut on mass of the leptonically decaying W is required to remove $\gamma e^- \to \nu W^-$ events. Such events can provide interesting polarisation information, but are considered beyond the scope of this benchmark.

The reconstructed mass of the hadronically decaying W in semileptonic events is shown in Figure 11.4.8 along with the mass obtained by summing together all PFO objects with the exception of the charged lepton. The effectiveness of the 2-jet exclusive k_t jet algorithm in removing $\gamma\gamma \to$ hadrons is clear. The number of signal and background events following these cuts is summarised in Table 11.4.3.

Table 11.4.4: Number of events passing fully hadronic W^+W^- cuts for 500 fb^{-1} luminosity.

Type	Solid Angle	P(e^-)	P(e^+)	Number of events
Signal	$0.8 < \|\cos\Theta\| < 1.0$	-80%	+20%	293250
Signal	$0.8 < \|\cos\Theta\| < 1.0$	+80%	-20%	23720
Background	$0.8 < \|\cos\Theta\| < 1.0$	-80%	+20%	32971
Background	$0.8 < \|\cos\Theta\| < 1.0$	+80%	-20%	7851

Fully hadronic W^+W^- events are selected by requiring that there be no isolated electron, muon or photon, that the total number of PFO's in the two hadronically decaying W's (the four jets returned by the four-jet exclusive k_t jet algorithm) be greater than 28, that the mass of the each of the hadronically decaying W's be greater than 55 GeV and less than 105 GeV, and that the sum of the energies of the two hadronically decaying W be greater than 600 GeV. The number of signal and background events following these cuts is summarised in Table 11.4.4.

Beam Polarisation Measurements

The effective polarisation parameters a and b are extracted by counting events in bins of $(\cos\Theta, \cos\theta)$ and fitting for a and b with a linear least squares fit:

$$\chi^2 = \sum_i \frac{(N_i - (a\mu_i + b\nu_i)L)^2}{N_i}$$

where N_i is the number of events in bin i, L is the integrated luminosity

$$\mu_i = \int d\vec{x}_i d\vec{x'} \eta(\vec{x'}) \Omega(\vec{x}_i, \vec{x'}) \frac{d\sigma_{LR}}{d\vec{x'}}$$
$$\nu_i = \int d\vec{x}_i d\vec{x'} \eta(\vec{x'}) \Omega(\vec{x}_i, \vec{x'}) \frac{d\sigma_{RL}}{d\vec{x'}}$$

$\eta(\vec{x})$ is the detection efficiency, $\Omega(\vec{x}_i, \vec{x'})$ is the resolution function, and $d\sigma_{LR}/d\vec{x}$ and $d\sigma_{RL}/d\vec{x}$ are the true differential cross sections for 100% polarised beams for signal *and* background. The background must be included in this way since it in general has a polarisation dependence.

There is no need to separately calculate $\eta(\vec{x})$ and $\Omega(\vec{x}_i, \vec{x'})$ since the parameters μ_i and ν_i are linearly related to the bin contents of a $(\cos\Theta, \cos\theta)$ histogram of fully simulated Monte

Table 11.4.5: Polarisation errors assuming 500 fb^{-1} luminosity for each initial state polarisation configuration.

$\cos\Theta$ range	P_{e^-}, P_{e^+}	Δa	Δb	ΔP_{e^-}	ΔP_{e^+}
$0.8 < \cos\Theta < 1$	-0.8,+0.2	0.0011	0.62	3.77	2.51
$0.8 < \cos\Theta < 1$	+0.8,-0.2	0.00030	0.20	0.13	0.27
$-1 < \cos\Theta < 1$	-0.8,+0.2	0.0010	0.084	0.51	0.32
$-1 < \cos\Theta < 1$	+0.8,-0.2	0.00027	0.032	0.020	0.08
$\cos\Theta$ range	P_{e^-}, P_{e^+}	$\Delta\alpha$	$\Delta\beta$	$\Delta\lvert P_{e^-}\rvert$	$\Delta\lvert P_{e^+}\rvert$
$-1 < \cos\Theta < 1$	sum	0.00097	0.00027	0.0017	0.0027

Carlo events. Let M_{ki} be the number of events in bin i from a Monte Carlo sample produced with effective beam polarisations a_k and b_k and luminosity L_k. The SiD Monte Carlo samples were produced with $(P_{e^-}, P_{e^+}) = (-0.8, +0.2)$ $(k = 1)$ and $(P_{e^-}, P_{e^+}) = (+0.8, -0.2)$ $(k = 2)$. The parameters μ_i and ν_i are then given by

$$\mu_i = \frac{1}{a_1 b_2 - a_2 b_2}\left[b_2 \frac{M_{1i}}{L_1} - b_1 \frac{M_{2i}}{L_2}\right], \qquad \nu_i = \frac{1}{a_1 b_2 - a_2 b_2}\left[-a_2 \frac{M_{1i}}{L_1} + a_1 \frac{M_{2i}}{L_2}\right].$$

Ten divisions each are used for $\cos\Theta$ and $\cos\theta$ so that 100 bins are defined for each of the two event topologies, semileptonic and fully hadronic. A total of 200 bins are then used for the least squares fit of the effective polarisations a and b or α and β. The errors on the effective polarisations are displayed in Table 11.4.5 along with the errors on the actual polarisations P_{e^-} and P_{e^+}.

11.4.4 Top quark cross-section, mass, and forward-backward asymmetry

Introduction

The top quark is the heaviest elementary particle known. The explanation for its large mass may come from beyond the standard model physics[cite(s)]. Generally, models predict the top quark couples strongly to the particle(s) that generate the spontaneous symmetry breaking of the electroweak interaction as a result of the top quark's large mass. As such, it is important to measure the characteristics of the top quark with high precision.

In this analysis, we investigate the determination of the cross-section and the forward-backward asymmetries for both the b and $\bar{\text{b}}$ quarks and t and $\bar{\text{t}}$ quarks using the fully hadronic $\text{t}\bar{\text{t}}$ decay mode ($e^+e^- \to \text{t}\bar{\text{t}} \to \text{b}\bar{\text{b}}\text{q}\bar{\text{q}}\text{q}\bar{\text{q}}$). The forward-backward asymmetry is defined in Equation 11.4.3.

$$A_{FB} = \frac{\sigma(\theta < 90^o) - \sigma(\theta > 90^o)}{\sigma(\theta < 90^o) + \sigma(\theta > 90^o)} \tag{11.4.3}$$

where $\sigma(\theta < 90^o)$ is the cross-section of the events in which the b or t quark has a polar angle of less than 90^o in the centre-of-mass frame of reference.

Event Selection

The event selection presented in this study is closely based on an early study[cite]. We require that jets be composed of at least two reconstructed particles in order to reject semi-leptonic $t\bar{t}$ decays and other SM backgrounds. The total energy originating from the six jets is required to be greater than 400 GeV in order to suppress events with leptons and neutrinos. We also require that each event has a particle and track multiplicity greater than 80 and 30, respectively. The next step of the event selection is to identify the two b-jets in the signal event, which is achieved by using the LCFI algorithm [89]. The importance of correctly identifying the b-jets is twofold: to reduce the SM background and to reduce the number of combinations required to reconstruct the full signal event. As such, we require that the jet with the highest b-tag value be greater that 0.9 and the jet with the second highest b-tag value be greater than 0.4. Once the b-jets are identified, the remaining jets are assumed to be associated with the W boson hadronic decays. The top quark mass is determined using a kinematic fitting approach with constraints listed in Table 11.4.1. The combination with the smallest χ^2 is selected as the proper event configuration. The results from the kinematic

Table 11.4.1: Top mass kinematic constraints.

$m(\text{top}_1)$	=	$m(\text{top}_2)$
$m(W_1)$	=	80.4 GeV
$m(W_2)$	=	80.4 GeV
$m(b_1)$	=	5.8 GeV
$m(b_2)$	=	5.8 GeV
E_{tot}	=	$\sqrt{s}$
$\vec{p}_{tot}$	=	0

fitting algorithm are presented in Figure 11.4.9. Finally, we require that the reconstructed mass of the top quark candidates be between 145 GeV and 195 GeV, yielding a final signal efficiency of $27.2 \pm 0.1\%$. After applying all the event selections, the cross-section for

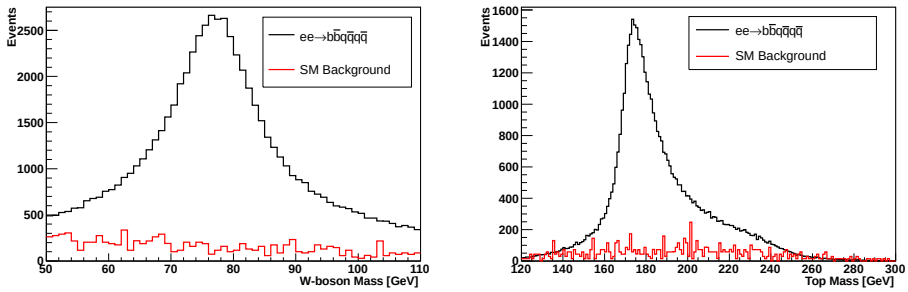

Figure 11.4.9: Mass distribution of the W boson candidates (left) and top quark candidates (right).

$e^+e^- \to t\bar{t} \to b\bar{b}q\bar{q}q\bar{q}$ was calculated using Equation 11.4.4.

$$\sigma = \frac{N_{tot} - N_{bkg}}{\varepsilon_{sig} \int \mathscr{L} dt} \tag{11.4.4}$$

Here N_{tot} is the number of total events that survive all selection cuts, N_{bkg} is the estimated background events after the selection cuts, ε_{sig} is the signal efficiency, and $\int \mathscr{L} dt$ is the integrated luminosity. The cross-section was calculated to be 354.3±1.4 fb and ??±?? fb for the p80m20 and m80p20 polarisation, respectively.

Forward-Backward Asymmetry

In order to determine the forward-backward asymmetry, the charge associated to the bottom and top quarks must be determined. Based on the previous studies[cite], the vertex charge and the jet charge are the two variables that are used in determining the quark charge. The vertex charge is determined by calculating a momentum weighted charge using the tracks associated to the secondary vertex within the identified b-jet, as defined in Equation 11.4.5.

$$Q = \frac{\sum_j p_j^k Q_j}{\sum_j p_j^k} \tag{11.4.5}$$

Here p_j^k and Q_j are the momentum and the charge of the j-th track and $k = 0.3$ is a power weight. Similarly, the jet charge is also calculated using Equation 11.4.5, however, it is determined by using all the tracks associated to a b-jet. These two variables are combined to provide a single discriminate variable, C, as defined in Equation 11.4.6.

$$C = \frac{1-r}{1+r}; \quad r = \prod_i \frac{f_i^{\bar{b}}(x_i)}{f_i^{b}(x_i)} \tag{11.4.6}$$

Here $f_i^b(x_i)$ and $f_i^{\bar{b}}(x_i)$ is the probability density function for variable x_i for the b and $\bar{b}$ quarks, respectively.

The calculation of A_{FB} for the bottom quarks can be performed by using the effective charge from Equation 11.4.6 and the angle θ of the identified b-jets. The corrected number of b-jets in each hemisphere is calculated using Equation 11.4.7.

$$N_b = (N_{tot} - N_{bkg}) * \varepsilon_p * \varepsilon_{sig} \tag{11.4.7}$$

Here, N_{tot} is the total number of events, N_{bkg} is the background events, ε_p is the purity, and ε_{sig} is the signal efficiency. Finally, we require that the product of the two effective charges be negative, resulting in the bottom quark forward-backward asymmetry yield ??±?? which agrees well with the MC input value. Similarly, the calculation of A_{FB} for the top quarks is performed by using the effective charge of the b-jet and the angle θ of the reconstructed top quark. We require that the product of the two charges is negative, resulting in the top quark forward-backward asymmetry yield ??±?? which agrees well with the MC input value.

Conclusion

The achievable resolution for the forward backward asymmetry of the top quark at the ILC in the $e^+e^- \to t\bar{t} \to b\bar{b}q\bar{q}q\bar{q}$ channel is approximately 0.0?? for a total luminosity of 500 fb^{-1} Similarly the achievable resolution for the b quark resulting from the top decay is also 0.0??. In the case of polarized beams the achievable resolution for both the top and bottom quark asymmetries is 0.0?? and 0.0?? for the -80% electron polarization, +20% positron polarization and the +80% electron polarization, -20% positron polarization respectively.

11.5 Additional Benchmarks

11.5.1 The Analysis and the Importance of the BeamCal

One of the processes whose detection is very difficult at the LHC but easier at the ILC is the $\widetilde{\tau}$ production [102]. In this benchmark, the $\tilde{\tau}^{\pm}$ production and decay has been studied [103] at the kinematically accessible benchmark points B', C', D', G', and I' as proposed in [104]. At these points, the LSP is the $\tilde{\chi}_1^0$, and the NLSP is the $\tilde{\tau}^{\pm}$, with the masses shown in Table 11.5.1. Having similar masses, the two particles are a candidate for the co-annihilation mechanism that can explain the WMAP relic dark-matter density. It is therefore important

to identify and measure the mass of the NLSP, as well as the LSP. Several studies of the $\tilde{\tau}^{\pm}$ at the ILC have already been made. These include an analysis at D' [105], an analysis at SPS1a' [106], and a much broader analysis covering many parameter points [107].

Table 11.5.1: SUSY Particle Masses (GeV).

Model	B'	C'	D'	G'	I'
$\tilde{\tau}^{-}$	110.6	170.6	223.9	158.6	144.6
$\tilde{\chi}_1^0$	96.5	161.0	216.4	150.9	140.8

At the benchmark points analysed here, the $\tilde{\tau}^{\pm}$ has only one decay channel: $\tilde{\tau}^{\pm} \rightarrow \tau^{\pm}\tilde{\chi}_1^0$. The production of τ leptons via the two-photon process $e^+e^- \rightarrow e^+\gamma^* e^-\gamma^* \rightarrow e^+e^-\tau^+\tau^-$ is by far the most significant background process, and the BeamCal is an essential detector to veto two-photon events by detecting high energy scattered e^+e^- beam particles. Figure 11.5.1 shows the detection efficiency as a function of radius in the BeamCal for 5, 15, 30, 50, 100, and 150 GeV electrons. As the beamstrahlung energy has a strong radial and azimuthal dependence, the detection efficiency is calculated as a function of the distance from the outgoing beam axis at three azimuthal angles (0, 90, and 180 degrees). The inefficiency between 30 and 50 mm at $\phi = 180^\circ$ is due to the incoming beam hole. Since the beamstrahlung background energy is the highest at $\phi \approx 90^\circ$ (and 270°), the detection efficiency is lower at this angular region. The efficiency to detect electrons with energy above 150 GeV is almost 100% up to 8 mrad from the beam axis.

Events are grouped based on their vectorially combined transverse momentum, and it is expected that the SUSY events will often have higher vectorially combined momentum due to the momentum carried away by the $\tilde{\chi}_1^0$. Detection of the $\tilde{\tau}^{\pm}$ by these methods relies on a significant mass difference between the $\tilde{\tau}^{\pm}$ and the $\tilde{\chi}_1^0$. If the mass difference between the $\tilde{\tau}^{\pm}$ and $\tilde{\chi}_1^0$ is not large enough, the visible τs will not have sufficient scalar momentum to be visible above the two-photon process (even if the visible products have a preferred direction). For this reason a cut is made on the acoplanarity of the two jets in the plane perpendicular to the beampipe. The requirements that the mass of each jet be less than 1.8 GeV and the number of charged particles in each jet be either one or three, serve to select $\tau^{\pm}$ events and eliminate other processes such as $hZ^0 \rightarrow$ hadrons. Figure 11.5.2 shows the transverse momentum of combined SM and $\tilde{\tau}^{\pm}$ events (blue) and the SM backgrounds (red) at the benchmark point C' using a data sample based on an integrated luminosity of 250 fb^{-1}. Figure 11.5.2 (left) shows the distribution when the BeamCal is used to veto SM backgrounds, while Figure 11.5.2 (right) shows the distribution without the veto. A significant excess of $\tilde{\tau}^{\pm}$ signal is observable over SM backgrounds only when the BeamCal

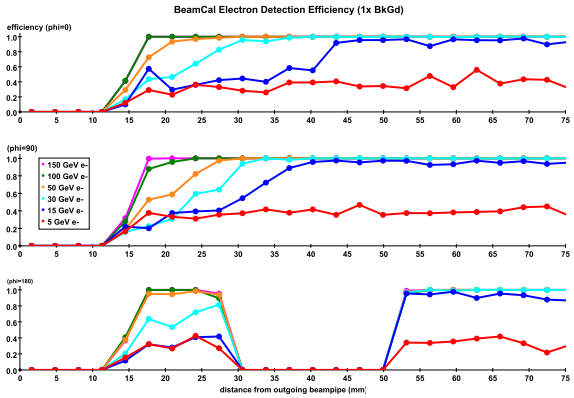

Figure 11.5.1: The BeamCal detection efficiency of electrons, at various energies and angles, as a function of distance from the outgoing beam.

is used as a veto. The mass difference between $\tilde{\tau}^{\pm}$ and $\tilde{\chi}_1^0$ is 9.6 GeV at the benchmark point C', and it is possible to measure the $\tilde{\tau}^{\pm}$ mass with a 1 GeV uncertainty.

Figure 11.5.3 shows the transverse momentum of combined SM and $\tilde{\tau}^{\pm}$ events (blue) and the SM backgrounds (red) at the benchmark point I' using a data sample based on an integrated luminosity of 250 fb^{-1}. Figure 11.5.3 (left) shows the distribution when the BeamCal is used to veto SM backgrounds, while Figure 11.5.3 (right) shows when the BeamCal is not used. Although the $\tilde{\tau}^{\pm}$ signal can be enhanced when the BeamCal is used for a veto, the mass difference between the $\tilde{\tau}^{\pm}$ and the $\tilde{\chi}_1^0$ is only 3.8 GeV at this benchmark point I' and the signal is not very visible even after applying the BeamCal veto. Similarly, good signal-to-noise was achieved by the application of the BeamCal veto for the benchmark points B', C', and G', where the mass difference between $\tilde{\tau}^{\pm}$ and $\tilde{\chi}_1^0$ is about 10 GeV, while the $\tilde{\tau}^{\pm}$ signal was not strong enough for mass measurements for the benchmark points D' and I', where the mass difference is about 5 GeV.

11.6 Benchmarking Summary

A large set of benchmarks have been conducted with the SiD detector using both simulations of the LOI and the more detailed DBD detector variants. They illustrate the physics reach of the SiD concept ranging from centre-of-mass energies of 250 GeV to 1 TeV. All results obtained have been summarised in Table 11.6.1.

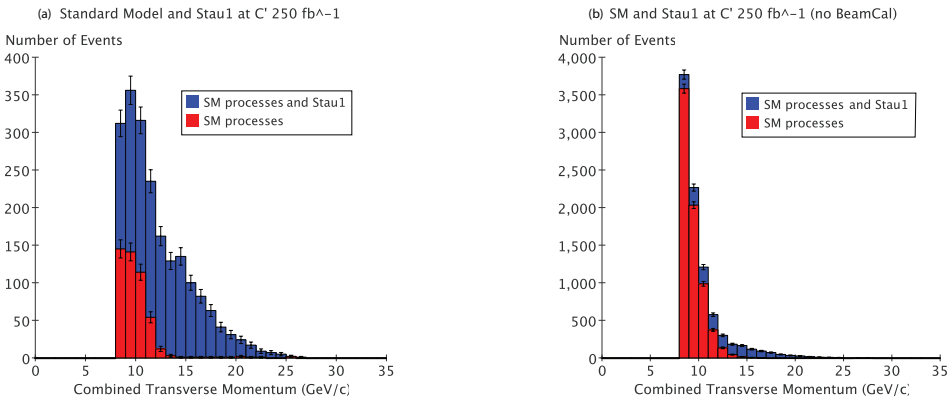

Figure 11.5.2: Fill event p_{T} distribution with (left) and without (right) the BeamCal veto at the benchmark point C'.

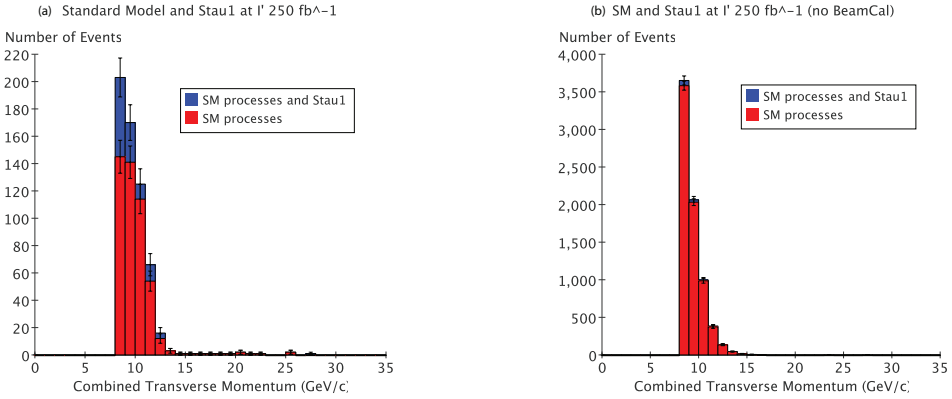

Figure 11.5.3: p_{T} distribution with BeamCal veto (left) and without (right) at the benchmark point l')

Table 11.6.1: Summary of the benchmarking results using both the LOI and the DBD versions of SiD.

Process $e^+e^- \to$	$\sqrt{s}$ (GeV)	$\mathscr{L}$ (fb^{-1})	SiD	Meas. Quant.	Unit	Result
$e^+e^-h/\mu^+\mu^-h$	250	250	LOI	m_H	GeV	$\pm 0.04/0.03$
				σ	fb	$\pm 0.027/0.043$
$hZ^0 \to c\bar{c}q\bar{q}$	250	250	LOI	BR	%	3.3 ± 0.2
$hZ^0 \to c\bar{c}\nu\bar{\nu}$	250	250	LOI	BR	%	3.3 ± 0.4
$hZ^0 \to \mu^+\mu^-q\bar{q}$	250	250	LOI	σ	%	89.1%
$\tau^+\tau^-$	500	250	LOI	A^τ_{FB}	-	0.504 ± 0.02
				A^τ_{FB}	-	0.470 ± 0.02
$t\bar{t} \to 6$ jets	500	500	LOI	m_{top}	GeV	173.92 ± 0.05
				σ	%	0.49%
				A^t_{FB}	-	0.342 ± 0.015
$\tilde{\chi}^0_2\tilde{\chi}^0_2 \to \tilde{\chi}^0_1\tilde{\chi}^0_1Z^0Z^0$	500	500	LOI	$m_{\tilde{\chi}^0_1}$	GeV	± 0.16
$\tilde{\chi}^0_2\tilde{\chi}^0_2 \to \tilde{\chi}^0_1\tilde{\chi}^0_1Z^0Z^0$	500	500	LOI	$m_{\tilde{\chi}^+_1}$	GeV	± 0.45
$\tilde{\chi}^+_1\tilde{\chi}^-_1 \to \tilde{\chi}^0_1\tilde{\chi}^0_1W^+W^-$	500	500	LOI	$m_{\tilde{\chi}^0_1}$	GeV	± 0.28
$\tilde{\chi}^+_1\tilde{\chi}^-_1 \to \tilde{\chi}^0_1\tilde{\chi}^0_1W^+W^-$	500	500	LOI	$m_{\tilde{\chi}^0_2}$	GeV	± 0.49
$t\bar{t}h$ (6 jets)	1000	1000	DBD	σ	%	± 13.6
$t\bar{t}h$ (8 jets)	1000	1000	DBD	σ	%	± 12.3
$t\bar{t}h$ (combined)	1000	1000	DBD	σ	%	± 9.1
$\nu_e\bar{\nu}_e h; h \to WW^*$	1000	1000	DBD	BR	%	
$\nu_e\bar{\nu}_e h; h \to gg$	1000	1000	DBD	BR	%	
$\nu_e\bar{\nu}_e h; h \to c\bar{c}$	1000	1000	DBD	BR	%	
$\nu_e\bar{\nu}_e h; h \to b\bar{b}$	1000	1000	DBD	BR	%	
$\nu_e\bar{\nu}_e h; h \to \mu^+\mu^-$	1000	1000	DBD	BR	%	
W^+W^-	1000	1000	DBD	σ	%	
$t\bar{t} \to 6$ jets	500	500	DBD	m_{top}	GeV	

Chapter 12

Costs

12.1 Introduction

The SiD cost estimate is a construction cost estimate; it does not include R&D, commissioning, operating costs, or physicist salaries.

The SiD design process has continuously monitored costs using a parametric cost model. This tool has been essential for the ongoing detector optimisation process. At various stages, detector parameters (e.g. dimensions or masses) have been transferred to a Work Breakdown Structure where it is more convenient to describe a subsystem to arbitrary levels of detail. Here we describe the DBD version of SiD as such a point design.

Table 12.1.1: Unit Costs agreed to by SiD, ILD, and CLIC [108].

	agreed unit cost (US-$)	agreed error margin (US-$)
Tungsten for HCAL	105/kg	45/kg
Tungsten for ECAL	180/kg	75/ kg
Steel for Yoke	1000/t	300/t
Stainless Steel for HCAL	4500/t	1000/t
Silicon Detector	6 / cm^2	2 / cm^2

The SiD baseline for the DBD has been changed from RPC's to scintillator bars for the muon system (see Chapter 5), which is also included in the costing model.

At the time of the LOI, the cost optimisation of the global SiD design was studied by using a parametric model of PFA based jet energy resolution and the parametric cost tools

described here. The tracker radius, B field, and HCAL depth were varied holding the jet energy resolution fixed at 3.78% for 180 GeV jets. The cost optimal point was quite near the baseline SiD parameters of R = 1.25 m, B = 5 T, and HCAL λ_I = 4.5. This work has not been repeated.

12.2 Parametric cost model

The parametric model of the detector is a large set of Excel spreadsheets that first maintain a self consistent model of SiD. It is straightforward to vary parameters ranging from the most basic, such as the tracker radius and aspect ratio, to parameters such as the number of tracking layers, the number and thickness of HCAL layers, and calorimeter radiator material. The tracking layers and disks are adjusted to fit the allocated space.The calorimeter inner radii and minimal z coordinate are adjusted for the tracker size, and thicknesses are set parametrically. The solenoid model is adjusted for its radius and field, and the flux return is adjusted to roughly contain the return flux.

For each system, the cost driving component count, such as tungsten plate, silicon detectors, and readout chips for the ECAL, are calculated. The model has tables for material costs and estimates both M&S and labour costs that are associated with the actual scale of SiD. Costs that are approximately fixed, for example, engineering, fixturing, or solenoid He plants, are imported from the separate Work Breakdown Structure program. Finally, a set of macros calculate the costs of SiD as parameters are varied.

The cost process also develops a Work Breakdown Structure using the SLAC program WBS. WBS facilitates the description of the costs as a hierarchical breakdown with increasing levels of detail. Separate tables describe cost estimates for purchased M&S and labour. These tables include contingencies for each item, and these contingencies are propagated by WBS. The M&S costs are estimated in 2008 US-$ except for those items described in Table 12.1.1. Labour is estimated in man-hours or man-years as convenient. The WBS had about 50 labour types, but they are condensed to engineering, technical, and clerical for this estimate. The statement of base M&S and labour in man-years by the three categories results in a cost which we believe is comparable to that used by the ILC machine, and is referred to here as the ILC cost.

Contingency is estimated for each quantity. While contingency is not explicit ILC value system, it gives an estimate of the uncertainties in the costs of the detector components. Items which are commodities, such as detector iron, have had costs swinging wildly over the last few years. While there is agreement on a set of important unit costs, those quantities also have ”error margins”.

SiD, ILD, and CLIC have worked together to reach agreed values for some unit costs as

shown in Table 12.1.1.

There are a substantial set of interfaces in the interaction region hall. For the purpose of this estimate, the following has been assumed:

- The hall itself, with finished surfaces, lighting, and HVAC are provided by the machine.
- Utilities, including 480 VAC power, LCW, compressed air, and Internet connections are provided.
- An external He compressor system with piping to the hall is provided. The refrigeration and associated piping is an SiD cost.
- All surface buildings, gantry cranes, and hall cranes are provided by the machine.
- Data storage systems and offline computing are provided by others.
- SiD will be assembled and will travel on a suitable platform for push-pull. This platform and its motion and alignment systems will be provided by the machine.
- QD0's and their 2K systems are provided by the machine. The beampipe is an SiD cost.

12.3 Results

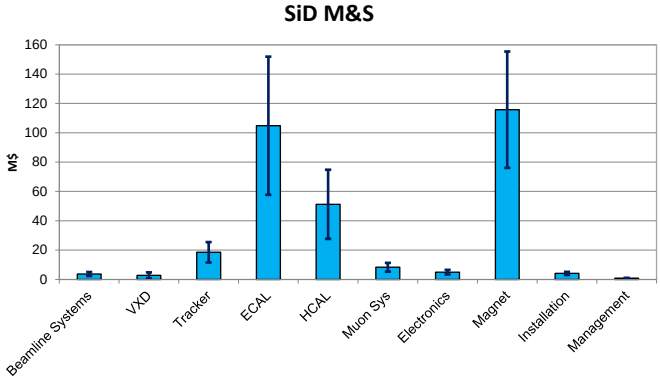

Figure 12.3.1: Subsystem M&S Costs in million US-$, the error bars show the contingency per subsystem.

Table 12.3.1: Summary of Costs per Subsystem.

	M&S Base (M US-$)	M&S Contingency (M US-$)	Engineering (MY)	Technical (MY)	Admin (MY)
Beamline Systems	3.7	1.4	4.0	10.0	
VXD	2.8	2.0	8.0	13.2	
Tracker	18.5	7.0	24.0	53.2	
ECAL	104.8	47.1	13.0	288.0	
HCAL	51.2	23.6	13.0	28.1	
Muon System	8.3	3.0	5.0	22.1	
Electronics	4.9	1.6	44.1	41.7	
Magnet	115.7	39.7	28.3	11.8	
Installation	4.1	1.1	4.5	46.0	
Management	0.9	0.2	42.0	18.0	30.0
	314.9	126.7	186.0	532.1	30.0

The subsystem level summary is shown in Table 12.3.1, the M&S costs are plotted in Figure 12.3.1, and the labour costs are shown in Figure 12.3.2. The costs are dominated by the Magnet and the ECAL. The magnet has roughly equal costs for the superconducting coil and the iron. The ECAL is dominated by the silicon detectors. The cost estimate has several important "commodity" items whose costs have recently been fluctuating significantly. For SiD, these include most metals and processed silicon detectors. Table 12.3.2 illustrated the cost sensitivity to these prices by indicating the unit cost used in the estimate and the effect on the SiD M&S cost of doubling the unit cost.

The superconducting coil cost is difficult to estimate, because there is little data and experience with coils of this size and field. An attempt was made to extract the CMS coil cost, and it is believed to be US-$ 48M for cold mass and vacuum tank. A Japanese industrial estimate for the SiD coil was obtained, and it was approximately the same as CMS, but for a coil with roughly half the stored energy. Cost functions linear in the stored energy and with a 0.66 exponential dependence have been studied. SiD has taken a conservative approach and for the parametric study has used a linear model fit to the Babar coil at the low end and the industrial estimate at the high end. The result for the current SiD design is US-$ 55M, higher than the CMS cost, but inflation and currency exchange variations have been ignored. SiD is doing R&D on advanced conductor design, and there is some reason to expect the coil cost estimate to decrease.

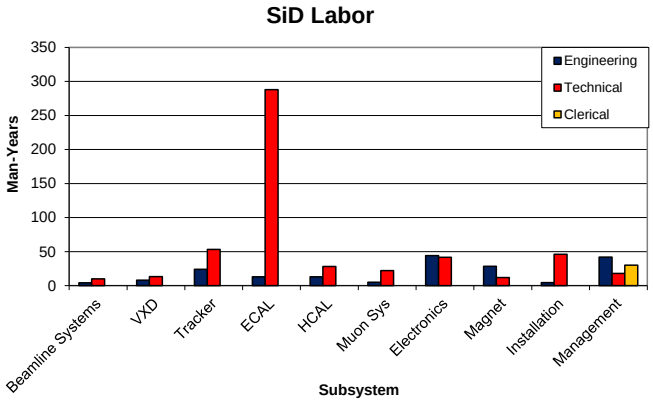

Figure 12.3.2: Subsystem Labour

Table 12.3.2: Sensitivity to selected unit costs. The table shows the effect on the total M&S cost if the selected unit cost were to double.

Material	Base Cost (US-$)	Delta Cost (M US-$)	Fractional Delta (%)
Magnet Iron	6.00 /kg	48	16
Silicon Sensors	6.00 /cm^2	79	26
Tungsten ECAL	180 /kg	14	5
Stainless	4.5 /kg	2	1
HCAL Detector	12K /m^2	42	14

The SiD cost in ILC value units is US-$ 315M for M&S, 186 MY engineering, 532 MY technical, and 30 MY administrative labour. The estimated M&S contingency, reflecting uncertainty in unit costs and some estimate of the maturity of this study, is US-$ 127M. The cost in US accounting, assuming a construction start in 2016 and 3.5% per year inflation and US National Laboratory labour rates, is US-$ 857M. The components of the US accounting calculation are indicated below in Table 12.3.3.

12.4 Parameter Dependencies

The parametric fitter enables studies of the SiD cost against the major parameters of the detector. Figure 12.4.1 shows the dependence on the HCAL thickness, Figure 12.4.2 on the

Table 12.3.3: Components of the US accounting style estimate.

	M&S (M US-$)	Labour (M US-$)	Totals (M US-$)
Base	315	81	396
Contingency	127	18	144
Total	442	99	540
Indirect rates	0.06	0.20	
Indirects	26	20	46
Totals w/ indirects	468	119	587
Total in FYXXXX M$	2008		586.7
Start Year	2016		
Construction Duration	6 years		
Inflation	3.5%/a		
Factor	1.460		
Total Escalation			269.9
Total			856.6

central value of the magnetic field, and Figure 12.4.3 on the tracker radius. In all case the cost is M&S base cost; contingency and labour are not included.

SiD has also examined using higher density absorber material in terms of their cost impact, especially by reducing the diameter of the coil. In this exercise, the number of layers and λ_I has been keep constant. It has been found, that moving from an all-steel HCAL to an all-tungsten HCAL would increase the total cost of SiD by about US-$ 26M. In adapting a configuration used in CLIC_SiD [56] where the transition of barrel and endcap has been optimised for cost and by using tungsten only for the barrel, the cost increase goes down to US-$ 15M. So in terms of cost optimisation, moving to a tungsten HCAL is not beneficial for SiD.

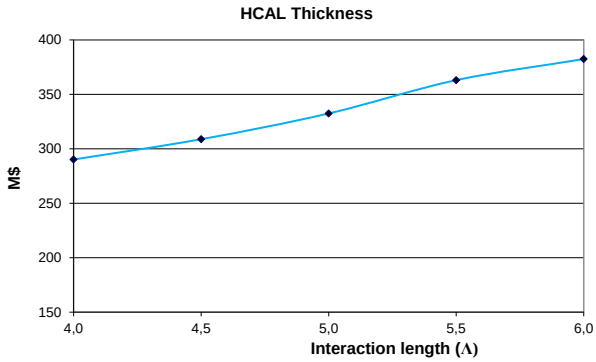

Figure 12.4.1: Dependence of the SiD M&S base cost on the thickness of the HCAL

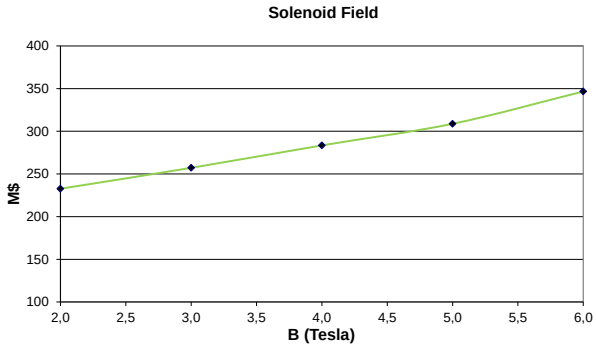

Figure 12.4.2: Dependence of the SiD M&S base cost on the Solenoid Field

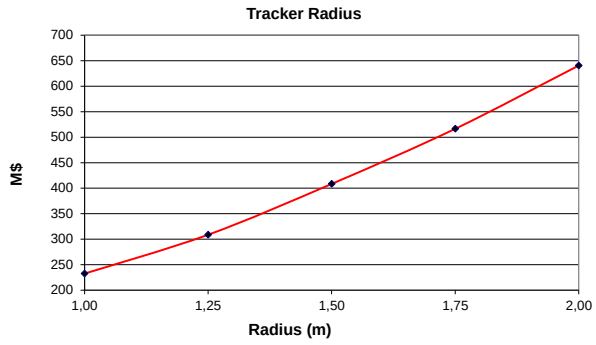

Figure 12.4.3: Dependence of the SiD M&S base cost on the Tracker barrel radius

Chapter 13

Summary

13.1 The Status of the SiD Detector Concept

We have presented a Detailed Baseline Design for the SiD Detector Concept for experiments at a future Linear Collider. Our design is mature and delivers the required detector and physics performance as demonstrated so far by our simulations. The baseline choices for the SiD subsystems represent our current selections in terms of level of successful R&D, measured and or simulated performance characteristics, dimensional practicality, and cost. We will continue to develop alternative technology options where they show promise for enhanced performance. The detector design presented here has been aimed specifically at a 500 GeV or 1 TeV ILC. A modified SiD design, aimed at CLIC energies up to 3 TeV, has already been described in the CLIC CDR [56].

13.2 Further Development of the SiD Detector Concept

As a detector concept we strongly believe that, while technologies and/or their implementations may evolve over time, SiD will remain an excellent tool for exploration of physics at a linear collider. There are several aspects to this from the detector, physics, organisational, and resource perspectives. We therefore propose to further study and develop SiD as new information emerges in the Higgs and possibly other new physics areas. There are areas of detector R&D that must be further developed and completed, followed by studies of specific implementations in a full technical design. In parallel, while a limited number of physics processes have been studied for this DBD, there are other processes that should be addressed in continued studies. The sum of all these detector and physics activities points towards a lively and sustained effort on SiD as a well identified concept moving forward

into the next phase of linear collider development. We therefore see SiD as a vital element of the future program and a major component of the Physics and Detectors section of the new Linear Collider Organisation.

SiD has evolved from the LOI stage as a largely U.S.- based activity to a more global concept with increased contributions from outside the Americas. Our aim is to expand to an even more global level of participation, and we will pursue this vigorously within the new organisation.

13.3 SiD and the New Global Linear Collider Organisation

The members of the SiD Detector Concept look forward to working with the new global Linear Collider Organisation. We view the new organisation as a framework within which we can advance our concept towards a full technical detector design for ILC, and, working with our CLIC colleagues, for CLIC also. We support the creation of a group having broad representation from the concept groups, R&D collaborations, with well-balanced regional representation, to advance the case for the linear collider and to support a specific implementation when timely. We believe that, when the time is right for the linear collider to move towards realisation, having a well identified detector concept with a substantial U.S. participation within the global organisation, will significantly benefit discussion of the U.S. contribution to the project as a whole.

Bibliography

[1] (Ed.) Aihara, H., (Ed.) Burrows, P., (Ed.) Oreglia, M., et al. SiD Letter of Intent. 2009, 0911.0006. arXiv:0911.0006, SLAC-R-944.

[2] MDI Common Task Group. MDI CTG Agreement Granada 2011 to use Platform for Push-Pull.

[3] MDI Common Task Group and ILC CFS Group. MDI CTG and CFS Agreement Granada 2011 for Layout of Vertical Access IR Hall.

[4] Grzegorz Deptuch, Marcel Demarteau, James Hoff, Farah Khalid, Ronald Lipton, et al. Vertically integrated pixel readout chip for high energy physics. 2011.

[5] Y. Onuki, H. Katsurayama, Y. Ono, H. Yamamoto, Y. Arai, et al. SOI detector developments. PoS, VERTEX2011:043, 2011.

[6] Marc Winter, Jerome Baudot, Auguste Besson, Gilles Claus, Andrei Dorokhov, et al. Development of CMOS Pixel Sensors fully adapted to the ILD Vertex Detector Requirements. 2012, 1203.3750.

[7] L. Gaioni, M. Manghisoni, L. Ratti, V. Re, and G. Traversi. A 3D deep n-well CMOS MAPS for the ILC vertex detector. Nucl.Instrum.Meth., A617:324–326, 2010.

[8] M. Benoit. Vertex Detectors for future Linear Colliders, 2012. CERN LCD-OPEN-2012-013.

[9] D. Dannheim. Vertex-Detector R&D for CLIC, 2012. CERN LCD-OPEN-2012-014.

[10] Stefan Rummel and Ladislav Andricek. The DEPFET active pixel sensor for vertexing at ILC and Super KEKB. Nucl.Instrum.Meth., A623:189–191, 2010.

[11] A. Nomerotski et al. PLUME collaboration: Ultra-light ladders for linear collider vertex detector. Nucl.Instrum.Meth., A650:208–212, 2011.

[12] Ronald Lipton. 3D detector and electronics integration technologies: Applications to ILC, SLHC, and beyond. Nucl.Instrum.Meth., A636:S160–S163, 2011.

[13] C. Petteway A. Hollingsworth P. Enquist, G. Fountain and H. Grady. Low Cost of Ownership scalable copper Direct Bond Interconnect 3D IC technology for three dimensional integrated circuit applications. 3D System Integration, 2009.

[14] C.J. Kenney, J.D. Segal, E. Westbrook, S. Parker, J. Hasi, et al. Active-edge planar radiation sensors. Nucl.Instrum.Meth., A565:272–277, 2006.

[15] Ronald Lipton et al. Combining the Two 3Ds. submitted to Jinst., 2012.

[16] C. Baltay, W. Emmet, D. Rabinowitz, J. Brau, N. Sinev, et al. Chronopixel Vertex Detectors for Future Linear Colliders. 2011, 1109.2811.

[17] A. Affolder, B. Allongue, G. Blanchot, F. Faccio, C. Fuentes, et al. DC-DC converters with reduced mass for trackers at the HL-LHC. JINST, 6:C11035, 2011.

[18] C. Fuentes, B. Allongue, G. Blanchot, F. Faccio, S. Michelis, et al. Optimization of DC-DC converters for improved electromagnetic compatibility with high energy physics front-end electronics. IEEE Trans.Nucl.Sci., 58:2024–2031, 2011.

[19] William E. Cooper. Vertex Detector Cable Considerations. FERMILAB-CONF-09-047-E, 2009, 0902.3023.

[20] Grzegorz Deptuch et al. A vertically integrated pixel readout device for the Vertex Detector at the International Linear Collider. IEEE Trans.Nucl.Sci., 57:880–890, 2010.

[21] P. Valerio et al. Evaluation of 65 nm technology for CLIC pixel front-end, 2011. CERN LCD-Note-2011-022.

[22] Pierpaolo Valerio. Design of the 65 nm CLICpix demonstrator chip, 2012. CERN LCD-Note-2012-018.

[23] T Tick and M Campbell. Tsv processing of medipix3 wafers by cea-leti: a progress report. Journal of Instrumentation, 6(11):C11018, 2011.

[24] D. Freytag, R. Herbst, J. Brau, M. Breidenbach, R. Frey, et al. KPiX, An Array of Self Triggered Charge Sensitive Cells Generating Digital Time and Amplitude Information. 2008.

[25] D. Freytag, R. Herbst, J. Brau, M. Breidenbach, R. Frey, et al. KPiX: a 1024 Channel Readout ASIC for the ILC. IEEE Nuclear Science Symposium and Medical Imaging Conference. Accepted for presentation.

[26] C. Neher, R.L. Lander, A. Moskaleva, J. Pasner, M. Tripathi, et al. Further Developments in Gold-stud Bump Bonding. JINST, 7:C02005, 2012, 1112.1037.

[27] ATLAS inner detector: Technical design report. Vol. 1. 1997.

[28] C. Chasman et al. A Heavy Flavor Tracker for STAR, 2006.

[29] S. Dhiwan. Powering Delivery to KPiX Chips, 2010. http://shaktipower.sites.yale.edu/sites/default/files/Powering_KPiX_Chips_SiD_Workshop_111410_0.pdf.

[30] S. Dhiwan. Testing of Cables for KPiX Pulse Load, 2011. http://shaktipower.sites.yale.edu/sites/default/files/Testing_Cables_KPiX_Pulse_Load_ALCPG11.pdf.

[31] Christian Grefe. OverlayDriver: An event mixing tool for org.lcsim, 2011.

[32] Christian Grefe. Detector Optimization Studies and Light Higgs Decay into Muons at CLIC. PhD thesis, 2012. to appear.

[33] Eckhard von Thoerne Dmitry Onoprienko. Calorimeter Assisted Tracking Algorithm for SiD.

[34] Christian Grefe. Tracking Performance in sidloi3, 2012.

[35] Stewart T. Boogert and David J. Miller. Questions about the measurement of the e+ e- luminosity spectrum at a future linear collider. pages 509–516, 2002, hep-ex/0211021.

[36] G.W. Wilson. http://ilcagenda.linearcollider.org/conferenceDisplay.py?confId=1556, 2007. ALCPG, Chicago.

[37] Frey, R. et al. Design considerations for a silicon-tungsten electromagnetic calorimeter for a linear collider detector. In Proc. 10th International Conference on Calorimetry in High Energy Physics, page 304. World Scientific, 2002.

[38] D. Strom. Review of the Calorimeter R&D program, DESY, 2007. http://ilcagenda.linearcollider.org/sessionDisplay.py ?sessionId=38&slotId=22&confId=1296#20070531.

[39] J.A. Ballin, J.P. Crooks, P.D. Dauncey, B. Levin, M. Lynch, et al. A MAPS-based readout for a tera-pixel electromagnetic calorimeter at the ILC. Nucl.Phys.Proc.Suppl., 197:342–345, 2009.

[40] J.A. Ballin, P.D. Dauncey, A.-M. Magnan, M. Noy, Y. Mikami, et al. A Digital ECAL based on MAPS. 2009, 0901.4457.

[41] Paul Dauncey. Performance of CMOS sensors for a digital electromagnetic calorimeter. PoS, ICHEP2010:502, 2010.

[42] M. Stanitzki. Advanced monolithic active pixel sensors for tracking, vertexing and calorimetry with full CMOS capability. Nucl.Instrum.Meth., A650:178–183, 2011.

[43] Gary Drake, Jose Repond, David G. Underwood, and Lei Xia. Resistive Plate Chambers for hadron calorimetry: Tests with analog readout. Nucl.Instrum.Meth., A578:88–97, 2007.

[44] Burak Bilki, John Butler, Ed May, Georgios Mavromanolakis, Edwin Norbeck, et al. Environmental Dependence of the Performance of Resistive Plate Chambers. JINST, 5:P02007, 2010, 0911.1351.

[45] Burak Bilki, John Butler, Ed May, Geordios Mavromanolakis, Edwin Norbeck, et al. Measurement of the Rate Capability of Resistive Plate Chambers. JINST, 4:P06003, 2009, 0901.4371.

[46] Burak Bilki, John Butler, Tim Cundiff, Gary Drake, William Haberichter, et al. Calibration of a digital hadron calorimeter with muons. JINST, 3:P05001, 2008, 0802.3398.

[47] Burak Bilki, John Butler, Ed May, Georgios Mavromanolakis, Edwin Norbeck, et al. Measurement of Positron Showers with a Digital Hadron Calorimeter. JINST, 4:P04006, 2009, 0902.1699.

[48] Burak Bilki, John Butler, Georgios Mavromanolakis, Ed May, Edwin Norbeck, et al. Hadron Showers in a Digital Hadron Calorimeter. JINST, 4:P10008, 2009, 0908.4236.

[49] R. Chechik, A. Breskin, C. Shalem, and D. Mormann. Thick GEM-like hole multipliers: Properties and possible applications. Nucl.Instrum.Meth., A535:303–308, 2004, physics/0404119.

[50] Y. Giomataris, P. Rebourgeard, J.P. Robert, and Georges Charpak. MICROMEGAS: A High granularity position sensitive gaseous detector for high particle flux environments. Nucl.Instrum.Meth., A376:29–35, 1996.

[51] P. Buzhan, B. Dolgoshein, L. Filatov, A. Ilyin, V. Kantserov, et al. Silicon photomultiplier and its possible applications. Nucl.Instrum.Meth., A504:48–52, 2003.

[52] Solid-state Division 1126-1 Ichino-cho Hamamatsu City 435-8558 Japan. Hamamatsu Photonics K. K. Technical Note.

[53] C. Adloff et al. Construction and Commissioning of the CALICE Analog Hadron Calorimeter Prototype. JINST, 5:P05004, 2010, 1003.2662.

[54] CALICE Analysis Notes, https://twiki.cern.ch/twiki/bin/view/CALICE/CaliceAnalysisNotes.

[55] C. Adloff et al. Tests of a particle flow algorithm with CALICE test beam data. JINST, 6:P07005, 2011, 1105.3417.

[56] Lucie Linssen, Akiya Miyamoto, Marcel Stanitzki, and Harry Weerts. Physics and Detectors at CLIC: CLIC Conceptual Design Report. 2012, 1202.5940.

[57] A.I. Drozhdin, N.V. Mokhov, N. Nakao, S.I. Striganov, and L. Keller. Suppression of muon backgrounds generated in the ILC beam delivery system. Conf.Proc., C070625:2945, 2007.

[58] Minos Collaboration, D. G. Michael, P. Adamson, T. Alexopoulos, W. W. M. Allison, G. J. Alner, K. Anderson, C. Andreopoulos, M. Andrews, R. Andrews, and et al. The magnetized steel and scintillator calorimeters of the MINOS experiment. Nuclear Instruments and Methods in Physics Research A, 596:190–228, November 2008, 0805.3170.

[59] Adloff and et al. Construction and performance of a silicon photomultiplier/extruded scintillator tail-catcher and muon-tracker. Journal of Instrumentation, 7:4015, April 2012, 1201.1653.

[60] R.M. Carey et al. Proposal to search for μ-N $\rightarrow$ e-N with a single event sensitivity below 10^{-16}. 2008.

[61] M. Bona et al. SuperB: A High-Luminosity Asymmetric e+ e- Super Flavor Factory. Conceptual Design Report. 2007, 0709.0451.

[62] Paul Rubinov. Studies of pulse shape in SiPMs. TiPP 2011. .

[63] R. Santonico and R. Cardarelli. DEVELOPMENT OF RESISTIVE PLATE COUNTERS. Nucl.Instrum.Meth., 187:377–380, 1981.

[64] A.V. Barashkov, G.L. Glonti, A.L. Gongadze, M.I. Gostkin, A.V. Guskov, et al. Common support and integration of the BMS/BMF type MDT/RPC chambers of the muon spectrometer of the ATLAS experiment. 2005.

[65] Serguei Chatrchyan et al. Performance Study of the CMS Barrel Resistive Plate Chambers with Cosmic Rays. JINST, 5:T03017, 2010, 0911.4045.

[66] H.R. Band, J. Hollar, P. Tan, F. Anulli, R. Baldini, et al. Performance and aging studies of BaBar resistive plate chambers. Nucl.Phys.Proc.Suppl., 158:139–142, 2006.

[67] (ed.) Brau, James, (ed.) Okada, Yasuhiro, (ed.) Walker, Nicholas J., (ed.) Djouadi, Abdelhak, (ed.) Lykken, Joseph, et al. International Linear Collider reference design report. 1: Executive summary. 2: Physics at the ILC. 3: Accelerator. 4: Detectors. 2007.

[68] B. Parker, A. Mikhailichenko, K. Buesser, J. Hauptman, T. Tauchi, et al. Functional Requirements on the Design of the Detectors and the Interaction Region of an e+ e- Linear Collider with a Push-Pull Arrangement of Detectors. 2009.

[69] ARUP. ARUP final report: task 2.

[70] CMS. CMS TDR.

[71] CERN Vibration Team. CERN EDMS 1099646.

[72] K. Bertsche. CERN EDMS 1027459.

[73] T. Keller L., Markiewicz and T. Maruyama. Beam-Gas Interactions in the ILC Beam Delivery System. ILC-Note-2007-016.

[74] R. et al Apsimon. The FONT5 prototype ILC intra-train beam feedback system at ATF2. Proceedings of the Particle Accelerator Conference, New York, 2011.

[75] S. Smith. SiD Intratrain Feedback BPM and Kicker Design. 2011.

[76] G.R. White, D. Schulte, and N.J. Walker. Design and simulation of the ILC intra-train orbit and luminosity feedback systems. Conf.Proc., C060626:3041–3043, 2006.

[77] G. White. Beam-Beam Feedback, ALCPG11, Eugene, OR, 2011.

[78] D. Tshilumba C. Collette, S. Janssens. Control strategies for the final focus of future linear particle collider. Nucl.Instrum.Meth., A684:7–17, 2012.

[79] P.A. Coe, D.F. Howell, and R.B. Nickerson. Frequency scanning interferometry in ATLAS: Remote, multiple, simultaneous and precise distance measurements in a hostile environment. Measur.Sci.Tech., 15:2175–2187, 2004.

[80] Yanmei Han, Armin Reichold, Colin Perry, and Richard Bingham. Frequency Scanning Fibre Interferometer for Absolute Distance Measurements Over a Large Target

Area. eConf, C06092511:WEPO09, 2006.

[81] Hai-Jun Yang and Keith Riles. High-precision absolute distance measurement using dual-laser frequency scanned interferometry under realistic conditions. Nucl.Instrum.Meth., A575:395–401, 2007, physics/0609187.

[82] K. Riles. Update on FSI R&D for SiD Final Focus Magnet Alignment. LCWS 2011,Granada, Spain. 2011-09-28.

[83] G.P. Summers, E.A. Burke, P. Shapiro, S.R. Messenger, and R.J. Walters. Damage correlations in semiconductors exposed to gamma, electron and proton radiations. Nuclear Science, IEEE Transactions on, 40(6):1372 –1379, dec 1993.

[84] N. Walker et al. ILC Machine Parameter Tables. 2012. ILC-EDMS-925325.

[85] Simulator for the Linear Collider (SLIC), http://www.lcsim.org/software/slic/.

[86] S. Agostinelli et al. Geant4 – a simulation toolkit. Nucl. Instrum. Methods Phys. Res. A, 506(3):250–303, July 2003.

[87] Linear Collider simulations, http://lcsim.org/software/lcsim/1.18/.

[88] M. A. Thomson. Particle Flow Calorimetry and the PandoraPFA Algorithm. Nucl. Instrum. Methods, A611:25–40, 2009. arXiv:0907.3577.

[89] LCFIPlus, https://confluence.slac.stanford.edu/display/ilc/LCFIPlus.

[90]

[91] The sidloi3 detector description, http://www.lcsim.org/detectors/sidloi3.html.

[92] M. Cacciari and G. P. Salam. Dispelling the N^3 myth for the k_t jet-finder. Phys. Lett., B641:57–61, 2006. hep-ph/0512210.

[93] Matteo Cacciari, Gavin P. Salam, and Gregory Soyez. FastJet User Manual. Eur.Phys.J., C72:1896, 2012, 1111.6097.

[94] Matteo Cacciari and Gavin P. Salam. Dispelling the N^3 myth for the k_t jet-finder. Phys.Lett., B641:57–61, 2006, hep-ph/0512210.

[95] Andreas Hoecker, Peter Speckmayer, Joerg Stelzer, Jan Therhaag, Eckhard von Toerne, and Helge Voss. TMVA: Toolkit for Multivariate Data Analysis. PoS, ACAT:040, 2007, physics/0703039.

[96] M. Battaglia, T. Barklow, Michael E. Peskin, Y. Okada, S. Yamashita, et al. Physics benchmarks for the ILC detectors. eConf, C050318:1602, 2005, hep-ex/0603010.

[97] M. Davier, L. Duflot, F. Le Diberder, and A. Rouge. The Optimal method for the measurement of tau polarization. Phys.Lett., B306:411–417, 1993.

[98] Laurent Duflot. New method of measuring tau polarization. Application to the tau $\rightarrow$ a1 tau-neutrino channel in the ALEPH experiment. 1993.

[99] E. Boos, M. Dubinin, M. Sachwitz, and H.J. Schreiber. Probe of the W t b coupling in t anti-t pair production at linear colliders. Eur.Phys.J., C16:269–278, 2000, hep-

ph/0001048.

[100] Stefano Profumo. Neutralino dark matter, b tau Yukawa unification and nonuniversal sfermion masses. Phys.Rev., D68:015006, 2003, hep-ph/0304071.

[101] ILC PEB Benchmarks Task Force, Barklow T, Berggren M, Fujii K, Graf N, Miyamoto A, Peskin M, Richard F, and Weiglein G. Detector benchmarking for the 2012 dbd. May 2011.

[102] Michael Peskin. Will these be supersymmetry at the ILC? Presented at the workshop: Implications of LHC Results for TeV-scale Physics, July 2012.

[103] A. Jenkins et al. Signal Analysis of the Stau at the ILC.

[104] M. Battaglia, A. De Roeck, John R. Ellis, F. Gianotti, K.A. Olive, et al. Updated post - WMAP benchmarks for supersymmetry. Eur.Phys.J., C33:273–296, 2004, hep-ph/0306219.

[105] C. Long. Undergraduate Honors Thesis, Department of Physics, High Energy Physics Group, University of Colorado at Boulder, August 2010. Master's thesis.

[106] Philip Bechtle, Mikael Berggren, Jenny List, Peter Schade, and Olga Stempel. Prospects for the study of the $\tilde{\tau}$-system in SPS1a' at the ILC. Phys.Rev., D82:055016, 2010, 0908.0876.

[107] Carola F. Berger, James S. Gainer, JoAnne L. Hewett, and Thomas G. Rizzo. Supersymmetry Without Prejudice. JHEP, 0902:023, 2009, 0812.0980.

[108] M. Breidenbach et al. CLIC Detector Costing, 2012. CERN LCD-Note-2012-005.